UNIVERSITY OF CALIFORNIA,
IRVINE

Electromagnetic Wavefront Manipulation with Metasurfaces

DISSERTATION

submitted in partial satisfaction of the requirements
for the degree of

DOCTOR OF PHILOSOPHY

in Electrical and Computer Engineering

by

Mehdi Veysi

Dissertation Committee:
Associate Professor Filippo Capolino, Chair
Associate Professor Ozdal Boyraz
Professor Lee Swindlehurst

2017

“If at first the idea is not absurd, then there is no hope for it”

Albert Einstein

TABLE OF CONTENTS

LIST OF FIGURES

ACKNOWLEDGMENTS

First and foremost, I would like to express the deepest appreciation to my advisor Prof. Filippo Capolino, who has the attitude and the substance of a genius. I appreciate his high standards in research and in the quality of the work we produced. Without his guidance and persistent help this dissertation would not have been possible. I would also like to thank the doctoral committee members, Prof. Ozdal Boyraz and Prof. Lee Swindlehurst who provided guidance and support in our collaborations continuously. I am indebted to their very valuable comments on this thesis. I would also like to thank Prof. Alexander Figotin, Prof. Yahya Rahmat-Samii, and Prof. Regina Ragan who provided valuable guidance and constant support in our collaborations.

Every result provided in this thesis was accomplished with the valuable help and support of my fellow labmates and collaborators. Dr. Caner Guclu and I worked together on several different phases of this thesis and without his efforts and his knack for solving seemingly intractable problems, my job would have certainly been more difficult. I also acknowledge the contribution of my current labmate, Mohammed Othman who I benefited from his keen scientific insight. The former and current members of our research group and the graduate students in EECS department were always like an ever growing close-knit community, I thank them all, in particular Dr. Salvatore Campione, Farshad Yazdi, Saman Kabiri, Dr. Ali Hosseini, Dr. Shiji Pan, Kaveh Shahverdi, Dmitry Oshmarin, Mohammad Kamandi, Jinwei Zeng, Mohammad Albooyeh, Mahsa Darvishzadeh-Varcheie, Hamidreza Kazemi, Ahmad Tariq Almutawa, and Mohamed Yehia Nada. I am also very grateful to the friendship of Saman Jafarluo, Arghavan Arafati, and Peyman Nazari who made my time here at UCI a lot more fun. I am thankful to all of them for being my family in Irvine. The former and current staff at the Electrical Engineering department always kept an eye on the graduate students' wellbeing and helped us in most urgent conditions. Therefore, I am very grateful to them, especially to Amy Pham, Susan Staebell, Loretta Waltemeyer, and Elvia Salas.

Most importantly, I am deeply grateful to my mother, my dad, my sisters whose their constant love and endless support give me the strength to pursue my goals in life.

I am also grateful for the funding sources that allowed me to pursue my graduate school studies: the National Science Foundation, the USA Keck Foundation, and the Multidisciplinary University Research Initiative administered through the University of New Mexico.

The text of this dissertation is a reprint of the materials as they appear in Journal of the Optical Society of America B and IEEE Antennas and Propagation Magazine. The co-author listed in these publications directed and supervised research which forms the basis for the dissertation.

CURRICULUM VITAE

Mehdi Veysi

2017 Ph.D in Electrical and Computer Engineering, University of California, Irvine

2010 M.S. in Electrical and Electronics Engineering, K. N. Toosi University of Technology, Tehran, Iran

2007 B.S in Biomedical Engineering, University of Isfahan, Isfahan, Iran

EXPERIENCE

2017 RF/Antenna Engineer, Ossia Inc., Bellevue, WA, USA

2013-2017 Graduate Student Researcher, Electrical Engineering and Computer Science, University of California Irvine, Advisor: Prof. Filippo Capolino

2010-2012 Antenna Director, K. N. Toosi University Research Center, Tehran, Iran

FIELD OF STUDY

Metamaterials, phased-array antennas, Orbital Angular Momentum Beams, nano engineered materials, metasurfaces, Shaped-beam Reflector and Reflectarrays, electromagnetic modeling, numerical methods

PUBLICATIONS

J1. **M. Veysi**, C. Guclu, F. Capolino, and Y. Rahmat-Samii, "Revisiting the Orbital Angular Momentum Beams: Fundamentals, Reflectarray Generation, and Novel Antenna Applications" *In review process with IEEE Antenna and Propagation Magazine.*

J2. **M. Veysi**, M. Othman, A. Figotin, and F. Capolino, "Theory of The Degenerate Band Edge Laser" *In review process* (*arXiv preprint arXiv:1708.01381*)

J3. **M. Veysi**, C. Guclu, O. Boyraz, and F. Capolino, "Reflective metasurface lens with an elongated needle-shaped focus," *Journ. Opt. Soc. Am. B*, Vol. 34, No. 2, pp. 374-382, (2017)

J4. **M. Veysi**, C. Guclu, and F. Capolino, "Focused Azimuthally Polarized Vector Beam and Spatial Magnetic Resolution below the Diffraction Limit", *JOSA B*, vol. 32, pp. 345-354, 2016

J5. **M. Veysi**, C. Guclu, O. Boyraz, and F. Capolino, "Thin Anisotropic Metasurfaces for Simultaneous Light Focusing and Polarization Manipulation" *J. Opt. Soc. Am. B*, Vol. 32,

No. 2, (2015)

J6. **M. Veysi,** C. Guclu, and F. Capolino, "Vortex Beams With Strong Longitudinally Polarized Magnetic Field and Their Generation by Using Metasurfaces" *J. Opt. Soc. Am. B*, Vol. 32, No. 2, (2015)

J7. C. Guclu, **M. Veysi**, and F. Capolino, "Photoinduced Magnetic Nanoprobe Excited by Azimuthally Polarized Vector Beam", *ACS Photonics* 3 (11), pp 2049–2058 (2016).

J8. A. A. K. Othman, **M. Veysi**, A. Figotin, and F. Capolino, "Giant amplification in degenerate band edge slow-wave structures interacting with an electron beam," *Physics of Plasmas,* Vol. 23, No. 3, 033112, (2016)

J9. M. A. K. Othman, **M. Veysi,** A. Figotin, and F. Capolino, "Low Starting Electron Beam Current in Degenerate Band Edge Oscillators," IEEE Trans. on Plasma Science, Vol. 44, No. 6, pp. 918-020, (2016). *Article is highlighted by the Editor in the June's issue.*

J10. N. Sharac, H. Sharma, **M. Veysi**, M. Khine, F. Capolino, and R. Ragan "Tunable Optical Response of Bowtie Nanoantenna Arrays on Thermoplastic Substrates" *Nanotechnology* Vol. 27, Issue 10, pp. 1-12, (2016)

J11. F. Yazdi, M. A. K. Othman, **M. Veysi,** A. Figotin, and F. Capolino, "A New Amplification Regime for Traveling Wave Tubes with Third Order Modal Degeneracy," *In review process*

J12. J. Zeng, F. Huang, C. Guclu, **M. Veysi,** H. K. Wickramasinghe, and F. Capolino, "Sharply focused azimuthally polarized beams with magnetic dominance: near-field characterization at nanoscale by photoinduced force microscopy," *In review process*

J13. M. Kamandi, M. Albooyeh, C. Guclu, **M. Veysi**, J. Zeng, K. Wickramasinghe, and F. Capolino, "Enantio-specific Detection of Chiral Nano-Samples Using Photo-induced Force," *In review process*

ABSTRACT OF THE DISSERTATION

Electromagnetic Wavefront Manipulation with Metasurfaces

By

Mehdi Veysi

Doctor of Philosophy in Electrical and Computer Engineering

University of California, Irvine, 2017

Associate Professor Filippo Capolino, Chair

Conventional optical devices such as lenses with aberration correction, quarter-wave plate made of birefringent and chiral materials, spatial light modulators, and spiral phase-plates may meet the performance demand in both bandwidth and efficiency, but they are usually bulky, and difficult to integrate in nanophotonic systems. Nevertheless, the market constantly demands cheaper and thinner devices with better performance. In the last few years with the availability of nanoscale fabrication tools, plasmonic metasurfaces with subwavelength unit cells have attracted increasing attention in optics and photonics due to their capability to manipulate beams' wavefront over a subwavelength distance. Metasurfaces can introduce vast flexibility in the design of optical devices by tailoring the polarization state and wavefront of the beams. The manipulation of the light beams can be realized with resonant elements, which provide phase change discontinuities as the light travels across the metasurface (i.e., structured surface). The possibility of creating abrupt phase changes at optical/infrared frequencies can eliminate the need for propagation path compensation in lensing, or reduce the physical dimensions required for a quarter-wave plate or a phase-plate, because the tailoring of the beam is achieved by resonant printed

elements on a metasurface with an extremely subwavelength thickness. Probably even more importantly such abrupt phase changes recently enabled the generation of complex optical beams with orbital angular momentum a reality. Such beam characteristics are desired in many applications such as free space communications, remote sensing, multi-mode communication systems and secure communications.

This dissertation focuses on flat thin metasurfaces for wavefront engineering. We demonstrate the exotic capability of the metasurface in local phase, amplitude and polarization control of the electromagnetic waves along the surface populated with resonant antennas. A new class of flat, compact, multifunctional components, so-called polarizing lens, is introduced in an attempt to merge two important optical components, a circular polarizer and a lens, into a thin plasmonic metasurface. The concept of polarizing lens is then further extended to the investigation and development of multi-focus lenses and lenses with extended depth of focus. Another exotic application of metasurfaces is transforming incident beams into complex beams such as vector beams with non-uniform local polarization distributions. In particular, we focus on realizing azimuthally polarized beams which contain a magnetic dominant region within which longitudinal magnetic field is strong and electric field is ideally null. Such beams are promising for studying weak magnetic transitions in optical frequency range. Lastly, the exotic properties of the orbital angular momentum carrying beams, such as annular-shaped intensity profile and helical wavefront, motivated us to generate such beams in radio frequencies. We demonstrate that reflectarrays are an efficient vehicle to generate such beams and show their potential novel applications in wireless communication systems.

CHAPTER 1

INTRODUCTION

Sec. 1.1 The Concept of Metasurface

This dissertation is based on metasurface concepts developed over the course of electromagnetics engineering in a quest to manipulate the electromagnetic wavefront over a subwavelength distance. Metasurface, also called metafilm, is an artificial flat surface populated with subwavelength antennas whose physical parameters or/and orientations are locally varying to manipulate the incident beam wavefront over a subwavelength distance [1]–[9]. The metasurface concept is analogous to the reflectarray concept proposed to replace bulky reflector antennas with flat light-weight reflectarray antennas in microwave/millimeterwave frequencies [10]–[12]. The metasurface's exotic features such as light-weight, low-profile, flat two-dimensional surface, and their compatibility with integrated CMOS technologies make them a great candidate to replace the conventional bulky three-dimensional electromagnetic components, such as lenses and polarizers, which are taking advantage of the physical dimension of the components to manipulate the beams.

The antennas, which are the building blocks of the metasurfaces, are arranged in a semi-periodic order in a scale smaller than the operating wavelength. Over the past few years,

metasurfaces have found many applications in communication systems from microwave and millimeter wave to optical ranges, such as beam steering, spatial light modulator (SLMs), optical communication networks, generation of structured beams, OAM communication systems, to name only a few. The theory and applications of metasurfaces have been thoroughly discussed and presented in the literature [3], [5], [6], [13]–[19].

This thesis elaborates on the fundamental design of the electromagnetic metasurfaces (in particular multifunctional metasurfaces) as the extension of metamaterials, and their functionality in manipulation of the electromagnetic wave properties. The schematic of a representative metasurface developed in chapter 2 is shown in Fig. 1.1. A broad guideline of designing metasurfaces is also provided throughout the thesis. Based on the proposed subwavelength metasurfaces, multiple potential applications in both microwave and THz/optical frequencies are demonstrated. The fundamental goal of this dissertation lies in that the interaction of electromagnetic beams with metasurface (isotropic or anisotropic) can enable engineering of its local polarization and phase distribution. To this aim, both anisotropic and isotropic nanoantennas (scatters) are utilized.

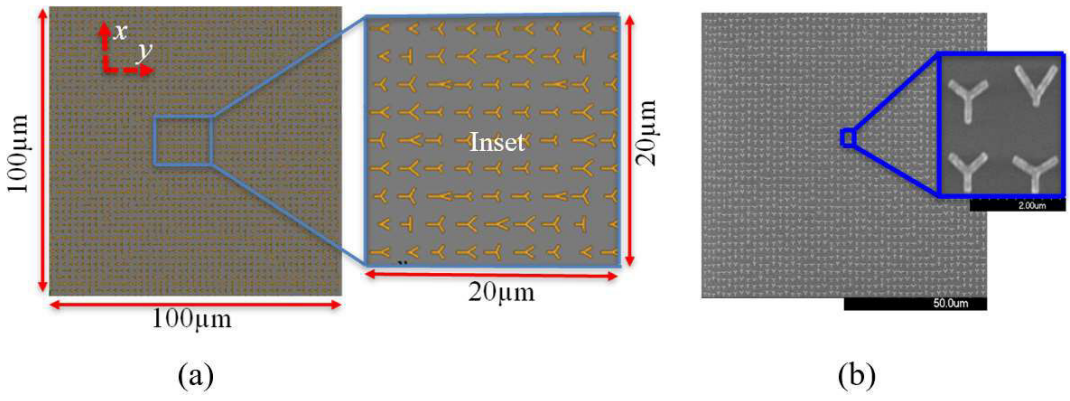

Fig. 1.1. (a) Schematic of a representative metasurface lens, proposed in Chapter 2, made of an array of anisotropic Y-shaped nanoantennas at 4.3µm.

(b) The Scanning electron microscope (SEM) image of the representative polarizing metasurface lens.

In the following, the Generalized Snell's laws [2] which are the basis of the metasurface concept are briefly introduced and then the content of each chapter is explained, leaving the detailed introduction and literature survey of each chapter to the motivation sections of respective chapter.

Sec. 1.2 The Generalized Snell's Laws

The main frame of the dissertation is based on the concept of the generalized Snell's laws that are utilized for wavefront manipulation of the electromagnetic beams. Here we briefly explain such concept and leave the detailed discussions and explanation to Chapter 2. It is known that the angle of refraction at the interface of two different media only depends on the angle of incidence and refractive indices of the two media and is imposed by the Snell's laws, as shown in Fig. 1.2(a). However, by introducing an artificial abrupt phase change along the interface of the two media, it is possible to redirect the refracted wave toward an arbitrary direction. Such a phase shift can be artificially realized and controlled by populating the interface of the two media by electromagnetic scatters (e.g., nanoantennas), as shown in Fig. 1.2(b). The conventional Fermat principle at the presence of such phase discontinuities on the interface between the two media would be then modified as $k_1 \sin\theta_i - k_2 \sin\theta_t = d\phi/dx$, where $d\phi/dx$ is the gradient of the phase discontinuity along the interface, k_1 and k_2 are the wavenumbers in the first and the second media, θ_i and θ_t are the angles of incidence and refraction, respectively [2]. As a result, by populating the interface of the two media by electromagnetic scatters (e.g., antennas) whose dimensions and/or

orientations are varying along the interface of the two media, we would be able to manipulate the wavefront of the incident electromagnetic wave. Such gradient surfaces, also called metasurfaces, have been extensively used, especially in the last decade, to replace the bulky 3D optical components, such as lens and polarizers, [1], [3], [5], [6], [17] similar to the flat reflectarrays which have been used to replace 3D bulky reflector antennas [10]–[12]. However, here the challenge is the metal loss at THz/optical ranges and how to design, optimize, fabricate and measure such THz/optical components.

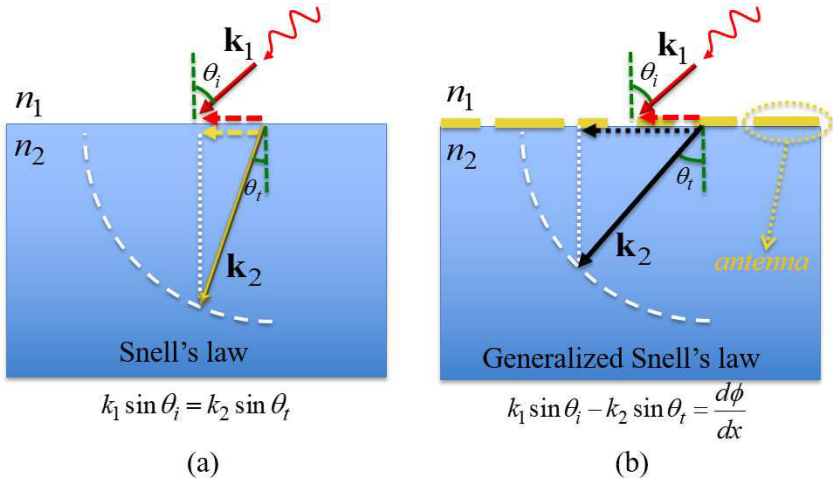

Fig. 1.2. The schematic representation of (a) conventional Snell's law, and (b) generalized Snell's law, of refraction at the interface of two media. In (b), the interface of the two media is artificially decorated with scatterers (here antennas) in order to introduce an abrupt phase shift in the wave path, which is a function of the position along the interface. Here $d\phi/dx$ is the local gradient of the phase discontinuity along the interface imposed by the antennas, k_1 and k_2 are the wavenumbers in the first and second media, θ_i and θ_t are the angle

of incidence in the first medium and the angle of refraction in the second medium, respectively.

Sec. 1.3 Reflectarrays: Historical Background and Their Analogy to Metasurfaces

In early 1960s, the Berry, Malech, and Kennedy conceived for the first time the reflectarray concept by using short-ended waveguide elements [20], as schematically shown in Fig. 1.3. The incident wave from the feed horn couples into the waveguide elements and reflects from the short end of the waveguides. The lengths of the waveguides are locally changed such that the reflected wave from the reflectarray surface forms a co-phasal reradiated far-field beam [12], [20]. However, such a reflectarray antenna was very bulky and heavy. With the development of light-weight, low-loss, printable microstrip antennas, the possibility of combining the microstrip antenna with the reflectarray concept has been extensively investigated in the late 1980s and early 1990s [11], [21]–[23]. Since then, the reflectarray antennas have progressed rapidly and gained increasing popularity in electromagnetics community, due to their compelling features such as, flat surface, light weight, low loss and low cost [12]. The required local phase shift at each reflectarray element can be achieved by varying the physical parameters of the element. Different reflectarray elements have been proposed in the literature, such as rectangular, circular, and ring patches, resonant dipoles and cross-dipoles, to name a few [12].

In the past few years, due to the developments in nanofabrication technologies, mapping the success of the reflectarrays to optical and acoustic domain has been pursued. In this regard, optical [2] and acoustical metasurfaces [24], [25] have been proposed and

experimentally realized. In this thesis, we propose some unique metasurfaces with novel applications at both optical and microwave frequencies, as summarized in Sec. 1.5.

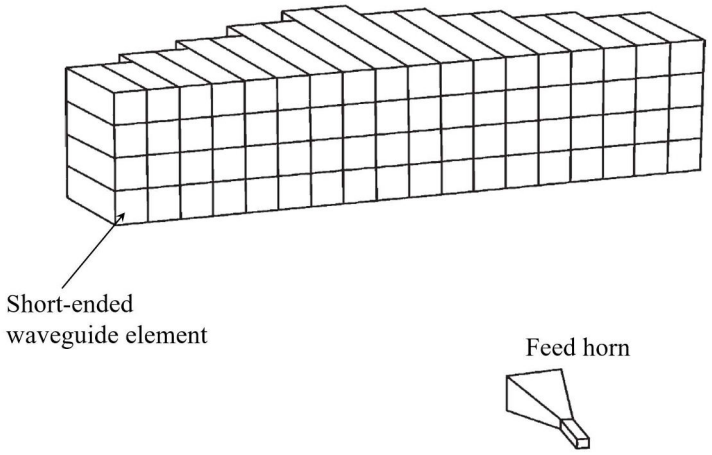

Fig. 1.3. Schematic of an early reflectarray antenna made of an array of short-ended waveguide elements of variable length [20].

Sec. 1.4 Other Techniques and Apparatus for Wavefront Manipulations

Various electromagnetic components have been employed to manipulate the wavefront of the electromagnetic waves by locally changing their phase, amplitude, and polarization. Such components also serve as the basis for optical holography technology, which is the use of amplitude and phase information of an optical field to reconstruct and display a 3D image. One conventional approach to manipulate the wavefront of an electromagnetic wave is to engineer the shape of the interface between the media of given refractive indices and therefore control the optical path of an electromagnetic beam based on the conventional reflection, refraction, and diffraction laws and the phase it accumulates through the refractive media. Such a principle is the basis for many 3D optical components such as lenses, prisms, gratings, and waveplates [26]. Another approach to control the optical path of a light

beam is to employ engineered subwavelength media, so-called metamaterials, to realize the spatially dependent refractive indices [27]–[30]. Metamaterials have been used in many applications such as developing Superlenses [31], [32] and cloakings [33] to name a few. Another technique for wavefront modulation is based on typical optoelectronic devices such as liquid-crystal based spatial-light-modulators (LC-SLMs) [34]. The liquid crystal modulator here has a planar configuration and its molecules' directions are titled with respect to the incident beam direction depending on the applied voltage. The change in the molecules' orientations (from aligned with respect to the incident beam direction when no voltage is applied) directly translates to the change of refractive index and therefore modifies the optical path of the incident beam in the desired way.

In this thesis, we focus on developing novel metasurfaces because of their unique and compelling features [35] as follows: (i) the wavefront manipulation in metasurfaces is performed over a flat 2D surface with a sub-wavelength thickness [2], [35], (ii) metasurface not only gives rise to the manipulation of the electric field but also the magnetic field component of the incident beam [36]–[39], and (iii) metasurfaces are potentially useful to realize multifunctional components and in particular they allow for simultaneous control of phase, magnitude, and polarization of the incident beams [5].

Sec. 1.5 Content of Each Chapter

The dissertation is organized into Chapters that involve metasurface designs and their novel applications from microwave to terahertz and optical ranges.

Chapter 2: The possibility of integration of two important categories of optical components, i.e., circular polarizer and lens, into a thin plasmonic metasurface is studied in

detail. We demonstrate that a single thin plasmonic metasurface is capable of simultaneous tailoring of two important features related to the electromagnetic beams: (i) polarization, and (ii) focusing properties. Since the circular polarizer and lens are at the heart of many optical systems, the possibility of having both light focusing and polarization manipulation capabilities with a thin single layer plasmonic MS would significantly reduce the cost, volume, optical loss, and system complexity.

Chapter 3: A novel metasurface lens with a single elongated depth of focus is presented in this chapter. Novel multifocal flat metasurface lenses are developed using two techniques: (i) polarization diversity, and (ii) annular segmentation of the lens aperture. The polarization-diversity technique enables overall lens aperture reuse, thus doubling the number of foci through the simultaneous focusing of two orthogonal linearly polarized incident beams at two distinct foci using the lens aperture. The annular-segmentation technique, on the other hand, is independent of incident beam polarization and is only based on dividing the lens aperture into concentric annular segments that converge different portions of the illuminating beam at different foci. The total number of foci can be further increased by combining the polarization-diversity and the annular-segmentation techniques. Subsequently, the concept of multifocality is further extended to design a novel flat lens with an overall single needle-like focal region with elongated depth of focus without loss of lateral resolution. To this goal, we design a multifocal lens with overlapping profiles of foci superposed into a single elongated needle-shaped focal region. Using the combination of polarization-diversity and annular-segmentation techniques, we develop a novel MS flat lens made of Y-shaped nanoantennas, whose polarization-dependent reflection phase and amplitude can be controlled independently via their geometrical parameters. Via numerical

calculations, we demonstrate that the proposed MS lens has an overall single focal region with an extremely long DOF of about 74.1 λ, a lateral full width at half maximum varying in the range of 1.37 λ to 2.8 λ, and a numerical aperture of about 0.26 (considering the center of the focal region as the effective focal point). In this chapter, the MS lens's capability to synthesize extremely long DOF is conceptually demonstrated without resorting to time-consuming and complicated wavefront synthesis methods.

Chapter 4: An azimuthally polarized vector beam (APB), with a polarization vortex, has a salient feature that it contains a magnetic-dominant region within which the electric field is ideally null while the longitudinal magnetic field is maximum. In this chapter, we thoroughly investigated such beams and their focusing properties. Fresnel diffraction theory and plane-wave spectral calculations are applied to quantify field features of such a beam upon focusing through a lens. The diffraction-limited full width at half-maximum (FWHM) of the beam's longitudinal magnetic field intensity profile and complementary FWHM of the beam's annular-shaped total electric field intensity profile are examined at the lens's focal plane as a function of the lens's paraxial focal distance. Then, we place a subwavelength dense dielectric Mie scatterer in the minimum-waist plane of a self-standing converging APB and demonstrate for the first time, to the best of our knowledge, that a very-high-resolution magnetic near-field at optical frequency is achieved with total magnetic near-field FWHM of 0.23λ (i.e., magnetic near-field spot area of $0.04\lambda^2$) within a magnetic-dominant region located one radius (0.12λ) away from the scatterer. In particular, the utilization of the nanosphere as a magnetic nanoantenna (so-called magnetic nanoprobe) illuminated by a tightly focused APB is instrumental in boosting the photoinduced magnetic response and suppressing the electric response of a sample matter. The access to the weak photoinduced

magnetic response in sample matter would add extra degrees of freedom to future optical photoinduced force microscopy and spectroscopy systems based on the excitation of photoinduced magnetic dipolar transitions [6], [40]–[45].

Chapter 5: A novel method of generation and synthesis of azimuthally polarized vortex beams, introduced in chapter 4, is presented based on the metasurface concept in this chapter. We show how such beams can be constructed through the interference of Laguerre–Gaussian beams carrying orbital angular momentum (OAM), and then quantify the longitudinal magnetic field of such beams. As an example, we present a metasurface made of double-split ring slot pairs and report a good agreement between simulated and analytical results. Both a high magnetic-to-electric-field contrast ratio and a magnetic field enhancement are achieved. We also investigate the metasurface physical constraints to convert a linearly polarized beam into an azimuthally polarized beam and characterize the performance of magnetic field enhancement and electric field suppression of a realistic metasurface.

Chapter 6: Inspired by unique and compelling traits of orbital angular momentum (OAM) laser beams, such as twisted wavefront and annular-shaped intensity pattern, we design, in this chapter, antennas generating OAM beams at radio frequencies, in particular to tailor antenna's far-field characteristics. We demonstrate that metasurface reflectarray antenna is an efficient apparatus to generate and manipulate OAM-carrying beams at radio frequencies. Novel metasurface reflectarray designs are developed at Ka-band, namely circularly-polarized Bessel-beam and helical-beam reflectarrays radiating cone-shaped patterns and single-feed azimuthal multi-beam reflectarrays, that are potentially beneficial for satellite and wireless communication systems. A parametric study is also conducted to further

characterize the proposed cone-shaped pattern reflectarrays. The OAM approach proposed in this chapter may also provide a vehicle for further developing antennas with complex radiation patterns.

References

[1] B. Memarzadeh and H. Mosallaei, "Array of planar plasmonic scatterers functioning as light concentrator," *Opt. Lett.*, vol. 36, no. 13, pp. 2569–2571, Jul. 2011.

[2] N. Yu *et al.*, "Light Propagation with Phase Discontinuities: Generalized Laws of Reflection and Refraction," *Science*, vol. 334, no. 6054, pp. 333–337, Oct. 2011.

[3] F. Aieta *et al.*, "Aberration-Free Ultrathin Flat Lenses and Axicons at Telecom Wavelengths Based on Plasmonic Metasurfaces," *Nano Lett.*, vol. 12, no. 9, pp. 4932–4936, Sep. 2012.

[4] A. Forouzmand and H. Mosallaei, "A functional metasurface platform with unique building blocks: light manipulation and beam shaping," 2016, vol. 9918, p. 99180Y–99180Y–8.

[5] M. Veysi, C. Guclu, O. Boyraz, and F. Capolino, "Thin anisotropic metasurfaces for simultaneous light focusing and polarization manipulation," *J. Opt. Soc. Am. B*, vol. 32, no. 2, p. 318, Feb. 2015.

[6] M. Veysi, C. Guclu, and F. Capolino, "Vortex beams with strong longitudinally polarized magnetic field and their generation by using metasurfaces," *J. Opt. Soc. Am. B*, vol. 32, no. 2, p. 345, Feb. 2015.

[7] M. Albooyeh *et al.*, "Resonant metasurfaces at oblique incidence: interplay of order and disorder," *Sci. Rep.*, vol. 4, Mar. 2014.

[8] M. Albooyeh, R. Alaee, C. Rockstuhl, and C. Simovski, "Revisiting substrate-induced bianisotropy in metasurfaces," *Phys. Rev. B*, vol. 91, no. 19, p. 195304, May 2015.

[9] V. Asadchy, M. Albooyeh, and S. Tretyakov, "Optical metamirror: all-dielectric frequency-selective mirror with fully controllable reflection phase," *J. Opt. Soc. Am. B*, vol. 33, no. 2, p. A16, Feb. 2016.

[10] J. Huang, "Circularly polarized conical patterns from circular microstrip antennas," *IEEE Trans. Antennas Propag.*, vol. 32, no. 9, pp. 991–994, Sep. 1984.

[11] D. M. Pozar, S. D. Targonski, and H. D. Syrigos, "Design of millimeter wave microstrip reflectarrays," *IEEE Trans. Antennas Propag.*, vol. 45, no. 2, pp. 287–296, 1997.

[12] J. Huang and J. A. Encinar, *Reflectarray antennas*. Piscataway, N.J.; Hoboken, N.J.: IEEE Press ; Wiley-Interscience, 2008.

[13] B. G. Cai, Y. B. Li, W. X. Jiang, Q. Cheng, and T. J. Cui, "Generation of spatial Bessel beams using holographic metasurface," *Opt. Express*, vol. 23, no. 6, p. 7593, Mar. 2015.

[14] J. Wang *et al.*, "Terabit free-space data transmission employing orbital angular momentum multiplexing," *Nat. Photonics*, vol. 6, no. 7, pp. 488–496, Jul. 2012.

[15] A. V. Kildishev, A. Boltasseva, and V. M. Shalaev, "Planar Photonics with Metasurfaces," *Science*, vol. 339, no. 6125, p. 1232009, Mar. 2013.

[16] L. Xu, C. A. Curwen, P. W. C. Hon, Q.-S. Chen, T. Itoh, and B. S. Williams, "Metasurface external cavity laser," *Appl. Phys. Lett.*, vol. 107, no. 22, p. 221105, Nov. 2015.

[17] M. Khorasaninejad *et al.*, "Achromatic Metasurface Lens at Telecommunication Wavelengths," *Nano Lett.*, vol. 15, no. 8, pp. 5358–5362, Aug. 2015.

[18] V. S. Asadchy, M. Albooyeh, S. N. Tcvetkova, A. Díaz-Rubio, Y. Ra'di, and S. A. Tretyakov, "Perfect control of reflection and refraction using spatially dispersive metasurfaces," *Phys. Rev. B*, vol. 94, no. 7, p. 075142, Aug. 2016.

[19] V. Asadchy, M. Albooyeh, and S. Tretyakov, "Optical metamirror: all-dielectric frequency-selective mirror with fully controllable reflection phase," *JOSA B*, vol. 33, no. 2, pp. A16–A20, Feb. 2016.

[20] D. G. Berry, R. G. Malech, and W. A. Kennedy, "The reflectarray antenna," *IEEE Trans Antennas Propagat*, vol. AP-11, pp. 645–651, Nov. 1963.

[21] C. S. Malagisi, "Microstrip disc element reflectarray," *Electron. Aerosp. Syst. Conv.*, pp. 186 – 192, Sep. 1978.

[22] J. P. Montgomery, "A microstrip reflectarray antenna element," *Electron. Aerosp. Syst. Conv. Univ. Ill.*, Sep. 1978.

[23] D. M. Pozar and T. A. Metzler, "Analysis of a reflectarray antenna using microstrip patches of variable size," *Electron. Lett.*, vol. 29, no. 8, pp. 657–658, Apr. 1993.

[24] H. Esfahlani, S. Karkar, H. Lissek, and J. R. Mosig, "Acoustic carpet cloak based on an ultrathin metasurface," *Phys. Rev. B*, vol. 94, no. 1, p. 014302, Jul. 2016.

[25] J. Zhao, *Manipulation of Sound Properties by Acoustic Metasurface and Metastructure*. Springer, 2016.

[26] A. E. Siegman, *Lasers*. University Science Books, 1986.

[27] F. Capolino, *Theory and Phenomena of Metamaterials*. CRC Press, 2009.

[28] N. Engheta and R. W. Ziolkowski, *Metamaterials: Physics and Engineering Explorations*. John Wiley & Sons, 2006.

[29] M. Kamandi, C. Guclu, T. S. Luk, G. T. Wang, and F. Capolino, "Giant field enhancement in longitudinal epsilon-near-zero films," *Phys. Rev. B*, vol. 95, no. 16, p. 161105, Apr. 2017.

[30] M. A. Vincenti, M. Kamandi, D. de Ceglia, C. Guclu, M. Scalora, and F. Capolino, "Second-harmonic generation in longitudinal epsilon-near-zero materials," *Phys. Rev. B*, vol. 96, no. 4, p. 045438, Jul. 2017.

[31] N. Fang, H. Lee, C. Sun, and X. Zhang, "Sub-Diffraction-Limited Optical Imaging with a Silver Superlens," *Science*, vol. 308, no. 5721, pp. 534–537, Apr. 2005.

[32] M. Darvishzadeh-Varcheie and R. Faraji-Dana, “Analysis and design of a multilayer plasmonic superlens by complex images technique,” in *2014 7th International Symposium on Telecommunications (IST)*, 2014, pp. 140–144.

[33] D. Schurig *et al.*, “Metamaterial Electromagnetic Cloak at Microwave Frequencies,” *Science*, vol. 314, no. 5801, pp. 977–980, Nov. 2006.

[34] S. Ahderom, M. Raisi, K. Lo, K. E. Alameh, and R. Mavaddat, “Applications of liquid crystal spatial light modulators in optical communications,” in *5th IEEE International Conference on High Speed Networks and Multimedia Communication (Cat. No.02EX612)*, 2002, pp. 239–242.

[35] N. Yu and F. Capasso, “Flat optics with designer metasurfaces,” *Nat. Mater.*, vol. 13, no. 2, pp. 139–150, Feb. 2014.

[36] F. Monticone, N. M. Estakhri, and A. Alù, “Full Control of Nanoscale Optical Transmission with a Composite Metascreen,” *Phys. Rev. Lett.*, vol. 110, no. 20, p. 203903, May 2013.

[37] C. Pfeiffer and A. Grbic, “Metamaterial Huygens’ Surfaces: Tailoring Wave Fronts with Reflectionless Sheets,” *Phys. Rev. Lett.*, vol. 110, no. 19, p. 197401, May 2013.

[38] S. Liu *et al.*, “Optical magnetic mirrors without metals,” *Optica*, vol. 1, no. 4, pp. 250–256, 2014.

[39] M. Albooyeh, D.-H. Kwon, F. Capolino, and S. A. Tretyakov, “Equivalent realizations of reciprocal metasurfaces: Role of tangential and normal polarization,” *Phys. Rev. B*, vol. 95, no. 11, p. 115435, Mar. 2017.

[40] C. Guclu, V. A. Tamma, H. K. Wickramasinghe, and F. Capolino, “Photoinduced magnetic force between nanostructures,” *Phys. Rev. B*, vol. 92, no. 23, p. 235111, Dec. 2015.

[41] C. Guclu, M. Veysi, and F. Capolino, “Photoinduced Magnetic Nanoprobe Excited by an Azimuthally Polarized Vector Beam,” *ACS Photonics*, vol. 3, no. 11, pp. 2049–2058, Nov. 2016.

[42] M. Veysi, C. Guclu, and F. Capolino, “Focused azimuthally polarized vector beam and spatial magnetic resolution below the diffraction limit,” *J. Opt. Soc. Am. B*, vol. 33, no. 11, p. 2265, Nov. 2016.

[43] C. Guclu, M. Veysi, M. Darvishzadeh-Varcheie, and F. Capolino, “Artificial Magnetism via Nanoantennas under Azimuthally Polarized Vector Beam Illumination,” 2016, p. JW2A.21.

[44] C. Guclu, M. Veysi, M. Darvishzadeh-Vercheie, and F. Capolino, “Optical nanoantennas as magnetic nanoprobes for enhancing light-matter interaction,” in *2016 10th International Congress on Advanced Electromagnetic Materials in Microwaves and Optics (METAMATERIALS)*, 2016, pp. 391–393.

[45] M. Darvishzadeh-Varcheie, C. Guclu, R. Ragan, O. Boyraz, and F. Capolino, “Electric field enhancement with plasmonic colloidal nanoantennas excited by a silicon nitride waveguide,” *Opt. Express*, vol. 24, no. 25, pp. 28337–28352, Dec. 2016.

CHAPTER 2

Thin Anisotropic Metasurface Lenses For Simultaneous Light Focusing And Polarization Manipulation

Sec. 2.1 Motivation

In this chapter, we first investigate the possibility of integration of two important categories of optical components, i.e., circular polarizer and lens, into a thin plasmonic metasurface (MS), for the realistic case when metal losses cannot be neglected (for example when operating in the visible spectrum, or at infrared when non-noble metals are used). Since the circular polarizer and lens are at the heart of many optical systems, the possibility of having both light focusing and polarization manipulation capabilities with a thin single layer plasmonic MS would significantly reduce the cost, volume, optical loss, and system complexity. In this regards, we first develop a theoretical formulation based on phase-amplitude synthesis method for a polarizing lens and then we present an optimal design at mid-infrared ranges near 4.3μm. The first challenge is to find an appropriate nanoantenna which can simultaneously satisfy both a wide reflection phase range and polarization conversion. Hence, an anisotropic nanoantenna, which allows for independent tuning of the

phase changes experienced by the *x*- and *y*-pol. incident fields, is needed. A two-dimensional array of Y-shaped nanoantennas with polarization dependent and spatially varying phase response offers the possibility of balancing the losses experienced by the x- and y-polarized incident fields and is the basis for such a compact polarizing lens. The theory and the example developed here will enable improvement of several devices, such as (i) reflecting/transmitting focusing lenses, (ii) polarizing lenses, (iii) lenses with dual foci, one for each polarization, and (iv) lenses with dual foci one for each wavelength.

We show that anisotropic Y-shaped nanoantennas possess an additional degree of freedom compared to the other nanoantennas studied in the literature such as V-shaped [1]–[3], cross-shaped and rectangular-shaped ones [4]. Such an extra degree of freedom in Y-shaped nanoantennas gives rise to the possibility of balancing the losses experienced by the two orthogonally polarized incident fields that eventually improves the performance of the polarizing lens. In this chapter, nanoantennas are assumed to be made of low cost aluminum with non-negligible loss at mid-infrared to account for the loss in the design process. Although, we focus on the reflection-type geometry due to its high focusing [5], [6] and polarization conversion efficiencies [7], the theory and application of Y-nanoantennas can be straightforwardly extended to the transmission-type geometry.

The outline of the chapter is as follows. We first develop the theory of the proposed polarizing MS lens in Sec. 2.2 where we also proposed and characterize an anisotropic Y-shaped nanoantenna element for the polarizing lens design. To have an engineering guideline, we conduct in Sec. 2.3 a parametric study on the polarizing MS made of Y-shaped elements. We then design and characterize a polarizing lens at infrared range in Sec. 2.4. Conclusions and final remarks are stated in Sec. 2.5.

Sec. 2.2 Theory of Polarizing MS lenses

The proposed polarizing lens design consists of an array of Y-shaped nanoantennas patterned on one side of a dielectric layer deposited onto a metallic ground plane as illustrated in Fig. 2.1. The MS is in the *x*-*y* plane, and it is illuminated by a normally incident slant-polarized plane wave whose transverse–to–*z* electric field phasor is $\mathbf{E}_t^i = E_0(\hat{\mathbf{x}}\cos\varphi_i + \hat{\mathbf{y}}\sin\varphi_i)e^{jkz}$, where E_0 is its magnitude, k is the free-space wavenumber, and φ_i is the angle of the electric field vector with respect to the *x*-axis. In the following we assume a $e^{j\omega t}$ time-harmonic convention with ω being the angular frequency. Here vectors are denoted by bold fonts and unit vectors are denoted by a hat. The transverse-to-*z* electric field phasor of the wave normally reflected by the polarizing lens is

$$\mathbf{E}_t^r = E_1\left(\hat{\mathbf{x}} + \frac{|\Gamma_y|}{|\Gamma_x|}e^{j(\phi_y-\phi_x)}\tan\varphi_i\ \hat{\mathbf{y}}\right);\quad E_1 = E_0|\Gamma_x|\cos\varphi_i\, e^{-jkz}e^{j\phi_x} \tag{2.1}$$

where $\Gamma_{x,y} = |\Gamma_{x,y}|e^{j\phi_{x,y}}$ is the reflection coefficient pertaining to the *x*- and *y*-pol. components, respectively. In order to change the polarization state of the incident wave, we consider here a plasmonic MS made of anisotropic Y-shaped nanoantennas able to manipulate both Γ_x and Γ_y. At a certain wavelength such that the phase difference between the *y*- and *x*-pol. reflection coefficients, $(\phi_y - \phi_x)$, is 90° and the ratio of the wave reflection magnitude for the *y*-pol. to that of *x*-pol. is almost constant, $|\Gamma_y|/|\Gamma_x| = \cot\varphi_i$, the reflected wave is purely left-hand circularly polarized (LHCP). It is purely right-hand circularly polarized (RHCP) when $(\phi_y - \phi_x) = -90°$. Although the above conclusions have been derived for

waves normally reflected from the MS, they are still reasonably valid for reflected waves with small oblique reflection angles (usually less than 30°-40°)

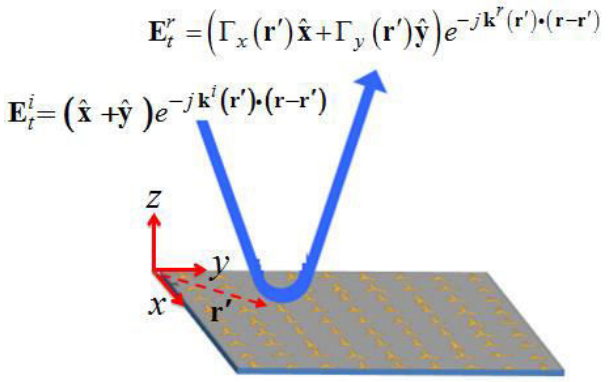

Fig. 2.1 Schematic of a MS composed of Y-shaped nanoantennas illuminated by a plane wave with transverse electric fields shown. The blue line represents a typical incident ray that is locally bended by the MS at a designed angle. The direction of the reflected wavevector, $\mathbf{k}^r = \mathbf{k}_t^r + k_z^r \hat{\mathbf{z}}$, depends on the phase of *x*-pol. and *y*-pol. reflection coefficients.

For a general case, consider a oblique incident ray tube as in Fig. 2.1, propagating with a wavevector, $\mathbf{k}^i$, impinging on the MS and experiencing reflection. The direction of the reflected wave can be controlled based on the generalized Fermat principle [1], [8]–[10] by a proper gradient of the phase of the reflection coefficient. Therefore the reflected beam can be steered toward a desire direction $\mathbf{k}^r$ given by $\mathbf{k}_t^r - \mathbf{k}_t^i = (\partial\phi/\partial x)\hat{\mathbf{x}} + (\partial\phi/\partial y)\hat{\mathbf{y}}$ where $\mathbf{k}_t^i$ and $\mathbf{k}_t^r$ are, respectively, the transverse–to–*z* wavevectors of the incident and reflected fields and $\partial\phi/\partial i = \partial\phi_x/\partial i = \partial\phi_y/\partial i$, $i = x, y$. Note that the condition $\partial\phi_x/\partial i = \partial\phi_y/\partial i$ is straightforwardly obtained by taking the derivative of the polarization conversion condition $(\phi_y - \phi_x) = \pm 90^\circ$. The local values of phase and magnitude of the reflection coefficient are controlled by a proper choice of the unit cell elements of the MS. The

elements should be modulated along the MS to provide the required gradient of the phase ϕ to achieve focusing. In the following element locations are denoted with $\mathbf{r}^{mn} = \mathbf{r}^{00} + ma\hat{\mathbf{x}} + nb\hat{\mathbf{y}}$ where *m* and *n* are integers, *a* and *b* are the local periods along *x* and *y*. Considering the generalized Fermat principle with the discretized MS unit cells, the phase of the reflection coefficient is changed adiabatically along the MS according to the expression

$$\mathbf{k}_t^r = \mathbf{k}_t^i + \left(\frac{\phi^{mn} - \phi^{(m-1)n}}{a} \right) \hat{\mathbf{x}} + \left(\frac{\phi^{mn} - \phi^{m(n-1)}}{b} \right) \hat{\mathbf{y}} \tag{2.2}$$

in order to bend the corresponding ray toward a certain direction $\mathbf{k}^r$. The above procedure is repeated for all other unit cells on the MS and the required phase of the reflection coefficient is found for each element. It is a common procedure to calculate the required reflection coefficient associated to a certain MS unit cell by assuming the MS periodic. This procedure provides accurate results if unit cells change gradually over the MS [10]. If all rays are focused at a certain focal point $\mathbf{r}_f$ the required phase of the reflection coefficient ϕ^{mn} at the *mn*th MS unit cell is found to be [10]

$$\phi^{mn} - \left[k_0 \left| \mathbf{r}^{mn} - \mathbf{r}_f \right| + \mathbf{r}^{mn} . \mathbf{k}^i \right] = 2s\pi + \psi, \quad s = 0,1,.. \tag{2.3}$$

Here, ψ is an arbitrary phase constant, and the subscripts *x* and *y* have been dropped since this equation applies to both polarizations. In summary, the focusing and polarization conversion mechanism of the anisotropic plasmonic metalens under the linearly polarized wave is conceptually described by Eq. (2.1) and (2.3), where two approximations extensively used in reflectarray research have been applied [10]–[15]: (i) the concept of

local periodicity, and (ii) the reflected phases $\phi_{x,y}^{mn}$ are evaluated at normal incidence. The latter approximation has been considered to be accurate especially for small to moderate incidence angles and focal length to diameter ratio larger than unity (in our case f/D=1.25).

Note that all possible polarizations (linearly polarized (LP), RHCP, and LHCP) can be achieved by also adjusting the φ_i angle. To independently vary the reflection phases $_{x,y}$ and amplitudes $\left|\Gamma_{x,y}\right|$ of each principle polarization of the incident wave, along the *x* and *y* directions, each unit cell should possess enough degrees of freedom. Hence, a Y-shaped nanoantenna shown in Fig. 2.2 (a) is utilized as a unit cell. Its symmetric and asymmetric current modes are depicted in Fig. 2.2 (a). Varying Δ and ℓ_1 leads to changes in both the *x*- and *y*-directed current paths. Note that ℓ_2 affects only the extension of the *y*-directed surface current path and has a negligible effect on the asymmetric mode. In the design, first, the two physical parameters of the Y-shaped elements, arm length ℓ_1 and arm angle Δ are tuned to satisfy the focusing condition in Eq. (2-3) for the *x*-pol incident wave at each *mn*th location on the MS as

$$err_{(1)}^{mn}(\Delta,\ell_1)=\left|\phi_x^{mn}-\phi_x^{simulated}(\Delta,\ell_1)\right| \tag{2.4}$$

where $\phi_x^{simulated}$ is phase of the reflected *x*-pol. at the design wavelength λ, obtained from a simulation with the geometrical parameters optimized to meet the required ϕ_x^{mn} from Eq. (2-3). The elements are optimized using the frequency domain finite-element method (FEM) (provided by HFSS by Ansys Inc.) in a fully periodic arrangement (based on local periodicity assumption).

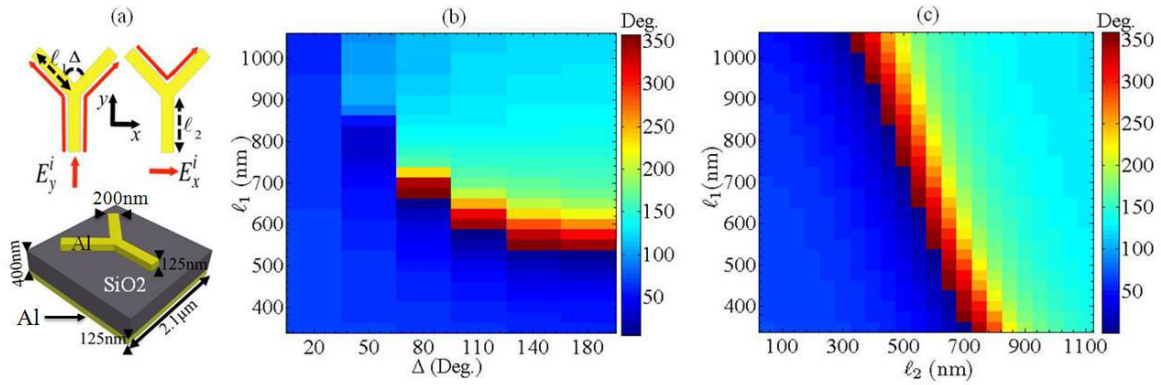

Fig. 2.2 (a) schematic of a MS Y-shaped nanoantenna together with its current distribution for symmetric (top left) and asymmetric modes (top right), and the 3D view of each MS cell (bottom). (b) The reflection phase of the asymmetric mode for a MS made of identical Y-shaped nanoantennas at 4.3μm as a function of the arm length, and the angle between the two arms, Δ, for $\ell_2 = 50nm$. Although results are not plotted here, a similar trend is observed for other values of the stub length ℓ_2 ranging from 50nm to 1100nm. (c) The reflection phase of symmetric mode for a MS made of identical Y-shaped nanoantennas at 4.3μm as a function of the arm length, and stub length, for Δ=110°. The lateral width and thickness of each arm are fixed at 200nm and 125nm, respectively. The complex relative permittivities of the Al and SiO2 at 4.3μm are -1601.3-j609.4 [16] and 1.9-j0.018 [17], respectively.

To achieve circularly polarized focused beam upon reflection from the MS, it is necessary to tailor both the spatial phase and amplitude distributions of the reflected field by tuning each element on the MS. Therefore, the stub length ℓ_2 is then tuned to meet the proper condition for converting the polarization from linear to circular and to meet the focusing condition in Eq. (2-3) also for the *y*-pol. Note that tuning the stub length has a negligible effect on the asymmetric mode of the Y-shaped elements and thus on the *x*-pol. focusing. Therefore, a second error function is defined based on the axial ratio (AR) of the reflected wave as

$$err_{(2)}^{mn}(\Delta, \ell_1, \ell_2) = \left| \pm 1 - AR(\Delta, \ell_1, \ell_2) \right| \tag{2.5}$$

where plus or minus sign stands for a desired LHCP or RHCP, respectively. The AR depends on the physical parameters of the elements and is expressed as

$$AR(\Delta,\ell_1,\ell_2) = -\frac{|E_R(\Delta,\ell_1,\ell_2)|+|E_L(\Delta,\ell_1,\ell_2)|}{|E_R(\Delta,\ell_1,\ell_2)|-|E_L(\Delta,\ell_1,\ell_2)|} \tag{2.6}$$

where E_R and E_L are projections of the reflected electric field $\mathbf{E}_t^r$, [see Eq. (2-1)] onto the RHCP and LHCP unit vectors $\hat{\mathbf{e}}_R = (\hat{\mathbf{x}} - j\,\hat{\mathbf{y}})/\sqrt{2}$ and $\hat{\mathbf{e}}_L = (\hat{\mathbf{x}} + j\,\hat{\mathbf{y}})/\sqrt{2}$, respectively. The AR can be rewritten in terms of linear components as [18]

$$\begin{aligned} AR(\Delta,\ell_1,\ell_2) &= \operatorname{sgn}(\phi_y - \phi_x)\frac{\sqrt{|E_x|^2+|E_y|^2+E'}}{\sqrt{|E_x|^2+|E_y|^2-E'}} \\ E' &= \sqrt{|E_x|^4+|E_y|^4+2|E_x|^2|E_y|^2\cos\left(2(\phi_y-\phi_x)\right)} \end{aligned} \tag{2.7}$$

where $E_{x,y} = |E_{x,y}|e^{j\phi_{x,y}}$ are the *x*- and *y*-pol. components of $\mathbf{E}_t^r$, [see Eq. (2-1)]. Note that for each MS element the phase difference $|\phi_x^{mn} - \phi_y^{mn}|$ between the *x*- and *y*-pol. reflection coefficients is set very close to 90° when minimizing $err_{(2)}^{mn}$ in Eq. (2-5). Therefore, the focusing condition for ϕ_y^{mn} in Eq. (2-3) is automatically satisfied provided that ϕ_x^{mn} satisfies it, as already imposed by Eq. (2-4).

Sec. 2.3 PARAMETRIC STUDY OF A METASURFACE MADE OF Y-SHAPED NANOANTENNAS

The range of phases of the *x*- and *y*-pol. reflection coefficients for a MS made of identical aluminum (Al) Y-shaped nanoantennas as a function of the physical parameters (arm

length, stub length, and arm angle) at λ=4.3μm are shown in Fig. 2.2 (b-c). It is observed that the 360° phase range required for the full control of the wavefront of the reflected wave is achieved. The low loss silica substrate with low dielectric constant (ε_r = 1.9 at λ = 4.3μm) is chosen here instead of higher dielectric constant substrates such as silicon to increase the MS bandwidth and at the same time decrease the rate of variation of reflection phase with the Y-shaped nanoantenna dimensions. The latter effect results in a lower sensitivity to manufacturing tolerances.

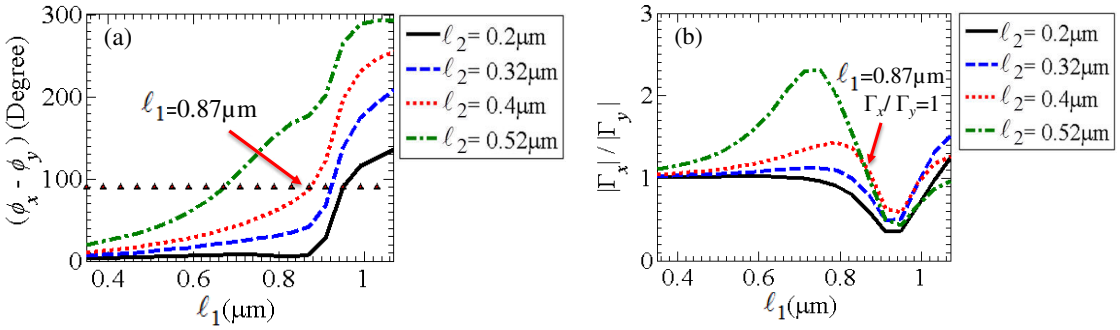

Fig. 2.3 (a) the effect of stub length on the phase difference between the *x*-pol. and *y*-pol. reflection coefficients. The horizontal line shows the 90° phase difference between the *x*-pol. and *y*-pol. reflection coefficients. (b) The effect of stub length on the amplitude ratio of the *x*-pol. to *y*-pol. reflection coefficient. The arm angle, Δ, is fixed at 50°.

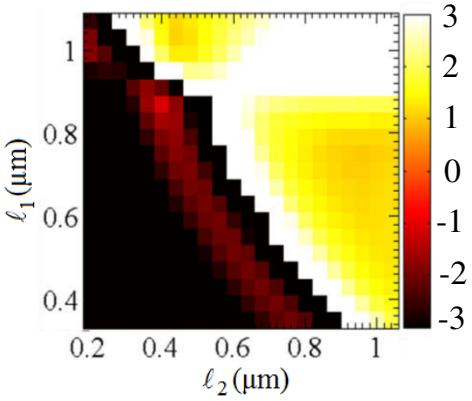

Fig. 2.4 Axial ratio of the reflected wave from a MS consists of an infinite periodic array of identical Y-shaped nanoantennas as a function of the arm length and the stub length. The arm angle, Δ, is fixed at 50°.

The phase difference between the *x*- and *y*-pol. reflection coefficients versus the arm length, ℓ_1, for different stub lengths, ℓ_2, is plotted in Fig. 2.3(a). As the stub length, ℓ_2, increases, the resonant length of the symmetric mode (*y*-directed current mode) increases, while the resonant length of the asymmetric mode (*x*-directed current mode) remains unchanged. Thus, for a given arm length, the phase difference between the *x*- and *y*-pol. reflection coefficients increases as the stub length increases [see Fig. 2.3(a)]. Fig. 2.3(b) also shows the amplitude ratio of the *x*-pol. to the *y*-pol. reflection coefficient versus the arm length, ℓ_1, for different stub lengths, ℓ_2 . For ℓ_2= 0.4μm and ℓ_1= 0.87μm, the amplitude ratio of the *x*-pol. to the *y*-pol. reflection coefficient is equal to 1 and the phase difference between the *x*- and *y*-pol. reflection coefficients is 90° (see Fig. 2.3). Under these conditions, the reflected beam is purely RHCP.

The axial ratio of the reflected wave from a MS made of an infinite periodic array of identical Y-shaped nanoantennas is calculated from Eq. (2-7) and plotted, as a function of the arm length, ℓ_1 , and the stub length, ℓ_2, in Fig. 2.4. Positive and negative axial ratios define the LHCP and the RHCP waves, respectively. Although the results provided in Fig. 2.3 and Fig. 2.4 calculated for a specific value of the arm angle (Δ=50°), similar plots can be obtained for other values of the arm angle. Fig. 2.4 reveals that for arbitrary pairs of the arm length and the arm angle, a proper stub length can be found such that the axial ratio of the reflected wave is positive and its magnitude is less than 1.42 or 3dB (LHCP).

Sec. 2.4 Polarizing Metasurface Lens Design

Based on the results and the theory provided in the previous sections of this chapter, here we show the performance of a designed square, flat, polarizing lens with dimensions

28μm×28μm (6.51λ×6.51λ) with focal length f =35μm, corresponding to a numerical aperture (NA) of 0.37. It is supposed to focus an incident beam with oblique incidence of α=30°, shown in Fig. 2.5(a). The beam waist of the incident Gaussian wave (w_0=25μm) is chosen so that almost the entire surface of the polarizing lens is illuminated by a plane-wave-like wavefront. Fig. 2.5 shows the schematic of the simulation setup together with the intensity of the scattered field in the longitudinal and transverse planes at λ=4.3μm, calculated by FEM full wave simulations (provided by HFSS by Ansys Inc.).

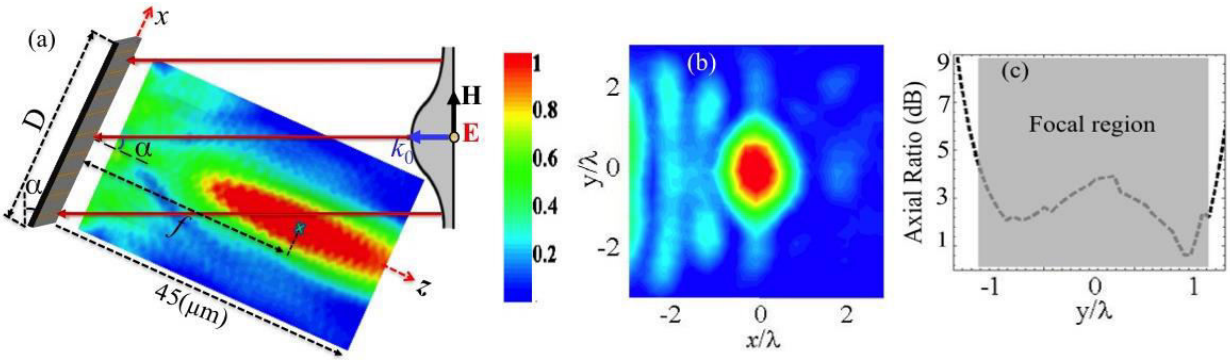

Fig. 2.5 (a) simulation setup together with the full wave simulated results of the normalized scattered field intensity ($|\mathbf{E}|^2/|\mathbf{E}_0|^2$) in x-z plane at λ=4.3μm: for a 28μm by 28μm sized flat polarizing lens with f=35μm, and α=30°, (b) the normalized intensity of the scattered field in x-y transverse focal plane. (c) Axial ratio of the scattered wave along a horizontal line in the focal plane (x=0, z=35μm), the highlighted rectangle shows the focus region.

The focus generated by the MS is clearly observed. The simulation result for the axial ratio of the scattered wave along the y transverse direction, in the focal plane, is plotted in Fig. 2.5(c). The axial ratio is around 3dB in the focal region. The designed polarizing lens preserves good focusing and polarization conversion properties over a relatively broad wavelength range from 3.8μm to 4.8μm. Fig. 2.6 shows the normalized intensity distribution for the scattered field at different incident wavelengths around the central wavelength of 4.3μm.

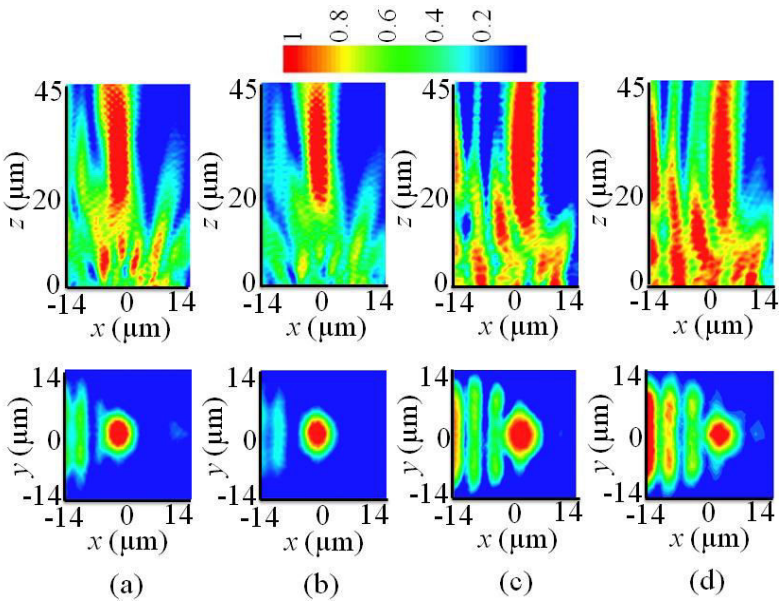

Fig. 2.6 Full wave simulation results of the normalized scattered electric field intensity in the *x*-*z* longitudinal plane (top) and *x*-*y* transverse focal plane, *z*=35μm (bottom) at operating wavelength of (a) 3.8μm, (b) 4μm, (c) 4.6μm, and (d) 4.8μm. Each case has been normalized to its own maximum.

The axial ratio of the scattered field along a *y*-directed line passing through the center of the focal spot in the transverse focal plane is shown in Fig. 2.7. The focal spot slightly shifts in the positive *x*-direction as the wavelength increases from 3.8μm to 4.8μm. This lateral chromatic aberration is mainly attributed to the oblique incidence angle of α=30° [see Fig. 2.5(a)]. In principle, the extra degree of freedom available in Y-shaped nanoantennas allows also to control the phase and amplitude of the reflection coefficient at other wavelengths than the central one, though this capability should be further investigated and may lead to a better control of chromatic aberration.

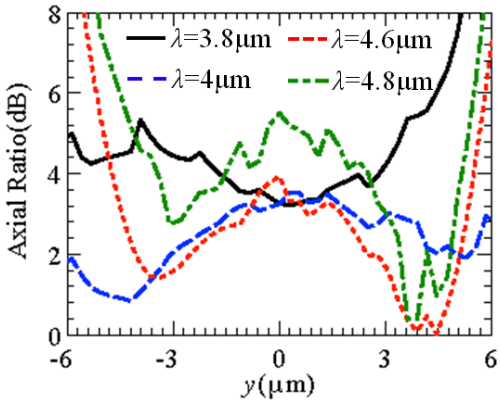

Fig. 2.7 Axial ratio in the focal plane (z=35μm) evaluated along the y-directed line passing through the center of the focal spot. The y-directed line is located at x = 2.5μm, 1.5μm, 1.5μm, 2.5μm for wavelengths 3.8μm, 4μm, 4.6μm, and 4.8μm, respectively.

Fig. 2.8 shows the absorption of the focusing MS, defined as the ratio of the power loss in the MS to the total power illuminating it, versus wavelength. The power lost in the MS is calculated by integrating $0.5\omega\varepsilon''|\mathbf{E}|^2$ over the whole metal volume of the Y-nanoantennas, substrate and ground plane, where ε'' is the imaginary part of the respective material permittivity. Absorption peaks at λ=4.3μm and it is less than 0.36 over a broadband wavelength ranging from 3.8um to 4.8um.

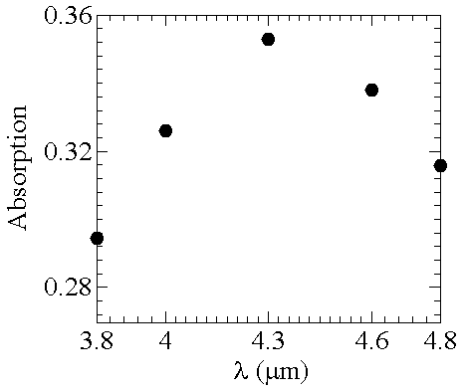

Fig. 2.8 Absorption of the MS-based polarizing lens versus wavelength. Absorption is defined as the power lost in the reflecting MS normalized by the incident power upon the MS.

Note that optical paths from nanoantennas at or close to the edge of the MS to the focal point differ significantly even between neighboring nanoantennas. This requires a large variation of nanoantenna dimensions between neighboring nanoantennas located at or close to the edges [10] to guarantee focusing. Moreover nanoantennas at the MS edges are not surrounded by other nanoantennas on all sides. Therefore the local periodicity assumption discussed earlier in this chapter is invalid for those nanoantennas [10]; as a result, the simulated reflection coefficients used to establish focusing may not model the scattering from these nanoantennas accurately. However, these edge-nanoantennas constitute only a small percentage of the total number of nanoantennas in the MS and their inaccurate modeling does not cause a significant change in the focusing field properties. Increasing the size of the MS not only reduces the effect of undesirable MS edge diffraction on both focusing and polarization conversion but also increases the number of the nanoantennas for which the local periodicity assumption used in the design process is accurate. Larger MSs would improve the polarizing lens performance and result in finer focus spots with smaller axial ratio.

Sec. 2.5 Conclusion

In this chapter, we introduced the concept and the design procedure for flat polarizing metasurface lenses, capable of simultaneous polarization and focusing manipulation, in the presence of non-negligible losses. For this purpose, a planar array of anisotropic Y-shaped nanoantennas is employed to generate light focusing and polarization state conversion because it provides enough degrees of freedom to balance the losses experiences with orthogonal polarizations. Indeed, the Y-shaped nanoantenna allows for the independent

tuning of the phases of both x- and *y*-pol. reflected fields, and at the same time compensate for the natural changes of the magnitude of the reflection coefficient due to losses, which eventually is important to improve the quality of the polarizing lens. The integration of polarizer and lens into a single thin MS layer may have an impact on significantly reducing cost, volume, optical loss, and system complexity.

This chapter is reproduced based on the material in [M. Veysi, C. Guclu, O. Boyraz, and F. Capolino, "A thin anisotropic metasurface for simultaneous light focusing and polarization manipulation," *Journ. Opt. Soc. Am. B*, Vol. 32, No. 2, pp. 318-323, 2015], © Optical Society of America 2015.

References

[1] N. Yu *et al.*, "Light Propagation with Phase Discontinuities: Generalized Laws of Reflection and Refraction," *Science*, vol. 334, no. 6054, pp. 333–337, Oct. 2011.

[2] F. Aieta *et al.*, "Aberration-Free Ultrathin Flat Lenses and Axicons at Telecom Wavelengths Based on Plasmonic Metasurfaces," *Nano Lett.*, vol. 12, no. 9, pp. 4932–4936, Sep. 2012.

[3] P. Genevet *et al.*, "Ultra-thin plasmonic optical vortex plate based on phase discontinuities," *Appl. Phys. Lett.*, vol. 100, no. 1, p. 013101, Jan. 2012.

[4] A. Pors, M. G. Nielsen, G. D. Valle, M. Willatzen, O. Albrektsen, and S. I. Bozhevolnyi, "Plasmonic metamaterial wave retarders in reflection by orthogonally oriented detuned electrical dipoles," *Opt. Lett.*, vol. 36, no. 9, pp. 1626–1628, May 2011.

[5] A. Pors, M. G. Nielsen, R. L. Eriksen, and S. I. Bozhevolnyi, "Broadband Focusing Flat Mirrors Based on Plasmonic Gradient Metasurfaces," *Nano Lett.*, vol. 13, no. 2, pp. 829–834, Feb. 2013.

[6] X. Li, S. Xiao, B. Cai, Q. He, T. J. Cui, and L. Zhou, "Flat metasurfaces to focus electromagnetic waves in reflection geometry," *Opt. Lett.*, vol. 37, no. 23, pp. 4940–4942, Dec. 2012.

[7] D. L. Markovich, A. Andryieuski, M. Zalkovskij, R. Malureanu, and A. V. Lavrinenko, "Metamaterial polarization converter analysis: limits of performance," *Appl. Phys. B*, vol. 112, no. 2, pp. 143–152, Aug. 2013.

[8] Z. Bomzon, G. Biener, V. Kleiner, and E. Hasman, “Radially and azimuthally polarized beams generated by space-variant dielectric subwavelength gratings,” *Opt. Lett.*, vol. 27, no. 5, pp. 285–287, Mar. 2002.

[9] Z. Bomzon, G. Biener, V. Kleiner, and E. Hasman, “Radially and azimuthally polarized beams generated by space-variant dielectric subwavelength gratings,” *Opt. Lett.*, vol. 27, no. 5, pp. 285–287, Mar. 2002.

[10] J. Huang and J. A. Encinar, *Reflectarray antennas*. Piscataway, N.J.; Hoboken, N.J.: IEEE Press ; Wiley-Interscience, 2008.

[11] B. Memarzadeh and H. Mosallaei, “Array of planar plasmonic scatterers functioning as light concentrator,” *Opt. Lett.*, vol. 36, no. 13, pp. 2569–2571, Jul. 2011.

[12] M. Farmahini-Farahani and H. Mosallaei, “Birefringent reflectarray metasurface for beam engineering in infrared,” *Opt. Lett.*, vol. 38, no. 4, pp. 462–464, Feb. 2013.

[13] A. Forouzmand and H. Mosallaei, “A functional metasurface platform with unique building blocks: light manipulation and beam shaping,” 2016, vol. 9918, p. 99180Y–99180Y–8.

[14] A. Forouzmand, S. Tao, S. Jafar-Zanjani, J. Cheng, M. M. Salary, and H. Mosallaei, “Double split-loop resonators as building blocks of metasurfaces for light manipulation: bending, focusing, and flat-top generation,” *J. Opt. Soc. Am. B*, vol. 33, no. 7, p. 1411, Jul. 2016.

[15] A. Forouzmand and H. Mosallaei, “Real-time controllable and multi-functional metasurfaces utilizing indium tin oxide materials: A phased array perspective,” *IEEE Trans. Nanotechnol.*, vol. PP, no. 99, pp. 1–1, 2017.

[16] A. D. Raki, A. B. Djurii, J. M. Elazar, and M. L. Majewski, “Optical properties of metallic films for vertical-cavity optoelectronic devices,” *Appl. Opt.*, vol. 37, no. 22, pp. 5271–5283, Aug. 1998.

[17] R. Kitamura, L. Pilon, and M. Jonasz, “Optical constants of silica glass from extreme ultraviolet to far infrared at near room temperature,” *Appl. Opt.*, vol. 46, no. 33, pp. 8118–8133, Nov. 2007.

[18] Constantine A. Balanis, “Antenna Theory: Analysis and Design", Wiley: 4th Edition.

CHAPTER 3

Metasurface Lens with an Elongated Needle-shaped Focus

Sec. 3.1 Motivation

Increasing depth of focus (DOF) without losing lateral spatial resolution has been a classical challenge in optical systems such as data recording systems and microscopy [1]–[5]. Particularly, a shallow DOF limits the capability of the imaging systems for thick specimen. Therefore such systems usually use "optical sectioning" technique [6], [7] by moving the specimen along the beam axis. Different extended DOF algorithms are then employed to restore a single image of the specimen from a range of images taken at different positions of the specimen along the beam axis [8]. Another approach to overcome the shallow DOF barrier is to use a variable focus hologram together with a restoring extended DOF algorithm while keeping the specimen position fixed on the beam axis [9]. To reduce the complexity of such focal scanning systems, a particular class of lenses with a single focal region featuring a narrow lateral width and an elongated DOF is employed for data recording systems and microscopy [10]–[12]. Such lenses with a long DOF provide a longer interaction range between the focused beam and the specimen in optical systems

and therefore remedy the problems caused by the specimen being out of focus. In this regard, the use of optical power absorbing apodizers has been thoroughly examined to increase the DOF in optical systems [12], [13]. It has been also demonstrated that upon focusing optical vector beam modes with annular intensity shape possessing radial [14]–[16] and azimuthal [17]–[19] polarizations through a conventional lens, a focal region is achieved with a very long DOF and narrow lateral full width at half maximum (FWHM). The narrower the annular-width of the incident radially polarized beam the longer the DOF. However, these methods usually suffer from a decrease of the optical power in the focal plane due to the partial blockage of the illuminating beam. Recently, a method based on optical "super-oscillations" (see [20] for more details) has been developed to generate a needle-shaped focus with a spot size smaller than the diffraction limit and a DOF of ~15λ [21]. However, such technique usually suffers from high intensity side lobes surrounding the focal region.

In this chapter, we demonstrate that a single elongated focal range with a very narrow lateral FWHM is obtained by generating multiple overlapping foci using, for the first time to the authors' knowledge, a novel multifocal metasurface (MS) lens. The techniques described here together with its realization using MS technology (that provides independent control of phase, amplitude, and polarization of the illuminating beam) would result in an extended DOF with reduced power loss. The only source of the power loss in our proposed method is the metal losses, which cannot be neglected when operating in the visible spectrum or at infrared when non-noble metals are used. Note that a multifocal lens by itself is an important optical component and is at the heart of many optical devices, such as multifocal plane microscopy [22], [23], dual field-of-view optical imaging systems [24],

digital versatile disc (DVD) drivers [25], optical coherence tomography (OCT) imaging systems, and intraocular contact lenses [26]. A conventional bifocal 3D lens is realized by dividing the lens aperture into two sub lenses: (i) a central zone with focal distance f1 and (ii) a peripheral concentric zone with focal distance f_2 greater than f_1 [27], in which the incident beam illuminates the central and peripheral zones of the lens with a specific power proportion. In addition, conventional multifocal lenses are usually designed based on diffractive optics approach and found their use in many practical applications [28].

The novel multifocal MS lenses proposed here have a flat, compact configuration and therefore are easier to fabricate and integrate in nanophotonic systems as compared to their conventional bulky counterparts. In addition, they provide more functionalities by allowing to independently tailor not only the local phase and amplitude but also the polarization of the beam [29]. In order to design proposed multifocal MS lenses, two techniques are investigated here: (i) polarization-diversity [simultaneous focusing of two orthogonal linearly polarized incident beams at two distinct foci, as shown in Fig. 3.1 (a)] that uses the overall lens aperture, and (ii) annular-segmentation [dividing the lens aperture into multiple concentric sub-lenses that converge the incident beam at distinct foci, as shown in Fig. 3.1(b)]. We also describe a novel combination of these two techniques either with spatially-separated foci [see Fig. 3.1(c)] or with a single needle-like focal region with an elongated DOF. Recently, with the availability of planar fabrication technologies, various flat optics devices have been developed and received increasing attention in modern optics and photonics. In particular, flat monofocal MS lenses comprising nanoantennas have been extensively investigated in the literature [30]–[32], however such designs usually have a shallow DOF. It has been recently demonstrated that a flat MS lens

forms a single focal range with a DOF of about 21λ and a lateral FWHM of 1.8λ (at λ=425μm) by properly tailoring the local phase and amplitude of the scattered field from the MS lens through an iterative phase-amplitude optimization algorithm [33]. However, due to the large number of elements on the MS lens, more than hundreds of elements, it would be difficult and time consuming to optimize the phase of reflection/transmission coefficient at all MS elements using local or global search algorithms.

In this chapter, we employ the flat MS lens technology due to its flexibilities in the engineering of the focal intensity profile by spatially tailoring the local phase, amplitude and polarization state of the incident beam. Note that, in principle, MSs can be realized either with metallic or dielectric nanoantennas. First, we design a novel bifocal flat MS lens based on the first technique, the polarization-diversity technique illustrated in Fig. 3.1(a). A slant-polarized incident beam (here represented as a superposition of two x'-pol. and y'-pol. beams such that the projections of the incident electric field on the x- and y-axes are of equal amplitude and phase) illuminates the bifocal MS lens. The angle of incidence defined as the angle between the beam axis z' and the MS normal z is α. The lens focuses the two orthogonally polarized linear components of the incident beam at two spatially separated foci whose separation is determined by the design. Upon choosing the proper separation distance of these two orthogonally polarized foci, a needle-like intensity profile forms along the axis of propagation with a very fine lateral resolution and an extended DOF. The simple design procedure makes this method promising for applications which are sensitive to intensity rather than polarization such as microscopy and data storage devices to name a few.

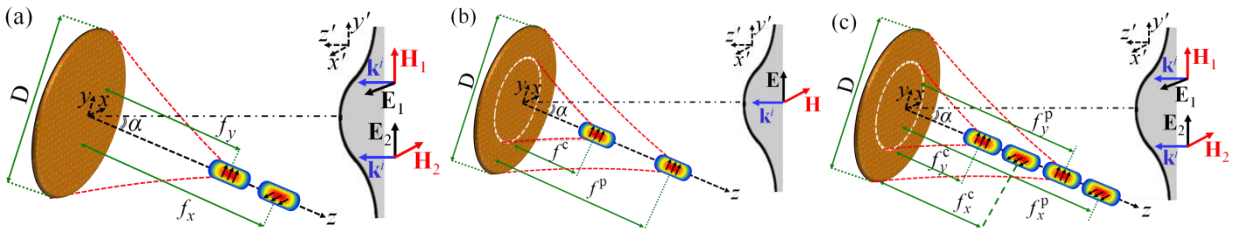

Fig. 3.1 Schematic of representative multifocal MS lenses based on (a) polarization-diversity technique, (b) annular-segmentation technique (in this representative example, the lens aperture is divided into two concentric annular segments, central and peripheral segments, focusing the illuminating beam onto two well-separated foci), and (c) combined polarization-diversity annular-segmentation technique. The illuminating beam is defined in the primed coordinate system and the x'-axis is aligned with the x-axis while the angle between the z-axis and the z'-axis is α. The subscripts x and y refer to the electric field polarization direction, and the superscripts c and p refer to the central and peripheral MS segments.

Next, the multifocal lens concept is further developed via the second technique discussed here, the annular-segmentation technique as illustrated in Fig. 3.1(b), in which the lens aperture divides into separate concentric annular sub-MSs. Different portions of the incident beam illuminate different sub-MSs and thus are focused into different closely-spaced/separated foci. In conventional multifocal diffractive lenses, foci are symmetrically distributed and equally spaced on the beam axis around the zeroth diffractive order focus, which is the focus corresponding to the rays diffracted according to the conventional Snell's law. In contrast, the foci locations and separations for the flat multifocal circular lens proposed in this paper can be chosen arbitrarily in three-dimensional space. Furthermore, a lens with an extraordinarily elongated DOF is realized with the combination of the two techniques just described: polarization-diversity and annular-segmentation, in such a way that each sub-MS exhibits two foci for two orthogonal linearly polarized components of the illuminating beam [see Fig. 3.1(c)]. Simulation results show that the proposed multifocal

lens design procedure, albeit simple and time-effective, is a great candidate for the design of various versions of multifocal lenses and monofocal lenses with elongated DOF. Note that although we here utilize the reflection-type geometry due to its high efficiency and polarization conversion efficiencies, the techniques proposed in this paper (see Fig. 3.1) can be straightforwardly extended to the transmission-type geometry using highly efficient metallic and dielectric MSs.

Sec. 3.2 Polarization-Diversity Technique

First, the concept of polarizing lens introduced in the chapter. 2 is extended here to the investigation and development of bifocal lenses. Let us denote the coordinates of the center of MS cells with $\mathbf{r}^{mn} = \mathbf{r}^{00} + ma\hat{\mathbf{x}} + nb\hat{\mathbf{y}}$ where *m* and *n* are integers that denote MS cells, *a* and *b* denote the unit cell periods along the *x* and *y* directions, respectively. In order to refract an incident ray propagating with the wave vector $\mathbf{k}^i$ onto a point-like spot at $\mathbf{r}_f$, the required local phase of the reflection coefficient at the *mn*th MS cell, denoted by ϕ^{mn}, can be found as [34]

$$\phi^{mn} - \left[k_0 \left| \mathbf{r}^{mn} - \mathbf{r}_f \right| + \mathbf{r}^{mn} \cdot \mathbf{k}^i \right] = 2s\pi + \psi, \tag{3.1}$$

where $s = 0, \pm 1, \ldots$ is an arbitrary integer and ψ is an arbitrary phase offset, constant with varying *n* and *m*. Note that this equation holds for both *x* and *y* polarizations, and different $\mathbf{r}_f$ can be chosen depending on different polarizations. The proposed flat MS lens consists of anisotropic Y-shaped nanoantennas. The advantages of these Y-shaped nanoantennas compared to the previously employed V-shaped designs as in [30] consist in having an

extra degree of freedom (stub length) that helps in balancing the reflection intensities of x- and y-polarized waves and having two different and independent reflection phase profiles for two orthogonal linear polarizations. The Y-shaped nanoantennas as discussed in chapter 2 are made of Al and patterned on one side of a silica substrate with thickness of 400nm, while a sufficiently thick aluminum layer is deposited on the other side of the substrate to act as a ground plane. In this chapter, the operating wavelength of the MS lens is 4.3μm. Fig. 3.2(a) shows the geometry of the Y-shaped nanoantenna together with the current paths for symmetric and anti-symmetric resonance modes that correspond to *y* and *x* polarized electric fields, respectively. While tuning the arm angle and the arm length l_1 changes both the reflection coefficients of *x*- and *y*-polarized waves, tuning the stub length l_2 mainly changes the *y*-polarized wave's reflection coefficient and has a slight effect on the *x*-polarized wave's reflection coefficient (anti-symmetric mode). In order to focus the slant-polarized incident beam (i.e., the projections of the incident electric field on the *x*- and *y*-axes are of equal amplitude and phase) onto two foci at locations $\mathbf{r}_{f_x}$ and $\mathbf{r}_{f_y}$ upon reflection, the physical parameters of the Y-shaped element at *mn*th cell's location on the MS must be properly tuned. It is required that the simulated reflection phases from the *mn*th element for both principal polarizations (ϕ_x^{sim} and ϕ_y^{sim}) meet the required phases of the reflection coefficients at *mn*th location (ϕ_x^{sim} and ϕ_y^{sim}) from Eq. (3-1).

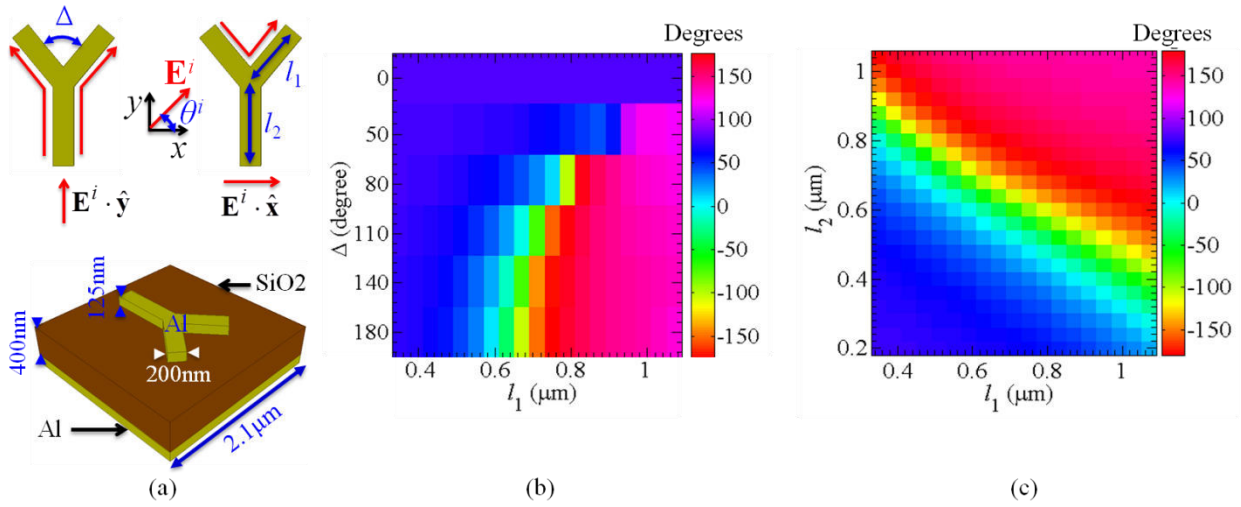

Fig. 3.2 (a) Geometry of a Y-shaped nanoantenna together with its current distribution for symmetric (top left) and anti-symmetric modes (top right), and the 3D view of each MS cell (bottom). (b) Reflection phase of the anti-symmetric mode, upon x-polarized incidence, for a MS made of identical Y-shaped nanoantennas at 4.3μm as a function of the arm length, l_1, and the angle between the two arms, Δ, for l_2= 200nm. Results for other values of the stub length l_2 ranging from 50nm to 1100nm provide analogous trends not shown here for simplicity. (c) Reflection phase of symmetric mode, upon y-polarized incidence, for a MS made of identical Y-shaped nanoantennas at 4.3μm as a function of the arm length l_1, and stub length l_2, for Δ=80°. In Fig. 3.2(a) we keep the arm angle fixed at Δ=80°, however the reflection phase of the symmetric mode also changes in a similar manner when using other values of the arm angle Δ, which is not shown here for brevity. The lateral width and thickness of each arm are fixed at 200nm and 125nm, respectively. The complex relative permittivities of the Al and SiO2 at 4.3μm are -1601.3-j609.4 and 1.9-j0.018, respectively.

Owing to the three physical parameters of the Y-shaped nanoantenna, we have enough degrees of freedom to control the reflection coefficients of orthogonally polarized incident waves almost independently. Fig. 3.2(b-c) shows the range of phases of the *x*- and *y*-polarized waves' reflection coefficients (ϕ_x^{sim} and ϕ_y^{sim}) as a function of the Y-shaped nanoantenna's design parameters ($l_1, l_2,$ and Δ) at 4.3μm. The frequency domain finite-element method (FEM) (commercially available in HFSS by Ansys Inc.) is used to simulate the Y-shaped nanoantennas in a fully periodic arrangement with normal incidence

illumination, applying the local periodicity assumption. The bifocal lens is subsequently designed to work under beam incidence angle of $\alpha = 30°$ (i.e., the beam is coming at an angle of $\alpha = 30°$ from the MS normal, *z*-axis) as shown in Fig. 3.1(a). In this figure, the slant-polarized beam impinges on the lens with an electric field vector having two orthogonal *x*- and *y*-polarized components with identical amplitude and phase. Upon reflection from the lens surface, the *x*- and *y*-polarized components of the incident beam are focused into two spatially separated spots at $\mathbf{r}_{f_x} = f_x\hat{\mathbf{z}}$ and $\mathbf{r}_{f_y} = f_y\hat{\mathbf{z}}$, respectively. Based on the element characterization provided in Fig. 3.2(b-c) and using Eq. (3-1), an illustrative flat bifocal circular lens of radius 25λ (wavelength is λ=4.3μm) is designed to have foci at $f_x = 42.8\lambda$ (numerical aperture, NA, of $NA_x = 0.5$) and $f_y = 89.5\lambda$ ($NA_y = 0.27$). The transverse scattered electric field within the focal range is numerically computed from the transverse electric field on the MS by using the plane wave spectrum decomposition. The corresponding longitudinal component of the scattered electric field is also found by applying Maxwell's divergence equation in the spectral domain followed by an inverse Fourier transform. The Fourier and inverse Fourier transform integrals in plane wave spectral calculations (see Eqs. (24)-(25) in [17]) are implemented numerically via a two-dimensional FFT algorithm where the size of the spatial domain size and spatial resolution are $102.4\lambda \times 102.4\lambda$ and $\lambda/20$, respectively. The transverse field on the MS lens is stepwise approximated and the reflected electric field at each MS cell is assumed uniform and equal to the reflected electric field calculated via the simulated reflection coefficient of the element multiplied by the transverse incident field at the center of the cell.

The electric field is assumed null outside of the overall MS equivalent aperture. A linearly polarized Gaussian beam, whose electric field and power density at the beam center are $1\mathrm{V/m}$ and $1.32\mathrm{mW/m^2}$, respectively, illuminates the MS lens with $\alpha = 30°$ angle of incidence. The total power carried by the beam is $246.8\mathrm{pW}$, which is calculated by the surface integral of its longitudinal Poynting vector. The beam waist of the incident Gaussian beam in the MS plane is chosen three times larger than the radius of the MS ($w_0 = 75\lambda$) such that incident beam has a plane-wave-like wavefront over the entire aperture of the lens. The intensities of the *x*- and *y*-polarized scattered fields in the longitudinal plane (*x*-*z* plane) are shown in Fig. 3.3(a)-(b). The slant-polarized incident beam is focused onto two spatially separated foci having different polarizations, i.e., *x*- and *y*-polarized. Note that the actual foci centers observed in Fig. 3.3 (obtained by PWS calculations) occurring at 42.5λ and 89.1λ slightly deviate from the designed geometrical point-like spot at 42.8λ and 89.3λ [used in Eq. (3-1)]. The larger the lens diameter the smaller the difference between the designed geometrical focal distances and the actual ones. Note that such a shift occurs in all the reported cases in this thesis. Since the bifocal lens has a higher NA for the *x*-polarized component of the incident field, the *x*-polarized spot (located closer to the lens) has a narrower lateral FWHM and shorter DOF compared to the *y*-polarized spot (the farther spot). The designed bifocal lens also works as a monofocal lens for an incident beam that is polarized purely either along *x*′- or *y*′-axis.

In the next step, the farther spot at f_y is placed very close to the closer spot at f_x aiming at increasing the DOF. The design parameters of the Y-shaped nanoantennas on the

MS are locally modified based on the aforementioned algorithm such that now we have two foci designed to be at $f_x = 42.8\lambda$ $\left(NA_x = 0.5\right)$, and $f_y = 47.7\lambda$ $\left(NA_y = 0.46\right)$.

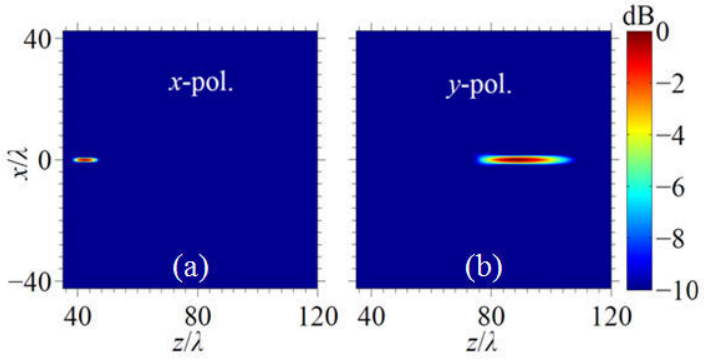

Fig. 3.3 Simulation results for an illustrative bifocal MS lens shown in Fig. 3.1(a) (with two well-separated foci of orthogonal polarizations) of radius 25λ, placed at the z = 0 transverse plane, upon plane wave incidence from an angle $\alpha = 30°$ in the x-z plane, at $\lambda = 4.3\mu m$. The projections of the incident electric field on the x-and y-axes are of equal amplitude and phase. The intensity (normalized to its maximum) of (a) the x-polarized scattered field and (b) the y-polarized scattered field, in the x-z longitudinal plane: $f_x = 42.8\lambda$ $\left(NA_x = 0.5\right)$, $f_y = 89.5\lambda$ $\left(NA_y = 0.27\right)$.

Under the slant-polarized incident beam illumination with the incidence angle of $\alpha = 30°$ with respect to the MS normal, we plot the intensity maps of the x- and y-component of the scattered electric field in Fig. 3.4(a-b), respectively. Moreover, the intensity of the total scattered electric field vector, accounting also for the longitudinal component, is reported in Fig. 3.4(c). The foci of different polarizations are at distinct locations whereas the focal range for the total field intensity extends over the two foci. The overall focal region has a uniform intensity distribution with a lateral FWHM of less than λ and a DOF, axial FWHM, of about 10.1λ (extends from z=40.4λ to 50.5λ). The proposed bifocal lens has a single elongated focal region [Fig. 3.4(c)] with a DOF which is 1.6 times longer than that of a simple monofocal lens of the same aperture size [Fig. 3.4(a-b)], while

the lateral FWHM is kept almost the same. In other words, the bifocal lens designed based on the polarization-diversity technique increases the DOF without compromising the lateral resolution and aperture efficiency of the monofocal lens of the same aperture size. Although the polarization diversity technique is used here to generate linearly-polarized spatially-separated foci with orthogonal polarization vectors, such technique can be straightforwardly used with other pairs of orthogonal polarizations, such as right- and left-hand circularly polarized beams, by employing a proper MS element. However, this should be further investigated in a future publication.

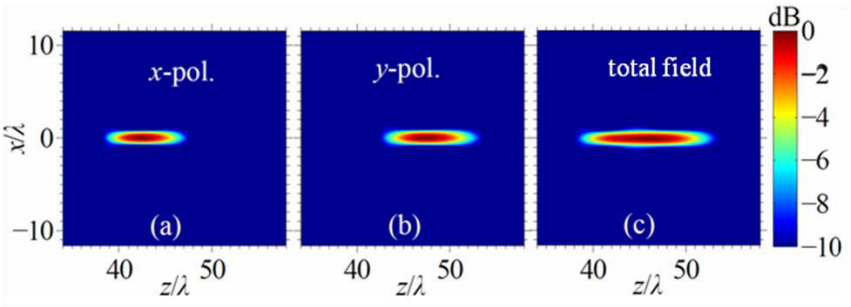

Fig. 3.4 Simulation results for an illustrative bifocal MS lens (with two overlapping foci of orthogonal polarizations) of radius 25λ featuring a single elongated focal region and operating at 4.3μm with: $f_x = 42.8\lambda$, $f_y = 47.7\lambda$. The illuminating beam has slant polarization and its incidence angle is set at $\alpha = 30°$. Intensity (normalized to its maximum) of (a) *x*-polarized scattered field, (b) *y*-polarized scattered field, and (c) total scattered field in the *x*-*z* longitudinal plane.

Sec. 3.3 Annular-Segmentation Technique

In order to further extend the DOF of the lens, an annular-segmentation technique is proposed such that the circular MS lens aperture is divided into a few annular regions, each region associated to an individual focal spot. In contrast to the polarization-only technique proposed in the previous section, which only offers two degrees of freedom (bifocal lenses), the annular-segmentation technique simply offers an increase in the degrees of

freedom. By allowing extra foci, we design multiple overlapping foci that collapse into a needle-like focal region with elongated DOF. Here, we need to make an important remark regarding the superposition of fields scattered by different sub-MSs along the focal axis. In contrast to the polarization-diversity technique, the annular-segmentation technique leads to foci mainly with the same polarization. The co-polarized fields scattered from different sub-MSs are not necessarily in phase all along the focal range. Therefore, when using only annular-segmentation technique, it is difficult to avoid destructive interference, which would inhibit a single elongated focal region with uniform intensity distribution by bringing multiple foci close to each other. To demonstrate this, a representative circular flat lens consisting of two concentric sub-MS regions of outer radii and r^{c}, r^{p} where superscripts *c* and *p* refer to the central and peripheral sub-MS regions respectively [see Fig. 3.1(b) and Fig. 3.5(a)], is designed to work under *y*′-polarized incident beam only. Therefore, the electric field at the foci is mainly *y*-polarized. The Y-shaped MS elements are oriented as in Fig. 3.5(a). The electric field scattered only from the central (peripheral) sub-MS is calculated by setting the field amplitude on the peripheral (central) sub-MS to zero. The outer radius of the peripheral sub-MS and the geometrical focus for the central sub-MS are fixed at $r^{\mathrm{p}} = 17.5\lambda$ and $f^{\mathrm{c}} = 30\lambda$, respectively. The outer radius of the central sub-MS and the geometrical focus for the peripheral sub-MS are then tuned such that the maximum magnitudes of the scattered fields from the central and peripheral sub-MSs are almost equal at their individual focal distances. Furthermore, field amplitudes are designed to drop to around half of their peak field amplitude between the two foci (here at the distance of $z = 38.3\lambda$). For constructive superposition, it is important for these two contributions to

be in phase at $z = 38.3\lambda$. Fig. 3.5(b) shows the scattered field intensity (normalized to its maximum) from the overall lens aperture on the *x*-*z* longitudinal plane.

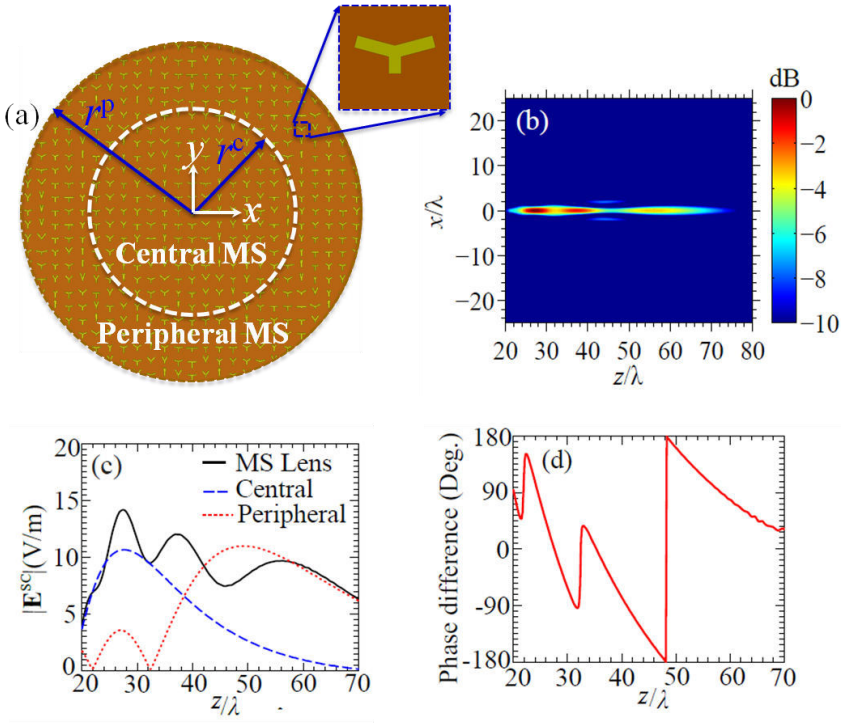

Fig. 3.5 (a) Geometry of a circular flat MS lens operating at that consists of two annular sub-MSs and (b) normalized total scattered field intensity from the MS lens illuminated by a *y*′-polarized incident beam with the incidence angle of with respect to MS normal [see Fig. 3.1]. The electric field intensity plot is normalized to the maximum intensity within the focal range. (c) Magnitude of the electric field scattered from the central, the peripheral and the overall MSs along the focal axis (*z*-axis). (d) Phase difference between the electric fields scattered from the central and peripheral sub-MSs along the focal axis. The MS is located at *z*=0 transverse *x*-*y* plane and the outer radii and the designed focal distances corresponding to central and peripheral sub-MSs are set as: $r^c = 10.3\lambda$, $r^p = 17.5\lambda$ $f^c = 30\lambda$, $f^p = 53\lambda$.

It is observed that the scattered field intensity from overall MS lens drops by about 5.6dB at the distance *z* = 46.3λ away from the MS with respect to the maximum scattered field intensity along the focal *z*-axis that occurs at z = 27.5λ. The magnitude of the electric fields scattered from the central and peripheral sub-MSs together with the magnitude of

the electric field scattered from the overall MS aperture are plotted in Fig. 3.5(c). We observe that the fields due to the central and peripheral sub MSs are in comparable amplitude, thus the dip in the total field is attributable to a degree of destructive interference. Note that although the maximum magnitude of the focal fields focused by the central and the peripheral sub-MSs are almost equal (see Fig. 3.5), the axial FWHM (i.e., the DOF) of the focal field for the peripheral sub-MS is longer than that for the central sub-MS. This is attributed to the fact that the peripheral sub-MS lens has a lower NA (i.e., a wider focus) and a higher incident illumination power (i.e., higher scattered field power) as compared to the central sub-MS lens. The phase difference between the electric fields scattered from the central and peripheral sub-MSs is also plotted in Fig. 3.5(d). This plot clearly shows that the fields scattered from the central and peripheral sub-MSs possess a varying phase difference along the *z*-axis, therefore it is not easy to guarantee constructive interference between the fields scattered from two sub-MSs and uniform focal field amplitude along the *z*-axis. This fact is clearly noticed at around $z = 48\lambda$ marking the destructive interference since the phase difference is 180°. Based on this remark, in the next section we design the multifocal lens with the combination of the polarization-diversity and the annular-segmentation techniques to eliminate the destructive interference and achieve a flat intensity profile along the extended DOF. Note that for a given MS lens radius, the number of foci can be increased by increasing the number of annular sub-MSs in Fig. 3.5(a). However an important limitation must be kept in mind: the annular width of each sub-MS must be large enough such that the local periodicity assumption remains valid (note that nanoantennas' dimensions might change considerably from one sub-MS to another since each sub-MS has a distinct focal distance). Note that the

scattered field polarization upon reflection from the elements is mainly the same as the incident field polarization when the latter is polarized along the symmetry axis (*y*-axis) or along the asymmetry axis (*x*-axis) of the Y-shaped elements (similarly to the V-shaped elements [30]). Moreover, since the plane of incidence (*yz*) coincides with the symmetry plane of the Y-shaped elements, the MS lens is also symmetric with respect to the incidence (*yz*) plane. Due to these symmetry properties the cross-polarized scattered field is minimized.

Sec. 3.4 Metasurface Lens With a Single Elongated DOF

In this section, we combine the polarization-diversity and annular-segmentation techniques to design a lens with an overall single focal region with an elongated DOF. This is achieved by exploiting the degrees of freedom offered by the Y-shaped nanoantennas. The proposed lens aperture consists of two concentric sub-MSs, each with two separate foci of different polarizations, leads to a total of four foci. Importantly, consecutive foci along the focal axis are always chosen from orthogonal polarization, such that the focal fields with the same polarization and scattered from separate sub MSs are farther separated to minimize destructive interference wherever they are in comparable amplitudes. Next, we optimize the *x*- and *y*-polarized focal distances and the outer radius of central sub-MS to achieve a single focal region with uniform intensity distribution and elongated DOF. Considering the dependence of the spot size and DOF on the ratio of focal distance to lens diameter (i.e., the NA), the peripheral sub-MS (which has a larger diameter) is set to obtain the focus with the longer focal distance such that an overall focal region with uniform transverse resolution is achieved. The outer radius of peripheral sub-

MS is also fixed at 17.5λ. The radius of central sub-MS and the distances of the corresponding *x*- and *y*-polarized foci for each sub-MS are selected by minimizing the error function defined as

$$error = \frac{\max\left\{\left|\mathbf{E}(0,0,z)\right|^2\right\} - \min\left\{\left|\mathbf{E}(0,0,z)\right|^2\right\}}{\text{mean}\left\{\left|\mathbf{E}(0,0,z)\right|^2\right\}} \tag{3.2}$$

where $z \in [30\lambda, 80\lambda]$, $f_x^{\text{c}} < f_y^{\text{c}} < f_x^{\text{p}} < f_y^{\text{p}}$, (in which subscripts *x* and *y* denote the polarization) $\mathbf{E}(0,0,z)$ is the total electric field vector on the *z*-axis (focal axis), and mean function $\text{mean}\{\cdot\}$ represents the average over $z \in [30\lambda, 80\lambda]$. In this procedure, we use the genetic algorithm technique to minimize the error function in Eq. (3-2), where the number of sampling points along the *z*-axis is 51. The field $\mathbf{E}(0,0,z)$ is evaluated using plane-wave spectrum decomposition where the field on MS is step-wise approximated as explained in the previous section of this chapter and in [17]. The optimal design in the end consists of two annular regions of outer radii 10.7λ and 17.5λ whose expected geometrical foci are allocated, respectively, at $f_x^{\text{c}} = 40.2\lambda$, $f_y^{\text{c}} = 50.5\lambda$, $f_x^{\text{p}} = 71.4\lambda$, and $f_y^{\text{p}} = 78.4\lambda$. The scattered field intensity (normalized to its maximum) on the *x*-*z* longitudinal plane and along the *z*-axis are reported in Fig. 3.6 (a) and (b), respectively. In the end, a needle shape focal region with axial FWHM (DOF) of about 74.1λ (extending from *z*=27.7λ to 101.8λ) is formed.

A very shallow dip of about -0.58dB (with respect to the maximum scattered field intensity) along the focal axis (*z*-axis) is observed at distance *z*=50λ away from the MS [marked as III in Fig. 3.6 (b)]. The NA of the lens, considering the center of the focal region as the effective focal point, is about 0.26. The reported elongated DOF of ~74.1λ is much

longer than the theoretical DOF of a conventional lens (i.e., $n\lambda / NA^2$ in which n is refractive index of the host medium) which is ~14.8λ. In Fig. 3.6 (c-g) we report the field intensity maps on different x-y transverse planes at z locations within the focal range, marked by roman numerals in Fig. 3.6(b).

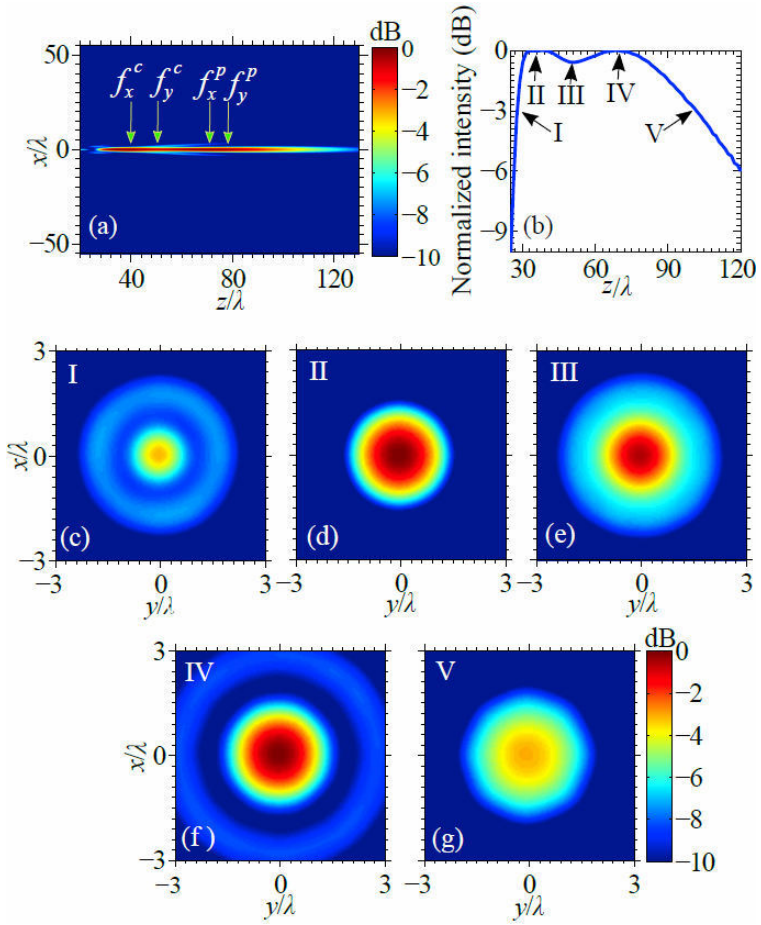

Fig. 3.6 Normalized scattered filed intensity for a MS lens consists of 2 annular sub-MSs of outer radii of 10.7λ and 17.5λ and operating at 4.3μm: (a) in x-z longitudinal plane, (b) along the focal axis (z-axis). Below, field maps at different z-dependent x-y transverse planes: (c) z=27.7λ, (d) z=37λ, (e) z=50λ, (f) z=70λ, (g) z=101.8λ. All intensity plots are normalized to the maximum intensity within the focal range. The MS lens is located at z=0 plane and the four focal distances of the lens are set at $f_x^{\mathrm{c}} = 40.2\lambda$, $f_y^{\mathrm{c}} = 50.5\lambda$, $f_x^{\mathrm{p}} = 71.4\lambda$, and $f_y^{\mathrm{p}} = 78.4\lambda$, respectively.

Moreover, the FWHM of the focus field in the *x*-*y* transverse plane (lateral resolution) is shown in Fig. 3.7 varying the transverse plane location within the focal region. It is observed that the lateral FWHM slightly changes from ~1.37λ to ~2.8λ along the focal range extended from z = 27.7λ to 101.8λ. The absolute efficiency of the MS lens is also ~28% at 4.3μm. In order to determine the absolute efficiency [35], we first calculate the waist of the scattered field in the transverse focal plane. Here the transverse plane located in the middle of the focus range (extending from z = 27.7λ to 101.8λ) is considered as the focal plane, which is $z \approx 65\lambda$ transverse plane. The waist of the scattered field (in the focal plane) is defined as the full width of the normalized intensity at $1/e^2$ and is evaluated by fitting the scattered field intensity distribution at the focal plane to a Gaussian function. The absolute efficiency is then defined as the total power flowing within the waist at the above defined focal plane, divided by the incident power illuminating the MS [35].

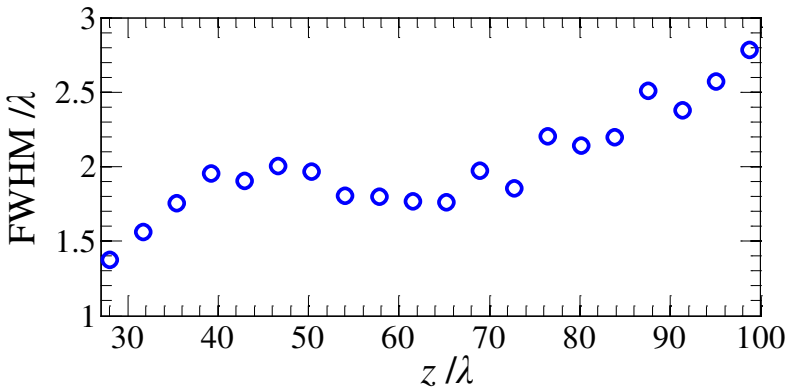

Fig. 3.7 The FWHM (lateral resolution) of the electric field scattered from the MS lens in Fig. 3.6 at different transverse (*x*-*y*) planes within the focal region.

Sec. 3.5 Conclusion

We have shown a novel concept and design for flat metasurface multifocal lenses, which provides multiple foci with arbitrary locations and separations. Instead of forming only a

single spot, the proposed lens can focus the incident beam into multiple closely-spaced/spatially-separated foci. Thanks to the proposed Y-shaped antenna elements that add a degree of freedom compared to the V-shaped elements used in other works, bifocal lenses are implemented based on the polarization-diversity technique in which each polarization contributes to one focal spot. Furthermore, the flat metasurface lens consisting of multiple concentric annular regions, on the other hand provides the possibility of focusing the incident beam into multiple well-separated foci. Subsequently, a flat lens with a single elongated focal region with depth of focus (DOF) of about 74.1λ and lateral FWHM of about 1.7λ is successfully implemented by combination of the polarization-diversity and the annular-segmentation techniques. The implementation of multifocal lenses and monofocal lenses with elongated DOF by thin flat MS would significantly reduce cost, volume, optical loss, and system complexity in integrated optics.

This chapter is reproduced based on the material in [M. Veysi, C. Guclu, O. Boyraz, and F. Capolino, "Reflective metasurface lens with an elongated needle-shaped focus," *Journ. Opt. Soc. Am. B*, Vol. 34, No. 2, pp. 374-382, 2017], © 2017 Optical Society of America.

References

[1] E. R. Dowski and W. T. Cathey, “Extended depth of field through wave-front coding,” *Appl. Opt.*, vol. 34, no. 11, p. 1859, Apr. 1995.

[2] J.-A. Conchello and M. E. Dresser, “Extended depth-of-focus microscopy via constrained deconvolution,” *J. Biomed. Opt.*, vol. 12, no. 6, pp. 064026-064026-7, 2007.

[3] B. Forster, D. Van De Ville, J. Berent, D. Sage, and M. Unser, “Complex wavelets for extended depth-of-field: A new method for the fusion of multichannel microscopy images,” *Microsc. Res. Tech.*, vol. 65, no. 1–2, pp. 33–42, Sep. 2004.

[4] T. Colomb, N. Pavillon, J. Kühn, E. Cuche, C. Depeursinge, and Y. Emery, “Extended depth-of-focus by digital holographic microscopy,” *Opt. Lett.*, vol. 35, no. 11, p. 1840, Jun. 2010.

[5] T. A. Planchon *et al.*, “Rapid three-dimensional isotropic imaging of living cells using Bessel beam plane illumination,” *Nat. Methods*, vol. 8, no. 5, pp. 417–423, May 2011.

[6] F. Aguet, D. V. D. Ville, and M. Unser, “Model-Based 2.5-D Deconvolution for Extended Depth of Field in Brightfield Microscopy,” *IEEE Trans. Image Process.*, vol. 17, no. 7, pp. 1144–1153, Jul. 2008.

[7] J.-A. Conchello and J. W. Lichtman, “Optical sectioning microscopy,” *Nat. Methods*, vol. 2, no. 12, pp. 920–931, Dec. 2005.

[8] A. G. Valdecasas, D. Marshall, J. M. Becerra, and J. J. Terrero, “On the extended depth of focus algorithms for bright field microscopy,” *Micron*, vol. 32, no. 6, pp. 559–569, Aug. 2001.

[9] S. Liu and H. Hua, “Extended depth-of-field microscopic imaging with a variable focus microscope objective,” *Opt. Express*, vol. 19, no. 1, p. 353, Jan. 2011.

[10] B.-Z. Dong, G.-Z. Yang, B.-Y. Gu, and O. K. Ersoy, “Iterative optimization approach for designing an axicon with long focal depth and high transverse resolution,” *J. Opt. Soc. Am. A*, vol. 13, no. 1, p. 97, Jan. 1996.

[11] J.-S. Ye, B.-Z. Dong, B.-Y. Gu, G.-Z. Yang, and S.-T. Liu, “Analysis of a closed-boundary axilens with long focal depth and high transverse resolution based on rigorous electromagnetic theory,” *J. Opt. Soc. Am. A Opt. Image Sci. Vis.*, vol. 19, no. 10, pp. 2030–2035, Oct. 2002.

[12] J. Ojeda-Castaneda and L. R. Berriel-Valdos, “Zone plate for arbitrarily high focal depth,” *Appl. Opt.*, vol. 29, no. 7, p. 994, Mar. 1990.

[13] J. Ojeda-Castaneda, R. Ramos, and A. Noyola-Isgleas, “High focal depth by apodization and digital restoration,” *Appl. Opt.*, vol. 27, no. 12, p. 2583, Jun. 1988.

[14] K. Kitamura, K. Sakai, and S. Noda, “Sub-wavelength focal spot with long depth of focus generated by radially polarized, narrow-width annular beam,” *Opt. Express*, vol. 18, no. 5, pp. 4518–4525, Mar. 2010.

[15] J. Lin, K. Yin, Y. Li, and J. Tan, “Achievement of longitudinally polarized focusing with long focal depth by amplitude modulation,” *Opt. Lett.*, vol. 36, no. 7, p. 1185, Apr. 2011.

[16] H. Dehez, A. April, and M. Piché, “Needles of longitudinally polarized light: guidelines for minimum spot size and tunable axial extent,” *Opt. Express*, vol. 20, no. 14, pp. 14891–14905, Jul. 2012.

[17] M. Veysi, C. Guclu, and F. Capolino, “Vortex beams with strong longitudinally polarized magnetic field and their generation by using metasurfaces,” *J. Opt. Soc. Am. B*, vol. 32, no. 2, p. 345, Feb. 2015.

[18] M. Veysi, C. Guclu, and F. Capolino, “Focused azimuthally polarized vector beam and spatial magnetic resolution below the diffraction limit,” *J. Opt. Soc. Am. B*, vol. 33, no. 11, p. 2265, Nov. 2016.

[19] F. Qin *et al.*, “Shaping a Subwavelength Needle with Ultra-long Focal Length by Focusing Azimuthally Polarized Light,” *Sci. Rep.*, vol. 5, p. 9977, 2015.

[20] E. T. F. Rogers and N. I. Zheludev, "Optical super-oscillations: sub-wavelength light focusing and super-resolution imaging," *J. Opt.*, vol. 15, no. 9, p. 094008, 2013.

[21] G. Yuan, E. T. F. Rogers, T. Roy, G. Adamo, Z. Shen, and N. I. Zheludev, "Planar super-oscillatory lens for sub-diffraction optical needles at violet wavelengths," *Sci. Rep.*, vol. 4, p. 6333, Sep. 2014.

[22] P. M. Blanchard and A. H. Greenaway, "Simultaneous multiplane imaging with a distorted diffraction grating," *Appl. Opt.*, vol. 38, no. 32, p. 6692, Nov. 1999.

[23] P. Prabhat, S. Ram, E. S. Ward, and R. J. Ober, "Simultaneous imaging of different focal planes in fluorescence microscopy for the study of cellular dynamics in three dimensions," *IEEE Trans. NanoBioscience*, vol. 3, no. 4, pp. 237–242, Dec. 2004.

[24] H. Caron, "Dual field-of-view optical imaging system with dual focus lens," US8294808 B2, 23-Oct-2012.

[25] P.-Y. Liu *et al.*, "A novel dual focus objective lens for DVD/CD pick-up head," *IEEE Trans. Magn.*, vol. 34, no. 2, pp. 462–464, 1998.

[26] M. J. Simpson, "Diffractive multifocal intraocular lens image quality," *Appl. Opt.*, vol. 31, no. 19, pp. 3621–3626, Jul. 1992.

[27] W. Daschner, B. Block, A. Thornton, and B. Kress, "Dual focus lens with extended depth of focus," US6330118 B1, 11-Dec-2001.

[28] P. J. Valle and M. P. Cagigal, "Analytic design of multiple-axis, multifocal diffractive lenses," *Opt. Lett.*, vol. 37, no. 6, pp. 1121–1123, Mar. 2012.

[29] M. Veysi, C. Guclu, O. Boyraz, and F. Capolino, "Thin anisotropic metasurfaces for simultaneous light focusing and polarization manipulation," *J. Opt. Soc. Am. B*, vol. 32, no. 2, p. 318, Feb. 2015.

[30] F. Aieta *et al.*, "Aberration-Free Ultrathin Flat Lenses and Axicons at Telecom Wavelengths Based on Plasmonic Metasurfaces," *Nano Lett.*, vol. 12, no. 9, pp. 4932–4936, Sep. 2012.

[31] B. Memarzadeh and H. Mosallaei, "Array of planar plasmonic scatterers functioning as light concentrator," *Opt. Lett.*, vol. 36, no. 13, pp. 2569–2571, Jul. 2011.

[32] M. Farmahini-Farahani and H. Mosallaei, "Birefringent reflectarray metasurface for beam engineering in infrared," *Opt. Lett.*, vol. 38, no. 4, pp. 462–464, Feb. 2013.

[33] X.-Y. Jiang *et al.*, "An ultrathin terahertz lens with axial long focal depth based on metasurfaces," *Opt. Express*, vol. 21, no. 24, pp. 30030–30038, Dec. 2013.

[34] J. Huang and J. A. Encinar, *Reflectarray antennas*. Piscataway, N.J.; Hoboken, N.J.: IEEE Press; Wiley-Interscience, 2008.

[35] M. Khorasaninejad *et al.*, "Achromatic Metasurface Lens at Telecommunication Wavelengths," *Nano Lett.*, vol. 15, no. 8, pp. 5358–5362, Aug. 2015.

CHAPTER 4

THEORY OF FOCUSED AZIMUTHALLY POLARIZED VECTOR BEAMS AND SPATIAL MAGNETIC RESOLUTION BELOW THE DIFFRACTION LIMIT

Sec. 4.1 Motivation

Vector beams [1]–[7] are a class of optical beams whose polarization profiles on the transverse plane, perpendicular to the beam axis, can be engineered to have an inhomogeneous distribution. Among them, beams with cylindrical symmetry (so-called cylindrical vector beams), particularly radially [3], [4], [8]–[10] and azimuthally [11]–[13] electric-polarized vector beams, are exceptionally important in the optics community. Owing to the presence of the longitudinal electric field component, a radially polarized vector beam with ring-shaped field profile after tight focusing through a lens provides a tighter electric field spot compared to the well-known linearly and circularly polarized beams [8], [9]. Such a beam has been extensively examined under tight focusing and has found many prominent applications in particle manipulation, high-resolution microscopy and spectroscopy systems [3], [5], [6], [8], [9], [14]–[24]. In this chapter, we are particularly

interested in studying the azimuthally electric-polarized vector beam primarily due to its unique magnetic field features, a strong longitudinal magnetic field where the electric field is null. In the following, we denominate such a beam simply as *azimuthally polarized beam (APB)* referring to the local orientation of its electric field vector. APBs possess an electric field purely transverse to the beam axis and a strong longitudinal magnetic field component in the vicinity of the beam axis where the transverse electric and magnetic fields are negligible and even vanish on the beam axis (See Fig. 4.1) [12]. This so-called magnetic-dominant region is characterized by the presence of a tight magnetic field with longitudinal polarization. Especially, focusing an APB through a lens boosts its longitudinal magnetic field component relatively more than its transverse electric and magnetic fields [12].

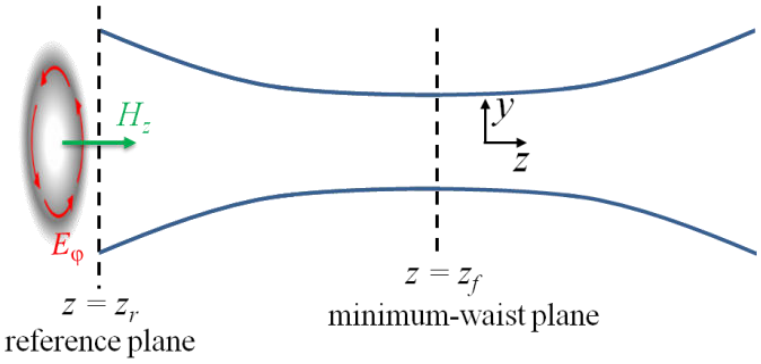

Fig. 4.1 Schematic of a converging azimuthally electric-polarized beam (APB), with a longitudinal magnetic field on its axis.

Due to such unique property, the APB may be beneficial by adding an extra feature to future spectroscopy and scanning probe microscopy systems based on the excitation of magnetic dipolar transitions [11], [12], [25], [26]. At optical range, the magnetic dipolar transitions in matter are several orders of magnitude weaker than their electric counterparts [26]–[28] and therefore require an excitation beam with an enhanced

magnetic-dominant region to be explicitly excited [26]. In this regards, the APBs are an intriguing choice for the illumination beam in such spectroscopy and scanning probe microscopy systems. Even though various methods have been proposed to generate APBs [12], [29]–[38], characterization of the magnetic field of these beams under tight focusing, to the authors' best knowledge, remains to be fully elucidated. Especially, this study is the basis for the successful implementation of magnetically sensitive nanoprobes at optical frequency which are crucial in the development of magnetism-based spectroscopy applications and the study of weak photoinduced magnetism in matter [25], [39], [40].

In this Chapter, we report the diffraction-limited tight field (especially magnetic field) features of an APB, represented in terms of paraxial Laguerre Gaussian (LG) beams, with beam parameter w_0 that is a measure of the spatial extent of the beam in the transverse plane at its minimum waist. The two main figures of merit used in quantifying the field features in this paper are the full width at half maximum (FWHM) of the longitudinal magnetic field intensity and the complementary FWHM (CFWHM) of the annular-shaped total electric field intensity. Keeping in mind that for a very small beam parameter w_0 the expressions obtained via paraxial approximation may not be accurate, we also report results using the accurate analytical-numerical plane-wave spectral (PWS) calculations [41], which is analogous to the Richards and Wolf theory [42].

We first elaborate on the diffraction-limited tight focus of an APB through a converging lens using both paraxial Fresnel diffraction integral formulation, leading to analytical assessments, and the accurate PWS calculations (see [12] for more details on PWS). We demonstrate using the Fresnel integral under *paraxial approximation* that upon focusing

through a lens an incident APB converts to another APB whose beam parameter is linearly proportional to the lens paraxial focal distance and inversely proportional to the incident APB parameter (see Appendix A at the end of this chapter). The minimum-waist plane position of the focused beam predicted by the Fresnel integral coincides with the lens paraxial focal plane, which deviates from the actual focal plane position calculated by PWS. The figures of merit of an APB focused by a lens are therefore calculated both by the Fresnel integral at the lens's paraxial focus and by the PWS at the actual focal plane as a function of the lens paraxial focal distance.

In addition to the case of focusing an APB by a lens mentioned above, the tight field features of a self-standing converging APB are also examined and its figures of merit are calculated using the paraxial LG beam expressions and the PWS calculations at the minimum-waist planes predicted by the respective methods. Recently it has been experimentally confirmed that cylindrical vector beams may selectively excite the electric or magnetic dipolar resonances of a subwavelength-sized dense dielectric nanosphere (e.g., a silicon nanosphere) [24]. In this paper, we use a silicon nanosphere as a magnetic nanoantenna (so-called magnetic nanoprobe) and place it at the focus of a converging APB, which selectively excites a magnetic dipolar resonance in the nanosphere as in [24]. The aim is to achieve a subwavelength magnetic field resolution. In general, such a subwavelength-sized scatterer hosts a magnetic Mie resonance with a circulating electric displacement current in addition to an electric dipolar resonance. However the latter is not excited by an APB due to its cylindrical symmetry, which ideally leads to a null average displacement current over the nanosphere. The induced electric displacement currents with a net magnetic dipole moment in the Si nanosphere along the z direction are shown to

boost not only the total longitudinal magnetic field but also the spatial magnetic field resolution below the diffraction limit in the vicinity of the scatterer. A total magnetic field enhancement of about 2.3 (with respect to the total incident magnetic field) and a total magnetic field spot area as small as $0.04\lambda^2$ are achieved within a magnetic-dominant region, evaluated at a transverse plane one nanosphere radius (0.12λ) away from the scatter surface.

Note that the FWHM is an effective feature to characterize the magnetic near-field intensity, and is also here used as a shorthand measure of resolution, i.e. the minimum resolvable distance between two closely-spaced point sources. The FWHM, here, is used as a measure of resolution since the side-lobe peak of the magnetic near-field intensity profile is for all cases by far less than half of its main peak. Throughout this chapter we consider time harmonic fields with an $\exp(i\omega t)$ time dependence, which is suppressed for convenience. Furthermore bold symbols denote vectors and hats (^) indicate unit vectors.

Sec. 4.2 Characterization of an APB

APB is here expressed as a superposition of a left and a right hand circularly polarized beam, carrying orbital angular momentum (OAM) with orders of +1 and -1, respectively. In paraxial regimes, OAM-carrying beams are analytically represented as LG beams [1]. Thus the APB's electric field is expressed in terms of self-standing paraxial LG beams in cylindrical coordinate system as [12]

$$\mathbf{E} = \frac{-i\sqrt{2}}{2}\left(u_{-1,0}\,\hat{\mathbf{e}}_{\mathrm{RH}} - u_{1,0}\,\hat{\mathbf{e}}_{\mathrm{LH}}\right)e^{ikz} \tag{4.1}$$

where $\hat{\mathbf{e}}_{\mathrm{RH}} = \left(\hat{\mathbf{x}} + i\,\hat{\mathbf{y}}\right)/\sqrt{2}$ and $\hat{\mathbf{e}}_{\mathrm{LH}} = \left(\hat{\mathbf{x}} - i\,\hat{\mathbf{y}}\right)/\sqrt{2}$ are, respectively, right and left hand circularly polarized unit vectors and the LG beam expression is

$$u_{\pm 1, p=0} = \frac{V}{\sqrt{\pi}} \frac{2\rho}{w^2}\, e^{-(\rho/w)^2 \zeta}\; e^{-2i \tan^{-1}(z/z_R)} e^{\pm i\varphi}$$
$$w = w_0 \sqrt{1 + \left(z/z_R\right)^2}\,, \qquad \zeta = \left(1 - i\, z/z_R\right) \tag{4.2}$$

where V is an amplitude coefficient, $z_R = \pi w_0^2 / \lambda$ is the Rayleigh range, and $k = 2\pi / \lambda$ and λ are the wavenumber and wavelength in the host medium, respectively. The beam parameter w_0 controls the transverse spatial extent of the beam at its minimum-waist plane. Vaguely speaking w_0 corresponds to the minimum waist which is very well defined for the fundamental Gaussian beam (FGB), but since the actual waist of the APB differs from w_0 we prefer to call it simply as "beam parameter" because this difference is of relevance in this paper. Here the term "beam waist" is reserved for the minimum of the actual waist size as discussed next. The electric field in Eq. (4.1) is equivalently expressed as [12]

$$\mathbf{E} = E_\varphi\, \hat{\boldsymbol{\varphi}} = \frac{V}{\sqrt{\pi}} \frac{2\rho}{w^2}\, e^{-(\rho/w)^2 \zeta}\; e^{-2i \tan^{-1}(z/z_R)} e^{ikz}\, \hat{\boldsymbol{\varphi}}, \tag{4.3}$$

that clearly shows the purely azimuthal polarization of the beam. The electric field intensity profile of an APB is plotted at the beam's minimum-waist plane (i.e., $z = \mathrm{O}$) in Fig. 4.2(a). It is observed that the APB's electric field has an annular-shaped intensity profile whose CFWHM is of interest to us as a measure of the beam's tightness. The APB examined in Fig. 4.2 is carrying a power of 1mW, obtained by setting $V = 0.89\,\mathrm{V}$ in Eq.

(4.3), and its beam parameter is set to $w_0 = 0.9\lambda$. In Appendix B and section IV of this paper, we show that the converging APB expressed by Eq. (4.1) with such an illustrative beam parameter ($w_0 = 0.9\lambda$) represents, by a good approximation, a self-standing beam. The strength of the APB's electric field given in Eq. (4.3) is proportional to $\rho \exp\left(-\rho^2 / w^2\right)$ in any given *z* transverse plane, and it reaches its maximum

$$\left|E_\varphi(\rho_M, z)\right| = \frac{|V|}{\sqrt{\pi}} \frac{2\rho_M}{w^2} e^{-\left(\rho_M / w\right)^2} = \frac{\sqrt{2}}{\sqrt{\pi e}} \frac{|V|}{w} \tag{4.4}$$

at $\rho_M = w/\sqrt{2}$. Therefore on the minimum-waist plane (i.e., $z = \mathbf{O}$) the electric field magnitude peaks at $\rho_M = w_0/\sqrt{2}$, that is in an agreement with what is shown in Fig. 4.2(a). The magnetic field of the APB with the electric field given in Eq. (4.3) is subsequently found by using $i\omega\mu\mathbf{H} = \nabla \times \mathbf{E}$ in cylindrical coordinates, yielding a longitudinal magnetic field component as [12]

$$H_z = \frac{-V}{\sqrt{\pi}} \frac{4i}{w^2 \omega\mu} \left[1 - \left(\frac{\rho}{w}\right)^2 \zeta\right] e^{-\left(\frac{\rho}{w}\right)^2 \zeta} e^{-2i \tan^{-1}\left(\frac{z}{z_R}\right)} e^{ikz} \tag{4.5}$$

alongside a radial magnetic field component as

$$H_\rho = -\frac{1}{\eta} E_\varphi \left[1 + \frac{1}{kz_R} \frac{\rho^2 - 2w_0^2}{w^2}\right] \tag{4.6}$$

It is observed from Eq. (4.6) that for $kz_R >> 1$ the radial magnetic field component follows the electric field profile of the beam. In summary, the APB possesses only $E_\varphi, H_z,$ and H_ρ field components. The intensity of the APB's longitudinal magnetic field [given in Eq. (4.5)]

is plotted in Fig. 4.2(b) where it peaks on the beam axis ($\rho = 0$) and is characterized by its FWHM. The maximum of the longitudinal magnetic field strength at any *z* is given by

$$\left|H_z(\rho = 0, z)\right| = 4|V| / \left(w^2 \omega \mu \sqrt{\pi}\right) \tag{4.7}$$

and is thus inversely proportional to w^2. It is observed from Eq. (4.7) that the longitudinal magnetic field of the APB peaks at the beam's minimum-waist plane (i.e., $z = 0$ where $w = w_0$), where its magnitude is inversely proportional to the square of the beam parameter w_0^2. The transverse magnetic field [which is purely radial and given in Eq. (4.6)] increases together with the electric field (which is purely azimuthal) as the radial distance ρ from the beam axis increases and peaks away from the beam axis alongside the azimuthal electric field, as shown in Fig. 4.2(c).

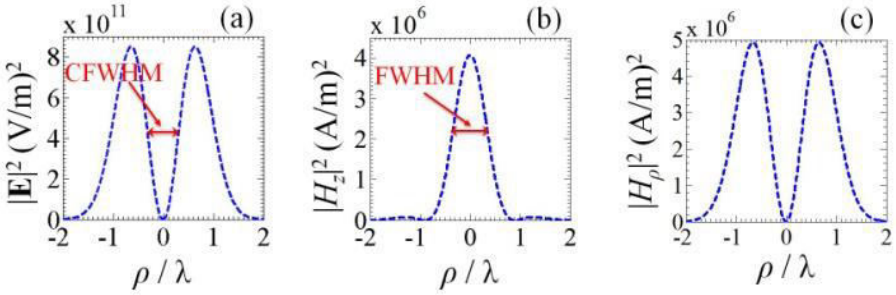

Fig. 4.2 Intensity profile of (a) electric field, (b) axis-confined longitudinal magnetic field, and (c) purely radial transverse magnetic field for an APB carrying 1mW power and with beam parameter of $w_0 = 0.9\lambda$ at λ=523nm.

By duality, this is analogous to the case of the radially polarized beam in which electric field intensity is purely longitudinal on the beam axis and its transverse component peaks off the beam axis [3], [4], [6], [11]. Here, we define the CFWHM for the annular-shaped electric field intensity profile of the APB as the width across its null where the field

intensity rises to the half of its maximum, i.e., to $0.5\left|E_{\varphi}(\rho_M, z)\right|^2$ [see Eq. (4.4) and Fig. 4.2(a)]. In addition, the FWHM of the longitudinal magnetic field intensity is also calculated as the width across its peak on the beam axis where the longitudinal magnetic field intensity drops to the half of its maximum, i.e., to $0.5\left|H_z(\rho=0, z)\right|^2$ [see Fig. 4.2(b)]. Based on the azimuthally polarized electric field and the longitudinally polarized magnetic field expressions given, respectively, in Eq. (4.3) and Eq. (4.5), the CFWHM of the electric field intensity and the FWHM of the longitudinal magnetic field intensity at the minimum-waist plane are calculated and given by

$$\begin{aligned} \mathrm{CFWHM}\left(E_{\varphi}\right)\Big|_{z=0} &\approx 0.68 w_0, \\ \mathrm{FWHM}\left(H_z\right)\Big|_{z=0} &\approx 0.81 w_0. \end{aligned} \tag{4.8}$$

One may be also interested in the ratio of the longitudinal magnetic field on the beam axis, where it is maximum, to the maximum of the electric field at $\rho = \rho_M$. This ratio, normalized with respect to the inverse of the host-medium wave impedance $\eta^{-1} = \sqrt{\varepsilon / \mu}$, is equal to

$$\eta \frac{\left|H_z(\rho=0, z)\right|}{\left|E_{\varphi}(\rho_M, z)\right|} = \frac{\sqrt{2}}{\pi} \frac{\lambda}{w} e^{1/2} \approx 0.74 \frac{\lambda}{w} \tag{4.9}$$

Note that such ratio is inversely proportional to w and it reaches its maximum at $z = 0$, i.e., in the minimum-waist plane. Therefore the maximum magnitude of the longitudinal magnetic field increases relatively more than the maximum magnitude of the electric field as w_0 decreases (tighter beams). Note that decreasing w_0 also has the effect of decreasing the area of the longitudinal magnetic field spot.

Finally, we should note that on the minimum-waist plane ($z=0$) the ratio $\eta\left|H_z(\rho,0)\right|/\left|E_\varphi(\rho,0)\right|$ is equal to unity at the radial distance

$$\rho = w_0\left(\sqrt{1+\left(\frac{\pi w_0}{2\lambda}\right)^2}-\frac{\pi w_0}{2\lambda}\right) \tag{4.10}$$

and inside this radius, the longitudinal magnetic to total electric field contrast ratio for APB is larger than the magnetic to electric field contrast ratio (the admittance) of a plane wave $1/\eta$. The optical power carried by the APB is calculated by the integral of its longitudinal Poynting vector over its minimum-waist plane as

$$P=\frac{1}{2}\int_0^{2\pi}\int_0^{\infty}\mathrm{Re}\left\{-E_\varphi\left(H_\rho\right)^*\right\}_{z=0}\rho d\rho d\varphi \tag{4.11}$$

After substituting the APB's azimuthal electric and radial magnetic fields formulas given in Eq. (4.3) and Eq. (4.5) into Eq. (4.11), the power carried by the APB is evaluated as

$$P=\frac{|V|^2}{2\eta}\left(1-\frac{1}{\left(\pi w_0/\lambda\right)^2}+\frac{\displaystyle\int_0^{2\pi}\int_0^{\infty}\left(\frac{|E_\varphi|}{w_0|V|}\right)^2\rho^3 d\rho d\varphi}{2\left(\pi w_0/\lambda\right)^2}\right) \tag{4.12}$$

After a change of variable from $2\left(\rho/w_0\right)^2$ to t, the integral term in Eq. (4.12) is found to be equal to $0.5\Gamma(3)=1$ where $\Gamma(\cdot)$ is the gamma function. Therefore Eq. (4.12) is reduced to

$$P = \frac{|V|^2}{2\eta}\left(1 - \frac{1}{2(\pi w_0/\lambda)^2}\right) \tag{4.13}$$

Eq. (4. 13) clearly shows that power carried by the APB is explicitly expressed as a function of w_0/λ and the absolute value of the amplitude coefficient $|V|$. Therefore, the APB's amplitude coefficient *V* is obtained for certain beam parameter w_0 and required power using Eq. (4.13).

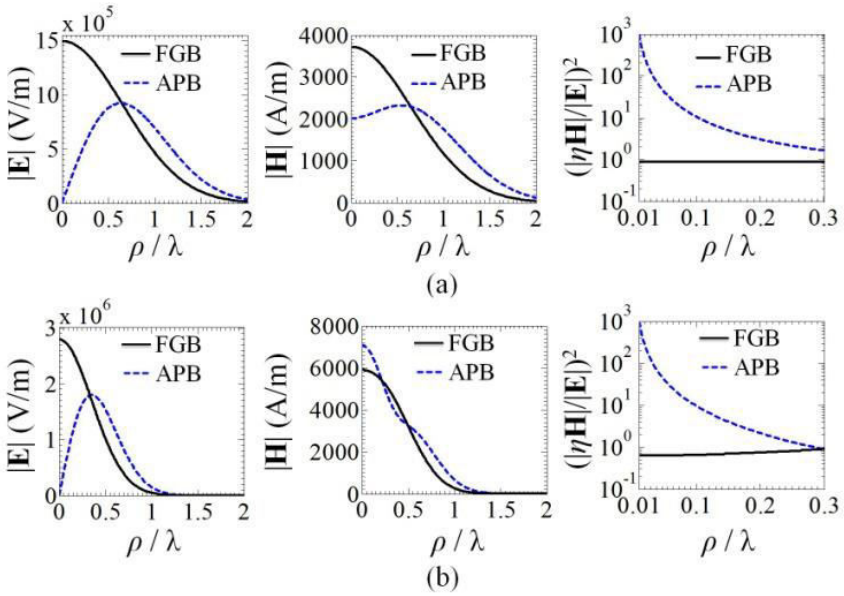

Fig. 4.3 Comparison between a FGB and an APB of equal powers (1mW) at and beam parameters at λ=523nm their minimum-waist planes (i.e., *z*=0): (top row) $w_0 = 0.9\lambda$ and (bottom row) $w_0 = 0.5\lambda$. Strength of the total electric field (first column), strength of the total magnetic field (second column), and the ratio of the total magnetic to the total electric field intensities normalized to that of a plane wave (third column) (Note how this ratio grows for the APB when approaching the beam axis.).

In order to have a better assessment of the APB's significance in providing a magnetic-dominant region, here we compare an APB with a FGB of equal powers and beam parameters. The electric and magnetic field distributions of a paraxial APB and a FGB at their paraxial minimum-waist planes, i.e. at *z* = 0, are compared in Fig. 4.3 for two

illustrative beam parameters set to (top row) $w_0 = 0.9\lambda$ and (bottom row) $w_0 = 0.5\lambda$. Here the APB and the FGB carry equal powers of 1mW [See Eq. (4.13)]. In order to have azimuthally symmetric magnetic field distribution for the FGB, we consider circularly polarized FGB in Fig. 4.3, however similar conclusions would be obtained if we used linearly polarized FGB. In contrast to the FGB whose magnetic and electric fields peak on the beam axis (i.e., the *z* axis), the APB contains a pure *longitudinal magnetic field component* on the beam axis where its electric field vanishes. The magnetic-to-electric field intensity ratio normalized to that of a plane wave is also plotted for the APB and the FGB in Fig. 4.3 (third column) varying radial distance from the beam axis. Note that the magnetic-to-electric field intensity ratio of the FGB is very close to that of a plane wave. In contrast the APB has a very large magnetic-to-electric field intensity ratio in the vicinity of the beam axis denoting the magnetic-dominant region. This ratio for the APB tends to infinity when $\rho \to 0$. For $w_0 = 0.9\lambda$ [Fig. 4.3(top row)], even though the strength of the APB's magnetic field on the beam axis is half of that of the FGB carrying the same power, the APB uniquely has only magnetic field and no electric field there, which is an important feature that can be used in various applications. In addition, it is observed from Fig. 4.3(top row) that the FWHM of the total magnetic field for the APB with $w_0 = 0.9\lambda$ is larger than that for the FGB with the same w_0, this is attributed to the fact that the APB contains an annular-shaped radial magnetic field component [see Fig. 4.2(c)]. However, decreasing the beam parameter (tightening the beam) from $w_0 = 0.9\lambda$ to $w_0 = 0.5\lambda$ boosts longitudinal magnetic field component relatively more than the radial one, and therefore significantly decreases the FWHM of the total magnetic field, as shown in Fig. 4.3(bottom row). To

further reduce the FWHM of the total magnetic field of the APB approaching to that of its longitudinal magnetic field component, one approach might be to use ring-shaped lenses with high numerical apertures for focusing of the APB. This technique has been used for generating very sharp electric field focuses using radially polarized beams [8], [9].

Sec. 4.3 Focusing an APB through a lens

Let us now assume that an APB illuminates a converging lens. In Appendix A, using the Fresnel integral [Eq. (4. A3)] we show how a lens, under paraxial approximation, converts an incident APB, whose minimum-waist plane occurs at the lens surface, to another *converging* self-standing APB whose paraxial minimum-waist plane coincides with the lens's paraxial focal plane. This is schematically represented in Fig. 4.4 for a specific example where we show the total electric and the longitudinal magnetic field magnitudes of the APB before and after focusing through the lens.

In this section, we aim to characterize magnetic and electric fields of an APB upon focusing through a lens at the focal plane of the lens. To have an analytical assessment, we first calculate the fields at the lens's paraxial focal plane using the paraxial Fresnel integral (See Appendix A for more details) as a function of the lens paraxial focal distance using Eq. (4.1) and Eq. (4.A10). Next in order to confirm the analytical calculations and to provide a guide to where the Fresnel integral expressions valid, we characterize the APB upon focusing through a converging lens using the accurate PWS calculations. As for the PWS calculations, we assume the thin lens approximation such that each *ray* entering one side of the lens exits the other side at the same transverse (ρ, φ) coordinates as the entrance

position. We model the transmission through the lens by imposing a phase shift, which varies in radial direction, added to the ρ-dependent phase of the incident APB.

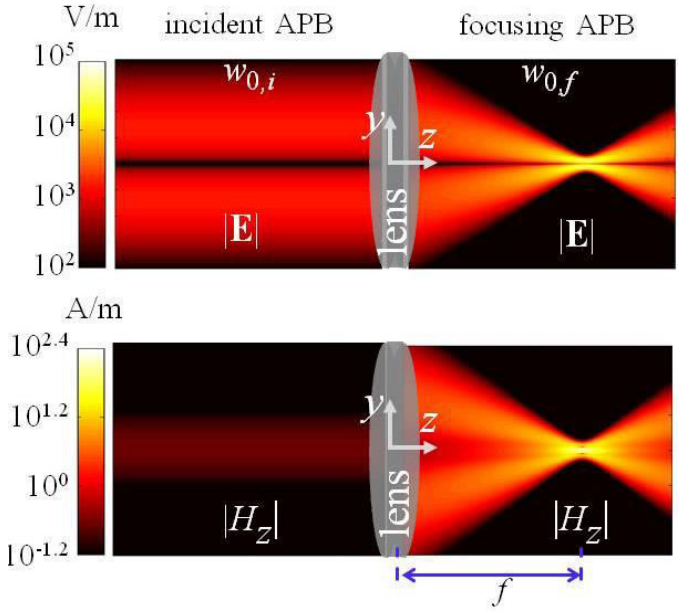

Fig. 4.4 Schematic of a converging lens transforming an incident APB with beam parameter $w_{0,i}$ into another converging APB with beam parameter $w_{0,f}$. The magnitudes of the total electric (which is purely azimuthal) and the longitudinal magnetic fields are plotted. The radial component of the magnetic field, also experiencing focusing, is not shown here for brevity. In this representative example, the incident APB carries 1mW power, and the lens radius and focal distance are set at a=40λ and f=80λ, respectively. The beam parameters of the incident and focusing APBs are $w_{0,i} = 29\lambda$ and $w_{0,f} = 1.3\lambda$, respectively.

The transmission phase shift that is added, relative to a spherically converging wave, is given by

$$\Phi(\rho) = -\frac{2\pi f}{\lambda}\left(\sqrt{1+\frac{\rho^2}{f^2}}-1\right) \tag{4.14}$$

where f is the paraxial focal distance of the lens (on the right panel of Fig. 4.4), ρ is the local radial coordinate of the lens, and λ is the wavelength in the host medium on the right

side of the lens. Note that we are assuming that the lens does not vary the ρ-dependent amplitude of the incident APB's field across the lens. We also remind that in the Fresnel integral equation the phase term in Eq. (4.14) is paraxially approximated as a quadratic phase [see Eq.(4.A2)] term [43]. The Fourier and inverse Fourier transform integrals in PWS calculations (see Eq. (24)-(25) in [12]) are then numerically calculated via a two-dimensional FFT algorithm where the size of the entire spatial domain and spatial resolution are $2048\lambda \times 2048\lambda$ and $\lambda/20$, respectively. Moreover, to model the hard-edged aperture, the electric field is assumed null outside of the overall lens aperture in the lens plane.

We now characterize the FWHM of $|H_z|^2$ and the CFWHM of $|\mathbf{E}|^2$ at the lens focal plane for an incident APB. As a representative example, we set the lens radius *a* equal to 40λ and characterize the focusing beam at the lens's focal plane as the lens's paraxial focal distance *f* changes. The *incident* APB has a beam parameter of $w_{0,i} = 29\lambda$ such that the beam cross-section is much wider than the wavelength and 90% of the incident beam power illuminates the lens surface. In Fig. 4.5 we plot the FWHM of $|H_z|^2$ and CFWHM of $|\mathbf{E}|^2$ calculated at the lens's focal plane as a function of the lens radius to focal distance ratio *a/f*, where *a* is kept constant and *f* is varied. We recall that the right side of Fig. 4.4 corresponds to the field maps for a specific case with *a*=*f*/2, which is a point on the curves reported in Fig. 4.5. The quantities plotted in Fig. 4.5 are calculated using both the Fresnel integral formula [given in Eq. (4.A10)] at the lens's paraxial focal plane (*z*=*f*) and PWS calculations (refer to [12] for more details on PWS) at the lens's actual focal plane.

It is observed from Fig. 4.5 that the paraxial Fresnel integral results (denoted by FI) agree very well with the accurate PWS results especially for large focal distances (small *a/f*). We also observe from the PWS results that for the case with *f*=*a*, the FWHM of the longitudinal magnetic field intensity and CFWHM of the total electric field intensity at the lens actual focal plane are 0.715λ and 0.53 λ, respectively. Note that the actual focal plane, obtained from PWS calculations, is slightly displaced from the lens's paraxial focal plane as described in the next section. In Appendix B, we elaborate more on this as we examine the plane wave spectrum of converging beams.

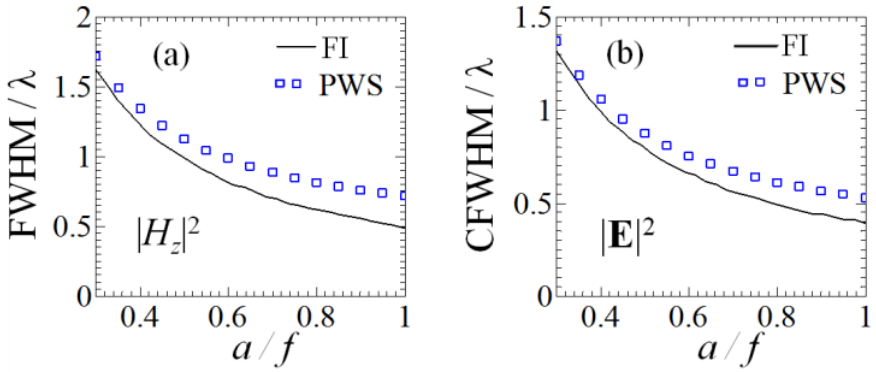

Fig. 4.5 (a) FWHM of the longitudinal magnetic field intensity $|H_z|^2$, and (b) CFWHM of the annular-shaped electric field intensity $|\mathbf{E}|^2$ calculated using (i) PWS at the actual focal plane and (ii) Fresnel integral (FI) at the lens's paraxial focal plane, upon illuminating the lens by an incident APB, varying normalized lens's focal distance *f*.

Sec. 4.4 Self-standing converging APB

As we discussed in the previous section, a lens converts an incident APB to another *converging* self-standing APB whose constituent evanescent components in its spectrum are negligible (see Fig. 4.4 and Appendix A). This simplifies the calculations of the focusing beam due to a lens assuming the paraxial approximation (See Appendix A). Therefore, in

this section we examine propagation of a self-standing converging APB, assuming it is focused by the lens, and quantify its properties at its minimum-waist plane. We show some important tight field features of self-standing converging APBs as a function of their beam parameter $w_{0,f}$ (as shown in Fig. 4.4) where we pay particular attention to the FWHM of their longitudinal magnetic fields at the minimum waist. Since we only elaborate on a self-standing converging beam we drop the subscript *f* and denote the converging beam parameter simply as w_0. The spectral components of the converging APBs are examined in Appendix B where we show that more than 95% of the spectral energy of the converging APBs with $w_0 \geq 0.5\lambda$ is confined in the propagating spectrum. Thus, in the subsequent studies the beam parameter of the converging APB is set larger or equal to 0.5λ. The results pertaining to the paraxial beam propagation are also compared to those obtained from the analytical-numerical computation based on the PWS. We assume to know the initial APB's field distribution, with converging features, at a certain *z*-plane (so-called reference plane) and observe the beam propagating toward its minimum-waist plane in +*z* direction. In other words, we investigate the converging properties of the beam on the right side of the lens in Fig. 4.4.

We first assess the validity of the paraxial approximation for APBs as in Eq. (4.1). It is known that the paraxial approximation for a beam holds under the following condition [2], [44], [45]

$$\left|2k\frac{\partial \boldsymbol{\psi}}{\partial z}\right| >> \left|\frac{\partial^2 \boldsymbol{\psi}}{\partial z^2}\right| \tag{4.15}$$

where $\mathbf{E} = \boldsymbol{\psi} e^{ikz}$ represents paraxial field distribution for a beam propagating in +z direction. In order to determine the validity range of the paraxial field, we define a *paraxiality* figure as

$$F_{\mathrm{p}} = \left| 2k \frac{\partial \boldsymbol{\psi}}{\partial z} \right| \Bigg/ \left| \frac{\partial^2 \boldsymbol{\psi}}{\partial z^2} \right| \tag{4.16}$$

which is a function of local coordinate. We also define the *normalized weighted average figure* of the paraxiality at each transverse z-plane as

$$F_{\mathrm{p,ave}} = \int_{-\infty}^{\infty} \int_{-\infty}^{\infty} F_{\mathrm{p}} |\boldsymbol{\psi}|^2 \, dx \, dy \Bigg/ \int_{-\infty}^{\infty} \int_{-\infty}^{\infty} |\boldsymbol{\psi}|^2 \, dx \, dy \tag{4.17}$$

where the numerator is the average paraxiality figure weighted by the intensity of the transverse field and the denominator is the total weight of the transverse field intensity with respect to which we normalize the weighted average paraxiality figure. The value of $F_{\mathrm{p,ave}}$ for the paraxial APB's electric field in Eq. (4.1) is calculated and plotted in Fig. 4.6 as a function of the beam parameter w_0, at the beam's paraxial minimum-waist plane z=0. The larger the paraxiality figure $F_{\mathrm{p,ave}}$ is, the better the paraxial approximation is. It is observed from Fig. 4.6 that $F_{\mathrm{p,ave}} \geq 50$ (i.e., $\log_{10}(F_{\mathrm{p,ave}}) \geq 1.7$) for the beam parameters larger than 0.9λ. We assume that $F_{\mathrm{p,ave}}$ values larger than 50 represent reasonably valid paraxial beams for practical purposes. Thus, for such values of w_0 the paraxial electric field expression given in Eq. (4.1) represents a self-standing APB's field distribution with a good approximation. Remarkably, the signature of this "validity range" manifests itself in the

comparison of the paraxial beam propagation and the accurate PWS results discussed in the following.

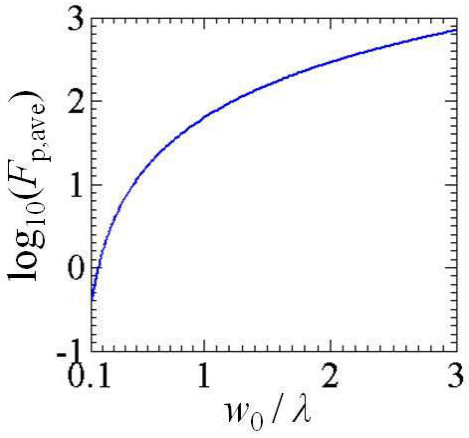

Fig. 4.6 The normalized weighted average figure of paraxiality $F_{\mathrm{p,ave}}$ (in logarithmic scale) for a converging APB at the beam's paraxial minimum-waist plane (z=0) as a function of the beam parameter w_0.

We now examine the magnetic and electric field features of a self-standing converging APB at its minimum-waist plane as a function of the beam parameter w_0 (for $w_0 \geq 0.5\lambda$). With this in mind, we characterize self-standing converging APB using PWS calculations. We start with an APB's paraxial transverse field distribution on a transverse reference plane located at $z = z_r$ ($z_r < z_f$, see Fig. 4.1 for z_f) given by Eq. (4.1). Subsequently the evolutions of the beam's magnetic and electric fields in the positive z-direction are examined using the PWS calculations. The location of the actual minimum-waist plane of a converging APB "launched" from a reference plane at $z_r = -3.5\lambda$ with the field distribution given in Eq. (4.1) is calculated using PWS and plotted in Fig. 4.7 as a function of the beam parameter w_0. We observe that the actual minimum-waist plane of the converging APB does not occur at z=0, that is the location of the focus predicted by the

paraxial field expression. This difference is attributed to the presence of plane-wave constituents with large transverse wave numbers in the field spectrum of the converging APB which are not properly modeled in the paraxial field expressions (See Appendix B for more details on spectral content of the APB). For an APB, with decreasing w_0 a larger amount of constitutive propagating plane wave spectral components of the beam's field will have large transverse wavenumbers.

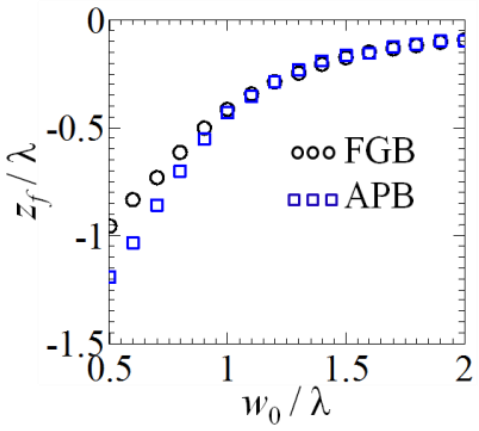

Fig. 4.7 The position of the actual minimum-waist plane of the beam z_f as a function of the beam parameter w_0 for both APB and FGB (calculated using the PWS). The minimum-waist plane estimated by using the simple paraxial field expression is at z=0.

Hence, the difference between the actual minimum-waist plane's location (here denoted by z_f) and the one predicated by the paraxial field expressions (here at z = 0) becomes more significant, because of the loss of accuracy of the paraxial approximation with decreasing w_0. As a reference, in Fig. 4.7 we also plot the minimum-waist plane's position of a converging FGB as a function of its w_0. We observe that the difference between the actual and the paraxial minimum-waist plane's positions for a FGB is also increasing as w_0 decreases. However, the difference between the actual minimum-waist plane's position and

the paraxial one is larger for an APB than for a FGB with an equal w_0. This is due to the fact that the transverse wavenumber spectrum of an APB's field is broader than that of a FGB's field with the same beam parameter; hence the paraxial approximation is coarser for the APB compared to the FGB.

Next the FWHM of $|H_z|^2$ and the CFWHM of $|\mathbf{E}|^2$ of the converging APB are calculated using both paraxial and PWS calculations and plotted in Fig. 4.8. The FWHM and the CFWHM in the PWS calculations are evaluated at the actual minimum-waist plane of the APB ($z = z_f$), that depends on w_0 (see Fig. 4.7). Instead, the FWHM and CFWHM under the paraxial approximation are evaluated using Eq. (4.1) at z = 0 for all the w_0 cases. It is observed from the paraxial calculations that the FWHM and CFWHM curves decrease monotonically as the beam parameter w_0 decreases. However, in practice, the decrease in FWHM of the longitudinal magnetic field intensity profile as well as CFWHM of the electric field intensity profile is hampered by an ultimate limit imposed by the diffraction of the beam. It is observed from the PWS curves in Fig. 4.8 that the FWHM and CFWHM of the converging APB are saturated by the diffraction to about 0.56λ and 0.43λ, respectively, despite the paraxial approximation estimates much smaller FWHM and CFWHM. Thus, according to accurate PWS calculations, longitudinal magnetic field intensity profile with FWHM as small as 0.56λ (spot area of about $0.25\lambda^2$) is achievable with $w_0 = 0.5\lambda$. The spot area is defined here as the circular area whose diameter is equal to the FWHM.

Here, based on what discussed in Appendix B, we stress that the transverse wavenumber spectrum of the APB's field in Eq. (4.1) with very small w_0 ($w_0 < 0.5\lambda$) is not

confined only in the propagating wavenumber spectrum and it starts to extend to the evanescent spectral region and therefore is not shown in Fig. 4.8. However, the spatial field distribution in Eq. (4.1) with w_0 as small as 0.5λ has wavenumber spectral constituents still confined in the propagating spectrum (see Appendix B) and it has a relatively large normalized weighted average figure of paraxiality $F_{\text{p,ave}} \approx 14$. Therefore, though it may not represent a strictly self-standing APB, the paraxial approximation is not too coarse.

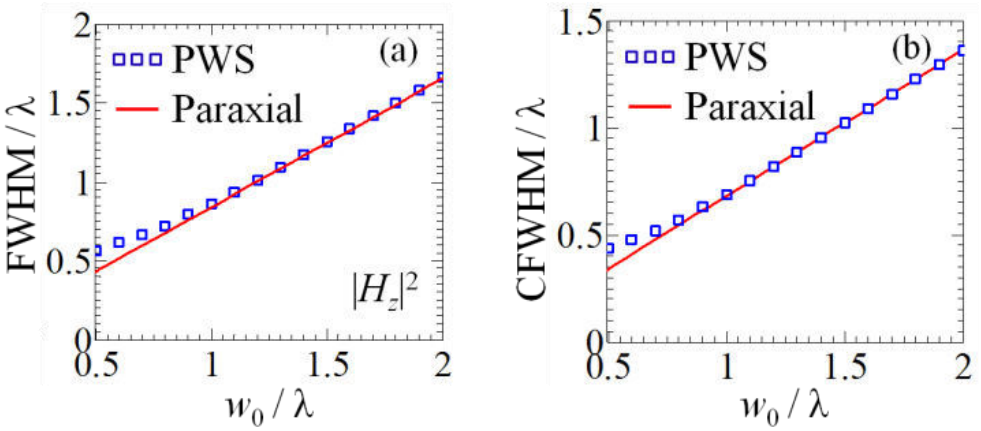

Fig. 4.8 Plane-wave spectral (PWS) and paraxial calculations for (a) the FWHM of the longitudinal magnetic field intensity and (b) the CFWHM of the annular-shaped electric field intensity of the converging APB as a function of the beam parameter w_0.

When the beam parameter w_0 is larger than 0.9λ, the paraxial curves for the FWHM and the CFWHM in Fig. 4.8 follow very well the accurate PWS ones, and they start to deviate from PWS curves when w_0 decreases to smaller values, which is in agreement with our finding in Fig. 4.6. In order to clarify the effect of beam parameter w_0 on different magnetic field components of the APB, in Fig. 4.9 we plot the strength of the longitudinal (H_z) and the radial (H_ρ) magnetic field components as well as the strength of the azimuthal electric field normalized to the host-medium wave impedance for two illustrative w_0 values at

$\lambda = 523\,\text{nm}$, using PWS calculations. We recall that the APB has a H_z profile that peaks on the beam axis ($\rho = 0$), whereas its transverse magnetic field component is purely radial and peaks off the beam axis. It is observed from Fig. 4.9 that the longitudinal magnetic field spot areas as small as $0.25\lambda^2$ and $0.49\lambda^2$ are obtained with converging APBs with w_0 of 0.5λ and 0.9λ, respectively. However, since APB possesses a radial magnetic field component over an annular-shaped region in addition to the longitudinal one (see Fig. 4.9), the FWHM of the total magnetic field is always larger than the FWHM of the longitudinal magnetic field component.

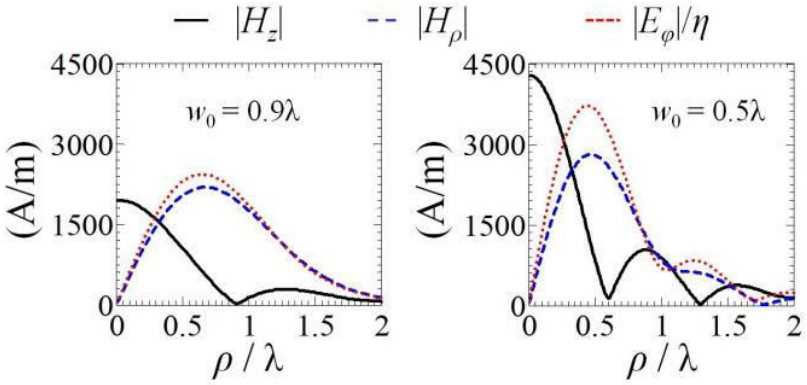

Fig. 4.9 Strength of the longitudinal (H_z) and radial (H_ρ) magnetic fields of an APB for two different beam parameters w_0 at $\lambda = 523\,\text{nm}$, evaluated using accurate PWS calculations. The strength of the azimuthal electric field (E_φ) normalized to the wave impedance is also plotted for comparison.

It is also observed from Fig. 4.9 that when w_0 of the APB decreases from 0.9λ to 0.5λ, the strength of its longitudinal magnetic field component increases by about 2.2 times, which is relatively more than the increase in the strength of its radial magnetic field component (1.24 times). Indeed, as the beam parameter w_0 decreases, the plane-wave spectral distribution of the APB includes large transverse wavenumbers. For smaller beam parameters such like $w_0 = 0.5\lambda$, a larger portion of the constitutive TE (transverse electric

with respect to z) plane waves in the spectrum of the APB possess large transverse wavenumbers meaning that they propagate in directions with larger angles α with respect to the beam axis, as shown in Fig. 4.10. Therefore the magnetic fields of the TE constitutive plane waves, which are perpendicular to the plane wave propagation directions, are more aligned with the beam axis. The depth of focus (DOF, or longitudinal FWHM) of the longitudinal magnetic field intensity profile for a converging APB is also shown in Fig. 4.11 as a function of w_0, using accurate PWS calculations. For the sake of comparison, in Fig. 4.11 we also plot the DOF of the electric field intensity profile for a converging circularly polarized FGB. As w_0 increases, the Rayleigh range z_R increases as $(w_0)^2$ and as a result the beam waist w varies less with respect to z (see Eq. (4.2) where w is written as a function of z and z_R). Therefore the DOF is much longer for larger w_0 which also means the field features are less tight.

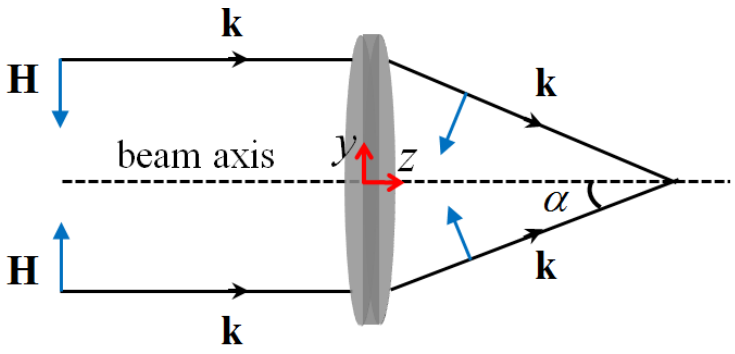

Fig. 4.10 Raytracing model of an APB focusing through a lens. Magnetic field vectors are denoted by blue arrows. Spectral components with large transverse wavenumber provide strong longitudinal magnetic field.

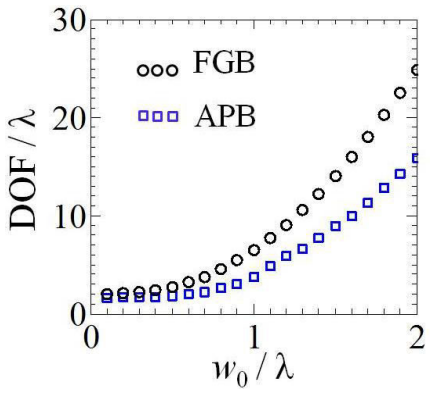

Fig. 4.11 The depth of focus (DOF) of the longitudinal magnetic field intensity profile for a converging APB as a function of the beam parameter w_0, evaluated using PWS. For comparison, the depth of focus of the electric field intensity profile of a FGB is also plotted.

Sec. 4.5 Spatial magnetic resolution below the diffraction limit

So far, we have demonstrated that fields in focal plane of a converging APB with $w_0 \geq 0.5\lambda$ are constructed only from the propagating spectrum and therefore are diffraction limited (see Appendix B). We have shown using PWS calculations in Fig. 4.8 that the FWHM of the longitudinal magnetic field intensity and the CFWHM of the total electric field intensity for such a converging APB are limited by the diffraction to 0.56λ and 0.43λ, respectively. In addition, we have also shown that the total magnetic field intensity is less collimated than the longitudinal magnetic field due to the presence of the strong annular-shaped transverse magnetic field. In this section, we aim at enhancing the longitudinal magnetic field of an APB and boosting its spatial magnetic resolution below the diffraction limit. To overcome the diffraction barrier, evanescent waves should be excited. One popular approach to generate evanescent waves, required for achieving spatial resolutions below the diffraction limit in microscopy, is to use a subwavelength scatterer [46].

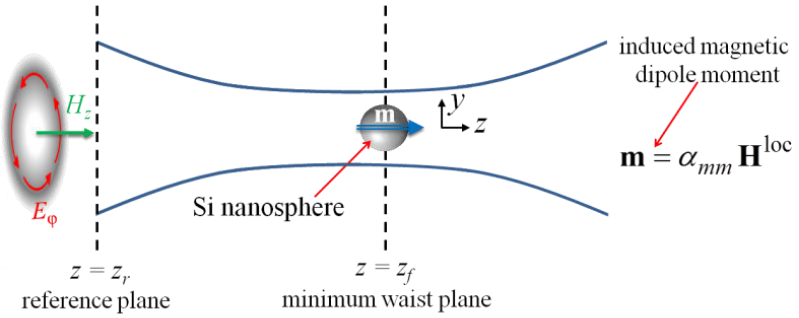

Fig. 4.12 Schematic of a converging APB with $w_0 = 0.9\lambda$ illuminating a subwavelength-size Silicon nanosphere (as a magnetic nanoprobe) placed at the actual minimum-waist plane of the beam: $r = 62\,\mathrm{nm}$, $z_f = -0.55\lambda$, $\lambda = 523\,\mathrm{nm}$.

Here, we show that a super tight magnetic-dominant spot is achieved using a subwavelength-size dense dielectric Mie scatterer (here Silicon nanosphere) having a "magnetic" Mie resonance as a magnetic nanoprobe [39]. We adopt an initial paraxial electric field distribution for the APB at a reference plane $z = z_r$ (here $z_r = -3.5\lambda$) away from the minimum-waist plane based on Eq. (4.1), as shown in Fig. 4.12. We remind that based on Appendix B, Fig. 4.6 and Fig. 4.8 and their corresponding discussions in this chapter, the APBs with beam parameters larger than $w_0 = 0.9\lambda$ can be, by a good approximation, represented by Eq. (4.1). Therefore, here we adopt $w_0 = 0.9\lambda$ for the illuminating APB to have a tight magnetic field spot. In the previous section, the propagation of such an APB was modeled using the PWS and its accurate minimum-waist plane position and field distributions are calculated. Here, we import the APB's paraxial transverse electric field distribution [given by Eq. (4.1)] into the finite integration technique in time domain solver implemented in CST Microwave Studio as a boundary field source. As a consequence of the Schelkunoff equivalence principle (PEC equivalent) implemented in CST Microwave Studio, the APB propagates towards the +*z* direction in

Fig. 4.12. The coefficient V in Eq. (4.2) is set to 0.89V such that the total power of the incident APB given in Eq. (4.13) is 1mW. In the full-wave simulations we assume a free space wavelength of $\lambda = 523\text{nm}$. The magnetic field map of the incident APB (without any scatterer yet), calculated by the time domain solver implemented in CST Microwave Studio in the *y*-*z* longitudinal plane, is shown in Fig. 4.13(a). We observe from Fig. 4.13(a) that the APB's minimum-waist plane occurs at $z_f \approx -0.55\lambda$ which is also obtained by the PWS calculations according to Fig. 4.7 (the paraxial approximation instead would estimate a focus at z=0). Next, a subwavelength-size Silicon nanosphere scatterer is placed at the APB's actual minimum-waist plane ($z = z_f = -0.55\lambda$), assumed to be in vacuum. The Silicon nanosphere has a relative permittivity equal to $\varepsilon_r = 17.1 + i\,0.084$ and radius of $r = 62\,\text{nm}$, such that its magnetic Mie polarizability magnitude peaks at $\lambda = 523\,\text{nm}$ [25]. The total magnetic field's magnitude at the presence of nanosphere (superposition of incident and scattered fields) locally normalized to the magnitude of the incident magnetic field is also shown in the *y*-*z* longitudinal plane in Fig. 4.13(b), where we observe large magnetic field enhancement at the scatterer cross section and in the vicinity of the scatterer. Note that the enhanced magnetic field is strongly localized close to the scatterer with a relatively very low side-lobe levels resulting in a very high spatial magnetic resolution. Moreover, starting from the surface of the scatterer the tight magnetic spot extends into the surroundings and drops rapidly away from the nanosphere's surface, revealing the presence of evanescent spectral fields in the near field close to the scatterer.

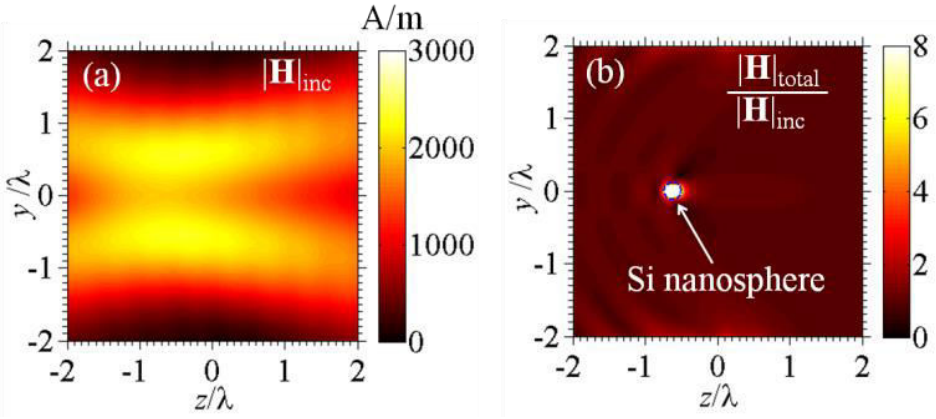

Fig. 4.13 Full-wave simulation results for the magnitude of (a) the incident magnetic field and (b) the total magnetic field (summation of incident and scattered field from the nanosphere) locally normalized to the incident magnetic field.

The normalized magnetic and electric field intensities without the presence of the scatterer (only the incident APB) at the APB's minimum-waist plane (at $z = z_f$) and with the scatterer at two different *x*-*y* transverse planes (at $z = z_f + r$ and $z = z_f + 2r$) slightly away from the scatterer are also shown in Fig. 4.14(a)-(b). In addition, Fig. 4.14(c) shows the FWHM of the total and the longitudinal magnetic near-field intensity patterns on *x*-*y* transverse planes versus the distance on the *z* axis from the nanosphere center at $z = z_f$ in positive *z*-direction. We observe from Fig. 4.14 that high resolution total magnetic near-field spots with FWHMs of 0.108λ and 0.23λ and relative side-lobe peaks of 0.018 and 0.29 (relative to the peak of the total magnetic near-field) are obtained in the transverse planes tangential to the scatterer and one radius away from the scatterer in the positive *z* direction, respectively. Note that as the distance from the nanosphere surface increases the strength of the annular-shaped transverse magnetic field component (relative to that of longitudinal magnetic field component) increases, eventually restoring the illuminating

APB's magnetic field profile. As such, the side-lobe level of the total magnetic near-field intensity pattern increases quickly for transverse planes more than $2.5r$ away from the nanosphere center, where the FWHM is not a measure of resolution anymore and therefore it is not reported for that range in Fig. 4.14(c).

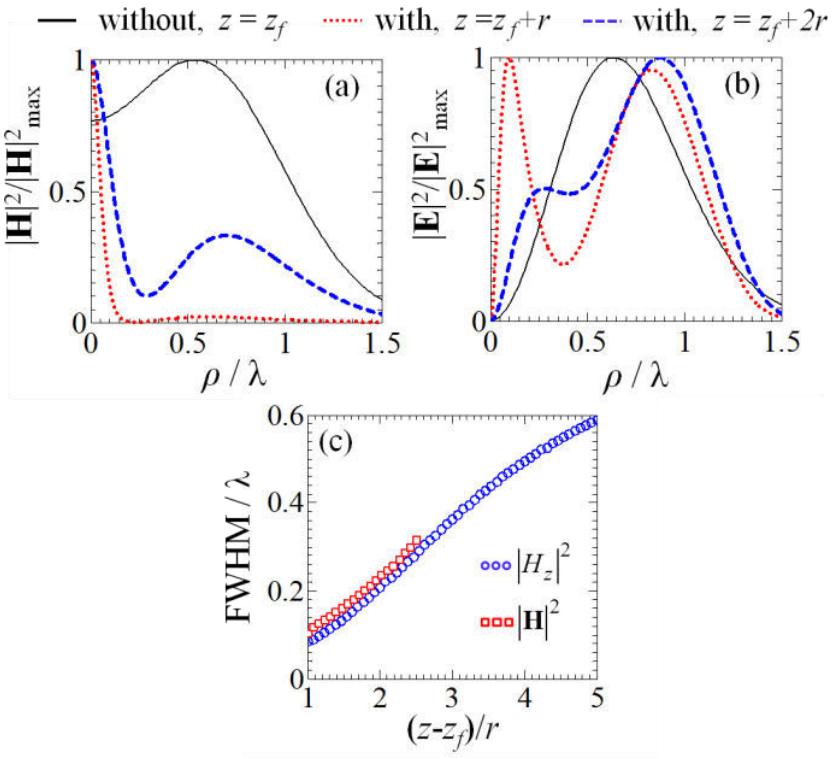

Fig. 4.14 Normalized total (a) magnetic and (b) electric near-field intensities (each case is normalized to its own maximum) without (black solid curves) and with (blue dashed and red dotted curves) the presence of the Silicon nanosphere centered at $z = z_f$, evaluated at different *x-y* transverse planes. (c) The FWHM of the total and the longitudinal magnetic near-field intensity patterns at different *x-y* transverse planes after the nanosphere.

The total magnetic field spot areas reported here (i.e., $0.009\lambda^2$ and $0.04\lambda^2$) are much smaller than the ultimate spot area obtained for the longitudinal magnetic field of a tightly focused APB with $w_0 = 0.5\lambda$ without the nanosphere which is $0.25\lambda^2$. The enhancement of the total magnetic field with respect to that of the incident APB at two different transverse

planes are also plotted in Fig. 4.15(a) where we observe a significant enhancement of the total magnetic field close to the nanosphere. The longitudinal magnetic field of the incident APB induces a magnetic dipole moment in the nanosphere polarized along the *z* direction which in turn boosts the total magnetic field thanks to the dipolar magnetic near fields. The square of the near-field admittance, defined as the total magnetic field intensity divided by the total electric field intensity, normalized to that of a plane wave ($1/\eta^2$) is also plotted in Fig. 4.15(b), which clearly shows a very high contrast ratio between magnetic and electric field especially around the beam axis. On the beam axis ($\rho = 0$) where the electric field has a null, magnetic to electric field contrast ratio goes to infinity (not shown here).

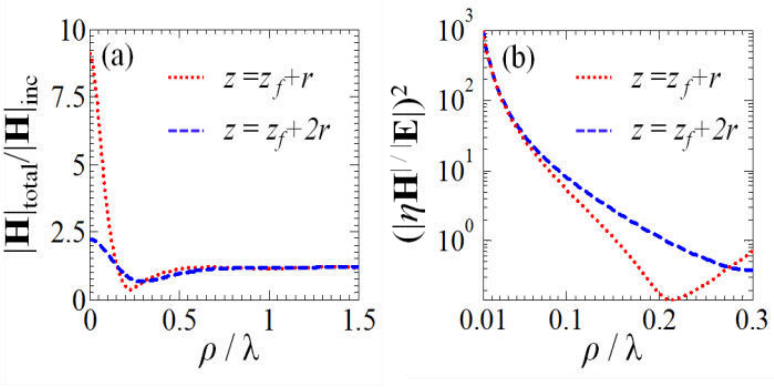

Fig. 4.15 (a) Total magnetic field (summation of incident and scattered fields) of the scatter system locally normalized to that without the nanosphere at $z = z_f$, evaluated at different transverse planes away from the scatterer. (b) Ratio of the total magnetic field intensity to the total electric field intensity of the scatter system normalized to that of plane wave (this defines the local near-field admittance normalized to that of the plane wave).

The utilization of a silicon nanosphere as a magnetic nanoprobe excited by a converging APB, which provides a tight magnetic-dominant region with enhanced magnetic and negligible electric near-fields, is especially crucial for explicit excitation of magnetic dipolar transitions in sample matters with weak magnetism at optical range. The magnetic dipolar

transitions are in general weak at optical range and overshadowed by their stronger electric counterparts. Note that when the nanosphere is utilized as a magnetic nanoprobe that boosts the magnetic response of a sample matter in its extreme vicinity, it is clear that the beam axis and the nanosphere should be perfectly aligned in order to boost only the magnetic response of the sample matter. This would be advantageous in scanning probe microscopy based on magnetism, as the extreme sensitivity to alignment would result in a high resolution mapping. In addition, in most fabrication techniques the nanosphere is either deposited on top of a substrate or embedded inside a dielectric. Most importantly, the presence of the dielectric/substrate would (i) shift the focal plane of the converging APB (depending on the relative position of the focal plane and the dielectric interface) which could be compensated when known, and (ii) change the FWHM of the longitudinal magnetic and CFWHM of the total electric near-fields inside the dielectric medium. Note that the electric field [which is purely transverse and given in Eq. (4.3)] and also the magnetic field of the APB should be continuous across the dielectric surface according to the field boundary conditions. However, since the effective wavelength inside the dielectric is shorter than that in the vacuum, the fields' features of the illuminating APB would be tighter than those belonging to the same APB propagating inside unbounded vacuum. Nevertheless, the magnetic-dominant region would be preserved across the dielectric surface.

Although in this paper a silicon nanosphere is proposed as an illustrative example of magnetic nanoprobe, other kind of the magnetic nanoprobes (such as circular clusters made of nanospheres of different geometries [39]) may be advantageous in terms of

increasing the magnetic near-field enhancement level, increasing the magnetic-dominant region size, or facilitating experimental setups.

Sec. 4.6 Conclusion

We have characterized the focusing of an azimuthally E-polarized vector beam (APB) through a lens with special attention on its magnetic-dominated region. When focusing the APB the longitudinal magnetic field strength grows relatively more than the azimuthal electric field strength, leading to a region of a boosted longitudinal magnetic field. We have also elaborated on self-standing converging APBs using plane-wave spectral (PWS) calculations and shown that longitudinal magnetic field intensity spot with full width at half maximum (FWHM) of 0.56λ and annular-shaped electric field intensity spot with complementary FWHM of 0.43λ can be achieved using a converging APB with $w_0 = 0.5\lambda$. However, the resolution of the total magnetic field intensity at a diffraction-limited APB focus is limited by the presence of the radial magnetic field in an annular-shaped region around the beam axis with comparable magnitude to the longitudinal one. In order to enhance the longitudinal magnetic field and obtain a very high total magnetic field resolution, we have proposed to utilize a magnetically polarizable (at optical frequency) particle leading to sharp magnetic near-field features. Full-wave simulation results reported here demonstrate that by placing a subwavelength-size dense Mie scatterer (here Silicon nanosphere) at the minimum-waist plane of a converging self-standing APB one achieves an extremely high resolution magnetic-dominant region with a magnetic field enhancement of about 2.3 (with respect to the incident magnetic field) and a magnetic field spot area of $0.04\lambda^2$ at a transverse plane 0.12λ away from the scatterer surface. Such a

super tight magnetic-dominant region, with enhanced magnetic and negligible electric near-fields, is essential for unambiguous excitation of magnetic dipolar transitions in materials. Especially this may be beneficial by adding an extra feature, based on magnetic near-field signature, to the future magnetism-based scanning probe microscopy and spectroscopy systems.

This chapter is reproduced based on the material in [M. Veysi, C. Guclu, F. Capolino, "Focused azimuthally polarized vector beam and spatial magnetic resolution below the diffraction limit," *Journ. Opt. Soc. Am. B*, Vol. 33, No. 11, pp. 2265-2277, 2016], © 2016 OSA.

Appendix A Field at the focal plane of a lens upon APB illumination

Let us assume that an incident paraxial APB as in Eq. (4.1)-(4.2) with beam parameter $w_{0,i}$ illuminates an infinitely-thin converging lens (Fig. 4.4). We assume the lens to be positioned at $z=0$ transverse plane where the incident APB has its minimum CFWHM. In other words, the lens is located at the incident beam's paraxial minimum-waist plane. Accordingly, the following conclusions would be still approximately valid if the incident beam's minimum-waist plane occurs at $|z| \ll z_R$ leading to $\zeta \approx 1$ and $w \approx w_0$ in Eq. (4.2). The electric field at the lens's paraxial focal plane $z = f$, on the right side of the lens in Fig. 4.4, is subsequently calculated using the Fresnel diffraction integral that in cylindrical coordinate system is written as [43]

$$\mathbf{E}_f\left(\rho,\phi,z=f\right)=\frac{k}{i2\pi f}e^{i\frac{k\rho^2}{2f}}e^{ikf}\int_0^{\infty}\int_0^{2\pi}P\left(\rho'\right)\times$$
$$\times\left(\mathbf{E}_i\left(\rho',\phi',z'=0\right)e^{i\Phi(\rho')}e^{\left(i\frac{k\rho'^2}{2f}\right)}\right)e^{-i\frac{k}{f}\rho\rho'\cos(\phi-\phi')}\rho'd\rho'd\phi' \tag{4.A1}$$

where f is the lens paraxial focal distance , $\mathbf{E}_i\left(\rho',\phi',z'=0\right)$ is the incident APB's electric field vector at the lens plane (given by Eq. (4.1) with $z'=0$), $P\left(\rho'\right)$ is the pupil function to account for the physical extent of the lens, and $\Phi\left(\rho'\right)$ is the lens-induced spherical phase given in Eq. (4.14) required to focus the beam. Under paraxial approximation, the phase term $\Phi\left(\rho'\right)$in Eq. (4.14) is approximated as

$$\Phi\left(\rho'\right)\approx-\frac{k\rho'^2}{2f} \tag{4.A2}$$

Substituting Eq. (4.A2) into (4.A1), the electric field at the lens's paraxial focal plane can be subsequently approximated as

$$\mathbf{E}_f\left(\rho,\phi,z=f\right)\approx\frac{k}{i2\pi f}e^{i\frac{k\rho^2}{2f}}e^{ikf}\times$$
$$\times\int_0^{\infty}\int_0^{2\pi}P\left(\rho'\right)\mathbf{E}_i\left(\rho',\phi',z'=0\right)e^{-i\frac{k}{f}\rho\rho'\cos(\phi-\phi')}\rho'd\rho'd\phi' \tag{4.A3}$$

For simplicity, let us first assume that the physical diameter of the lens (i.e., $2a$) is sufficiently larger than the beam waist of the incident beam, implying that almost all the incident beam power illuminates the lens. Under such assumption, the pupil function in Eq.

(4.A3) is set to one. The incident APB's electric field $\mathbf{E}_i\left(\rho',\phi',z'=0\right)$ in Eq. (4.A3) is a superposition of four linearly polarized LG beams, two *x*-pol. LG beams with $\left(l,p\right)=\left(\pm1,0\right)$ and two *y*-pol. LG beams with $\left(l,p\right)=\left(\pm1,0\right)$ [see Eq. (4.1)], where l and p are the azimuthal and radial LG beam's mode numbers, respectively. Therefore, for the sake of simplicity, we first show the steps for a general linearly polarized LG beam with mode number $\left(l,p\right)$ and beam parameter $w_{0,i}$ as the incident beam. Analogous treatment is readily applied to the all four linearly polarized LG beams that form the APB in Eq. (4.1). For an incident *x*-pol. LG beam, the electric field at the lens plane ($z=0$) is given as $\mathbf{E}_i\left(\rho',\phi',z'=0\right)=u_{l,p}\left(\rho',\phi',z'=0\right)\hat{\mathbf{x}}$. Here, we use the following integral identities [47]

$$\begin{aligned}
&\int_0^{2\pi} e^{il\phi'}\, e^{\left(\frac{-ik}{f}\rho\rho'\cos(\phi-\phi')\right)} d\phi' = 2\pi i^l\, e^{il\phi}\mathrm{J}_l\left(\frac{k}{f}\rho\rho'\right)\\
&\int_0^{\infty} \rho'^{\left(|l|+\frac{1}{2}\right)} e^{-\beta\rho'^2} L_p^{|l|}\left(\alpha\rho'^2\right) J_l\left(\frac{k\rho'\rho}{f}\right)\left(\frac{k\rho'\rho}{f}\right)^{\frac{1}{2}} d\rho' = \qquad (4.A4)\\
&=\left[\mathrm{sgn}(l)\right]^{|l|}\, 2^{-\left(|l|+1\right)}\beta^{-\left(|l|+p+1\right)}\left(\beta-\alpha\right)^p\left(\frac{k\rho}{f}\right)^{\left(|l|+\frac{1}{2}\right)} e^{\left(-\frac{k^2\rho^2}{4\beta f^2}\right)} L_p^{|l|}\left[\frac{\alpha k^2\rho^2}{4\beta f^2\left(\alpha-\beta\right)}\right]
\end{aligned}$$

where $\mathrm{J}_l\left(.\right)$ is the Bessel function of the first kind and order of l, $\mathrm{sgn}\left(l\right)$ denotes the sign of l, and $L_p^{|l|}\left(.\right)$ is the associated Laguerre polynomial [1], [12]. Accordingly, the *x*-pol. LG beam's field at the paraxial focal plane of the lens is then written as

$$\mathbf{E}_f\left(\rho,\phi,z=f\right)\approx V\left[\mathrm{sgn}(l)\right]^{|l|}\left(-1\right)^p\sqrt{\frac{2p!}{\pi\left(p+|l|\right)!}}e^{i\frac{k\rho^2}{2f}}\times$$
$$\times e^{ikf}\,\frac{i^{(l-1)}}{w_{0,f}}\left(\frac{\rho\sqrt{2}}{w_{0,f}}\right)^{|l|}e^{-\left(\frac{\rho}{w_{0,f}}\right)^2}L_p^{|l|}\left(\left(\frac{\rho\sqrt{2}}{w_{0,f}}\right)^2\right)e^{il\phi}\;\hat{\mathbf{x}} \tag{4.A5}$$

where

$$w_{0,f}=\frac{\lambda}{\pi}\frac{f}{w_{0,i}} \tag{4.A6}$$

For practical cases (as for the lens physical parameters provided in this chapter), almost all the focused beam power on the lens focal plane is confined in a circular region whose area is much smaller than $\pi f\lambda$, i.e., the focused area is within a radial distance $\rho<<\sqrt{\lambda f}$. Therefore, the phase factor $\exp\left[ik\rho^2/\left(2f\right)\right]$ in Eq. (4.A5) can be neglected and Eq. (4.A5) would clearly represent a paraxial LG beam at its minimum-waist plane with beam parameter of $w_{0,f}$. In other words, under paraxial assumption, focusing an incident LG beam through a simple lens placed at its minimum-waist plane results in another LG beam whose minimum-waist plane coincides with the lens's focal plane ($z=f$) and its beam parameter relates to the focal distance of the lens and the incident beam parameter through the Eq. (4.A6). Note that, in principle and according to Eq. (4.A6), if the radial spread of the incident LG beam determined through $w_{0,i}$ is in comparable length to the focus distance *f*, then the beam parameter of the converged beam $w_{0,f}$ would be subwavelength. However as shown in Sec. 4, physical limitations accounted by using the PWS (see [12] for details on the PWS calculations) shows that there is a limit in the

minimum achievable $w_{0,f}$. The electric field at the lens paraxial focal plane due to an incident APB is subsequently obtained by the superposition of the focal plane fields of its four constitutive linearly polarized LG beam terms leading to

$$\mathbf{E}_f = \frac{V}{\sqrt{\pi}} \frac{2\rho}{{w_{0,f}}^2} e^{-\left(\frac{\rho}{w_{0,f}}\right)^2} e^{ikf} e^{i\frac{k\rho^2}{2f}} \hat{\boldsymbol{\varphi}} \tag{4.A7}$$

In order to take into account for the physical extent of the lens, we also consider the following pupil function

$$P(\rho') = \begin{cases} 1 & \rho' \le a \\ 0 & \rho' > a \end{cases} \tag{4.A8}$$

where a is the lens radius. The pupil function in (4.A8) is expanded into a summation of Gaussian functions that come handy in taking the Fresnel integral in (4.A3) analytically. Such a pupil function is approximated with a finite summation of basis Gaussian functions as [47]

$$P(\rho') \approx \sum_{n=1}^{N} A_n e^{-\frac{B_n}{a^2}\rho'^2} \tag{4.A9}$$

where complex coefficients A_n and B_n are, respectively, expansion and Gaussian coefficients. It is demonstrated in [47] that for N = 10 the pupil function in Eq. (4.A8) is well represented by Eq. (4. A9) with proper coefficients given in [47]. By substituting Eq. (4.A9) into Eq. (4.A3), the focusing field at the focal plane $z = f$ of the finite-size lens upon illumination by an incident *x*-pol. LG beam with (l, p) is calculated as

$$\mathbf{E}_f \approx V\left[\operatorname{sgn}(l)\right]^{|l|}\sqrt{\frac{2p!}{\pi(p+|l|)!}}\,e^{i\frac{k\rho^2}{2f}}\,e^{ikf}\,\frac{i^{l-1}}{w_{0,f}}\left(\frac{\rho\sqrt{2}}{w_{0,f}}\right)^{|l|}e^{il\phi}\times$$
$$\times\sum_{n=1}^{N}A_n\left(1+\beta_n\right)^{-(|l|+p+1)}\left(\beta_n-1\right)^{p}\,e^{-\frac{\left(\rho/w_{0,f}\right)^2}{1+\beta_n}}\,L_p^{|l|}\left(\frac{\left(\frac{\rho\sqrt{2}}{w_{0,f}}\right)^2}{1-\beta_n^2}\right)\hat{\mathbf{x}} \qquad (4.A10)$$

where $\beta_n = B_n w_0^2 / a^2$, $w_{0,f}$ is given in Eq. (4.A6), and the summation over the Gaussian expansion index *n* appears in the focal field distribution term. In this way the paraxial approximation of the focusing field at the lens focal plane due to an incident *x*-pol. LG beam is conveniently expressed in series terms Eq. (4.A10) for the case of a pupil function of finite extent. The electric field at the lens paraxial focal plane due to an incident APB illumination is then calculated by the superposition of the four constitutive linearly polarized LG beam terms.

Appendix B Spectral interpretation of the beam propagation in non-paraxial regime

The electric field distribution for APB given in Eq. (4.1) represents a self-standing beam in the paraxial regime. Therefore it is important to address limitations of these paraxial expressions in the cases of beams with very tight spatial extents (small w_0). With this goal in mind, here we report in Fig. 4.16 the normalized magnitude of the plane-wave spectrum for APBs, i.e., the 2-D Fourier transform of the transverse field of the APB as

$$\tilde{\mathbf{E}}\left(k_x,k_y,z\right)=\int_{-\infty}^{+\infty}\int_{-\infty}^{+\infty}\mathbf{E}(x,y,z)\,e^{-ik_x x-ik_y y}\,dxdy \qquad (4.B1)$$

(see [12] for details on the numerical calculation of the integral). In Fig. 4.16 we show the wavenumber spectrum of three APBs with different beam parameters: (a) $w_0 = 3\lambda$, (b) $w_0 = 0.9\lambda$, and (c) $w_0 = 0.5\lambda$. It is observed from Fig. 4.16 that the plane-wave spectrum of the tighter beam (beam with smaller w_0) covers a wider region in the $k_x - k_y$ plane where $k_0 = 2\pi / \lambda$ is the free space wavenumber. Moreover the field spectral distribution for all three beams is well confined in the propagating wave spectrum with $k_x^2 + k_y^2 < k_0^2$, hence they are mainly constructed by propagating spectral components only. They propagate along the *z* axis with $\exp(ik_z z)$ where k_z is real and is evaluated as

$$k_z = \sqrt{k_0^2 - \left(k_x^2 + k_y^2\right)} \tag{4.B2}$$

All spectral magnitude distributions in Fig. 4.16 are representative at any *z* plane as these field spectral distributions propagate with no magnitude variation (implied by the propagator with magnitude $\left|\exp(ik_z z)\right| = 1$).

Let us now consider these three field distributions and look at the paraxial wave approximation. The paraxial wave equation is valid under the assumption that most of the field spectrum is confined to a region with $k_x^2 + k_y^2 << k_0^2$. Under this condition the accurate PWS evaluation can be approximated with the paraxial field expression of a propagating beam as in Eqs. (4.1)-(4.2) [44].

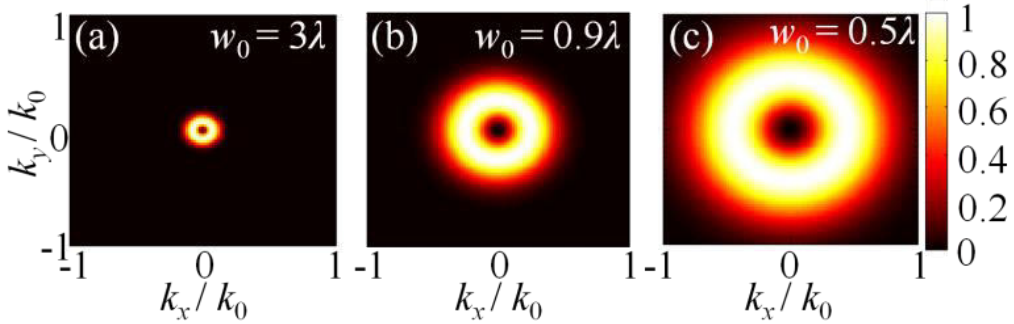

Fig. 4.16 Normalized magnitude of the transverse field spectrum $\tilde{\mathbf{E}}$ for APBs with (a) $w_0 = 3\lambda$, (b) $w_0 = 0.9\lambda$, and (c) $w_0 = 0.5\lambda$. Note that these APBs are made mainly by propagating spectrum (such that $k_x^2 + k_y^2 < k_0^2$), and therefore the spectral magnitude profiles are basically similar at any transverse plane (here we show only the propagating spectrum region).

Indeed, the required condition for deriving the paraxial field expressions using PWS calculations is to approximate Eq. (4.B2) as

$$k_z \approx k_0 - \left(k_x^2 + k_y^2\right) \Big/ \left(2k_0\right) \tag{4.B3}$$

It is observed from Fig. 4.16 that for $w_0 = 0.9\lambda$ and $w_0 = 0.5\lambda$ cases the spectral distributions cannot be fully confined to a region with $k_x^2 + k_y^2 << k_0^2$ in contrast to the case with $w_0 = 3\lambda$. Therefore, the prediction of the paraxial beam propagation is expected to deviate from the actual propagation of the beam, much more for $w_0 = 0.5\lambda$ than for $w_0 = 0.9\lambda$ and much more for $w_0 = 0.9\lambda$ than for $w_0 = 3\lambda$. The spectrums with $w_0 = 0.5\lambda$ and $w_0 = 0.9\lambda$ generate tight field spots but the *z* location of the tight spots cannot be accurately predicted by the paraxial field equations.

Especially, when considering a converging beam with $w_0 = 0.5\lambda$ or $w_0 = 0.9\lambda$, we can expect that the actual tight spot location (minimum-waist plane) will be formed closer to the reference plane than the one predicted by the paraxial expressions. This is due to the

fact that the field of the APB with $w_0 = 0.5\lambda$ or $w_0 = 0.9\lambda$ constitutes plane-wave spectral components with large transverse wave numbers which are not modeled accurately in the paraxial field expressions and propagate at larger incidence angles with respect to the beam axis (the *z* axis) and thus a tight spot forms closer than the one predicted by paraxial field expressions. The time-average spectral energy of the APB per unit length along the *z*-direction is calculated as

$$\tilde{\mathrm{W}} = \frac{1}{4}\varepsilon_0 \left|\tilde{\mathbf{E}}\right|^2 + \frac{1}{4}\mu_0 \left|\tilde{\mathbf{H}}\right|^2 \tag{4.B4}$$

We define here the figure of APB's spectral energy as the ratio of the APB's spectral energy per unit length in the propagating spectrum to its total spectral energy per unit length

$$F_{\mathrm{W}} = \iint\limits_{k_x^2+k_y^2<k_0^2} \tilde{\mathrm{W}}\, dk_x dk_y \Bigg/ \int\limits_{-\infty}^{+\infty}\int\limits_{-\infty}^{+\infty} \tilde{\mathrm{W}}\, dk_x dk_y \tag{4.B5}$$

Fig. 4.17 shows the figure of APB's spectral energy as a function of the beam parameter. It is observed that for $w_0 \geq 0.5\lambda$ more than 95% of the APB's spectral energy is confined in the propagating spectrum.

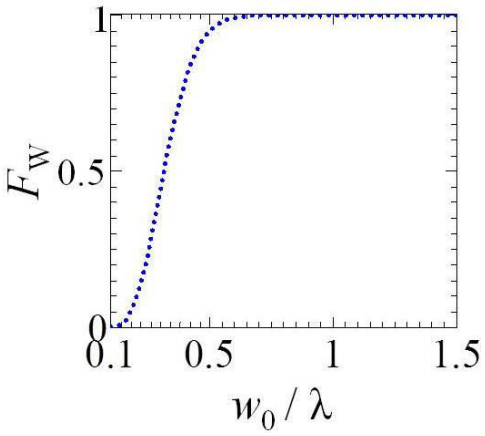

Fig. 4.17 Ratio of the APB's spectral energy per unit length (in z-direction) confined in the propagating spectrum to its total spectral energy per unit length (so-called figure of APB's spectral energy) defined in Eq. (4.B5) as a function of the beam parameter w_0.

References

[1] L. Allen, M. W. Beijersbergen, R. J. C. Spreeuw, and J. P. Woerdman, "Orbital angular momentum of light and the transformation of Laguerre-Gaussian laser modes," *Phys. Rev. A*, vol. 45, no. 11, pp. 8185–8189, Jun. 1992.

[2] D. G. Hall, "Vector-beam solutions of Maxwell's wave equation," *Opt. Lett.*, vol. 21, no. 1, p. 9, Jan. 1996.

[3] K. Youngworth and T. Brown, "Focusing of high numerical aperture cylindrical-vector beams," *Opt. Express*, vol. 7, no. 2, pp. 77–87, Jul. 2000.

[4] L. Novotny, M. R. Beversluis, K. S. Youngworth, and T. G. Brown, "Longitudinal Field Modes Probed by Single Molecules," *Phys. Rev. Lett.*, vol. 86, no. 23, pp. 5251–5254, Jun. 2001.

[5] Q. Zhan and J. Leger, "Focus shaping using cylindrical vector beams," *Opt. Express*, vol. 10, no. 7, pp. 324–331, Apr. 2002.

[6] Q. Zhan, "Cylindrical vector beams: from mathematical concepts to applications," *Adv. Opt. Photonics*, vol. 1, no. 1, p. 1, Jan. 2009.

[7] C. J. R. Sheppard, "Focusing of vortex beams: Lommel treatment," *J. Opt. Soc. Am. A*, vol. 31, no. 3, p. 644, Mar. 2014.

[8] S. Quabis, R. Dorn, M. Eberler, O. Glöckl, and G. Leuchs, "Focusing light to a tighter spot1," *Opt. Commun.*, vol. 179, no. 1–6, pp. 1–7, May 2000.

[9] R. Dorn, S. Quabis, and G. Leuchs, "Sharper Focus for a Radially Polarized Light Beam," *Phys. Rev. Lett.*, vol. 91, no. 23, p. 233901, Dec. 2003.

[10] D. P. Biss and T. G. Brown, "Cylindrical vector beam focusing through a dielectric interface," *Opt. Express*, vol. 9, no. 10, p. 490, Nov. 2001.

[11] J. R. Zurita-Sánchez and L. Novotny, "Multipolar interband absorption in a semiconductor quantum dot. II. Magnetic dipole enhancement," *J. Opt. Soc. Am. B*, vol. 19, no. 11, p. 2722, Nov. 2002.

[12] M. Veysi, C. Guclu, and F. Capolino, "Vortex beams with strong longitudinally polarized magnetic field and their generation by using metasurfaces," *J. Opt. Soc. Am. B*, vol. 32, no. 2, p. 345, Feb. 2015.

[13] M. Veysi, C. Guclu, and F. Capolino, "Large magnetic to electric field contrast in azimuthally polarized vortex beams generated by a metasurface (Presentation Recording)," 2015, vol. 9544, pp. 954408-954408–1.

[14] N. Hayazawa, Y. Saito, and S. Kawata, "Detection and characterization of longitudinal field for tip-enhanced Raman spectroscopy," *Appl. Phys. Lett.*, vol. 85, no. 25, pp. 6239–6241, Dec. 2004.

[15] Q. Zhan, "Trapping metallic Rayleigh particles with radial polarization," *Opt. Express*, vol. 12, no. 15, p. 3377, 2004.

[16] N. Davidson and N. Bokor, "High-numerical-aperture focusing of radially polarized doughnut beams with a parabolic mirror and a flat diffractive lens," *Opt. Lett.*, vol. 29, no. 12, p. 1318, Jun. 2004.
[17] B. Hao and J. Leger, "Experimental measurement of longitudinal component in the vicinity of focused radially polarized beam," *Opt. Express*, vol. 15, no. 6, p. 3550, 2007.
[18] E. Y. S. Yew and C. J. R. Sheppard, "Tight focusing of radially polarized Gaussian and Bessel-Gauss beams," *Opt. Lett.*, vol. 32, no. 23, p. 3417, Dec. 2007.
[19] G. M. Lerman and U. Levy, "Effect of radial polarization and apodization on spot size under tight focusing conditions," *Opt. Express*, vol. 16, no. 7, p. 4567, Mar. 2008.
[20] A. Yanai, M. Grajower, G. M. Lerman, M. Hentschel, H. Giessen, and U. Levy, "Near- and Far-Field Properties of Plasmonic Oligomers under Radially and Azimuthally Polarized Light Excitation," *ACS Nano*, vol. 8, no. 5, pp. 4969–4974, May 2014.
[21] R. D. Romea and W. D. Kimura, "Modeling of inverse \ifmmode \check{C}\else \v{C}\fi{}erenkov laser acceleration with axicon laser-beam focusing," *Phys. Rev. D*, vol. 42, no. 5, pp. 1807–1818, Sep. 1990.
[22] E. Y. S. Yew and C. J. R. Sheppard, "Second harmonic generation polarization microscopy with tightly focused linearly and radially polarized beams," *Opt. Commun.*, vol. 275, no. 2, pp. 453–457, Jul. 2007.
[23] T. X. Hoang, X. Chen, and C. J. R. Sheppard, "Multipole theory for tight focusing of polarized light, including radially polarized and other special cases," *J. Opt. Soc. Am. A*, vol. 29, no. 1, p. 32, Jan. 2012.
[24] P. Woźniak, P. Banzer, and G. Leuchs, "Selective switching of individual multipole resonances in single dielectric nanoparticles: Selective switching of individual multipole resonances in single dielectric nanoparticles," *Laser Photonics Rev.*, vol. 9, no. 2, pp. 231–240, Mar. 2015.
[25] C. Guclu, V. A. Tamma, H. K. Wickramasinghe, and F. Capolino, "Photoinduced magnetic force between nanostructures," *Phys. Rev. B*, vol. 92, no. 23, p. 235111, Dec. 2015.
[26] M. Kasperczyk, S. Person, D. Ananias, L. D. Carlos, and L. Novotny, "Excitation of Magnetic Dipole Transitions at Optical Frequencies," *Phys. Rev. Lett.*, vol. 114, no. 16, p. 163903, Apr. 2015.
[27] M. Burresi *et al.*, "Probing the Magnetic Field of Light at Optical Frequencies," *Science*, vol. 326, no. 5952, pp. 550–553, Oct. 2009.
[28] T. H. Taminiau, S. Karaveli, N. F. van Hulst, and R. Zia, "Quantifying the magnetic nature of light emission," *Nat. Commun.*, vol. 3, p. 979, Jul. 2012.
[29] R. Oron, S. Blit, N. Davidson, A. A. Friesem, Z. Bomzon, and E. Hasman, "The formation of laser beams with pure azimuthal or radial polarization," *Appl. Phys. Lett.*, vol. 77, no. 21, pp. 3322–3324, Nov. 2000.
[30] M. Beresna, M. Gecevičius, P. G. Kazansky, and T. Gertus, "Radially polarized optical vortex converter created by femtosecond laser nanostructuring of glass," *Appl. Phys. Lett.*, vol. 98, no. 20, p. 201101, May 2011.
[31] Z. Zhao, J. Wang, S. Li, and A. E. Willner, "Metamaterials-based broadband generation of orbital angular momentum carrying vector beams," *Opt. Lett.*, vol. 38, no. 6, pp. 932–934, Mar. 2013.
[32] X. Yi *et al.*, "Generation of cylindrical vector vortex beams by two cascaded metasurfaces," *Opt. Express*, vol. 22, no. 14, p. 17207, Jul. 2014.

[33] P. Yu *et al.*, “Generation of vector beams with arbitrary spatial variation of phase and linear polarization using plasmonic metasurfaces,” *Opt. Lett.*, vol. 40, no. 14, p. 3229, Jul. 2015.
[34] X.-L. Wang, J. Ding, W.-J. Ni, C.-S. Guo, and H.-T. Wang, “Generation of arbitrary vector beams with a spatial light modulator and a common path interferometric arrangement,” *Opt. Lett.*, vol. 32, no. 24, p. 3549, Dec. 2007.
[35] G. Volpe and D. Petrov, “Generation of cylindrical vector beams with few-mode fibers excited by Laguerre–Gaussian beams,” *Opt. Commun.*, vol. 237, no. 1–3, pp. 89–95, Jul. 2004.
[36] Z. Bomzon, G. Biener, V. Kleiner, and E. Hasman, “Radially and azimuthally polarized beams generated by space-variant dielectric subwavelength gratings,” *Opt. Lett.*, vol. 27, no. 5, pp. 285–287, Mar. 2002.
[37] M. Stalder and M. Schadt, “Linearly polarized light with axial symmetry generated by liquid-crystal polarization converters,” *Opt. Lett.*, vol. 21, no. 23, pp. 1948–1950, Dec. 1996.
[38] F. Qin *et al.*, “Shaping a Subwavelength Needle with Ultra-long Focal Length by Focusing Azimuthally Polarized Light,” *Sci. Rep.*, vol. 5, p. 9977, 2015.
[39] C. Guclu, M. Veysi, M. Darvishzadeh-Varcheie, and F. Capolino, “Artificial Magnetism via Nanoantennas under Azimuthally Polarized Vector Beam Illumination,” 2016, p. JW2A.21.
[40] C. Guclu, M. Veysi, and F. Capolino, “Photoinduced Magnetic Nanoprobe Excited by Azimuthally Polarized Vector Beam,” *ArXiv160400379 Phys.*, Apr. 2016.
[41] G. P. Agrawal and D. N. Pattanayak, “Gaussian beam propagation beyond the paraxial approximation,” *J. Opt. Soc. Am.*, vol. 69, no. 4, p. 575, Apr. 1979.
[42] B. Richards and E. Wolf, “Electromagnetic Diffraction in Optical Systems. II. Structure of the Image Field in an Aplanatic System,” *Proc. R. Soc. Lond. Math. Phys. Eng. Sci.*, vol. 253, no. 1274, pp. 358–379, Dec. 1959.
[43] J. W. Goodman, *Introduction to Fourier Optics*. McGraw-Hill, 1996.
[44] A. E. Siegman, *Lasers*. University Science Books, 1986.
[45] P. Vaveliuk, B. Ruiz, and A. Lencina, “Limits of the paraxial approximation in laser beams,” *Opt. Lett.*, vol. 32, no. 8, p. 927, 2007.
[46] G. Lerosey, J. de Rosny, A. Tourin, and M. Fink, “Focusing Beyond the Diffraction Limit with Far-Field Time Reversal,” *Science*, vol. 315, no. 5815, pp. 1120–1122, Feb. 2007.
[47] J. J. Wen and M. A. Breazeale, “A diffraction beam field expressed as the superposition of Gaussian beams,” *J. Acoust. Soc. Am.*, vol. 83, no. 5, pp. 1752–1756, May 1988.

CHAPTER 5

GENERATION OF AZIMUTHALLY POLARIZED BEAMS USING METASURFACE

Sec. 5.1 Motivation

Spectroscopy systems usually work based on electric dipole transitions, which are dominant effects in interaction of molecules and atoms with electromagnetic fields. However, it would be desirable to boost the magnetic dipole transitions, which are weaker than the electric ones, to a level that can be directly detected. It is demonstrated in [1] that the ratio of magnetic dipole to electric dipole absorption rate is proportional to the square ratio of the magnetic and the electric field, $|\mathbf{H}|^2 / |\mathbf{E}|^2$. Thus, detection of magnetic dipole transitions can be selectively boosted to rates comparable to electric dipole transitions by driving the particles with beams whose magnetic-to-electric-field ratio is purposely engineered. The magnetic-to-electric-field ratio is significant in the near field region of a very small circular aperture (like a fiber tip), and greatly enhances as the aperture radius decreases [2]. However, for practical aperture radii, the enhancement in magnetic field intensity is negligible [2]. For an azimuthally polarized beam, the magnetic-to-electric-field

ratio is significantly larger than that of a plane wave $|\mathbf{H}|/|\mathbf{E}| = 1/\eta_0$ on the beam axis where, η_0 is the free-space wave impedance [1]. Azimuthally beams are therefore promising for microscopy and spectroscopy methods based on detection of both magnetic and electric dipole transitions. Optical circular dichroism to study a vast amount of organic chiral molecules [3] would also benefit from enhancing magnetic fields.

Azimuthally polarized beams can be directly generated by coherent interference of two orthogonally polarized TEM01 laser modes [4]. In the past decades, there has been also a growing interest in novel azimuthal and radial polarizers comprising anisotropic metallic and dielectric structures with the ability to mimic polarization manipulation capabilities of the natural birefringent media. These include interferometric techniques [5], holograms [6], liquid crystal devices [7], spatial light modulators [8], multi elliptical core fibers [9]. Various flat optics devices can be also realized by plannar fabrication technologies that received considerable attention recently [10]–[12]. Space-variant gratings have been also used to convert the circularly polarized incident beams into radially or azimuthally polarized beams at far-infrared [13] and visible [14] ranges. Optical metasurfaces comprising nanoantennas offer vast flexibility in the design of space variant polarizers by spatially tailoring the polarization state of incident beam. A superposition of the radial polarizer and the fork diffraction hologram is proposed in [15] to generate radially polarized beam from circularly polarized beam. A metasurface comprising spatially rotated linear polarizers (rectangular apertures) is also proposed in [16] to convert a circularly polarized beam into vector beams. Recently, a set up consisting of an inhomogeneous half-wave plate metasurface to generate vector beams is demonstrated in [17], [18]. In this chapter, we adopt an approach similar to those in [17], [18] but with a different

metasurface element in order to increase efficiency. Furthermore, the main goal is different from [17], [18], because here we focus only on the properties and generation of azimuthally polarized beams for controlling and quantifying the longitudinal magnetic field.

In the previous chapter, we thoroughly examined the characteristics of the azimuthally polarized beams.In this chapter, we examine both analytically and numerically generation of azimuthally polarized vortex beams through interference of Laguerre Gaussian (LG) beams and study the evolution of their electric and magnetic field distributions as they propagate in a host medium. Ideally such beams possess no electric field along the beam axis where only longitudinally polarized magnetic field is present. This characteristic is the main interest of this investigation. After showing the basic principles for generating such beams, we show how these specific beams can be generated by using metasurfaces and investigate the physical parameters they should possess. The azimuthally polarized vortex beam is generated from a linearly polarized incident Gaussian beam passing through a flat inhomogeneous half-wave plate metasurface made of anisotropic nanoantennas, as shown in Fig. 5.1. Although here we are only interested in the generation of the azimuthally polarized vector beam, the proposed metasurface can be used to generate a vector beam with any desired spatial polarization distribution on the higher-order Poincaré sphere [19]. We also show where large magnetic-to-electric-field contrast ratio is obtained with the goal to describe where only intense magnetic field is present. Finally we show how focusing the generated azimuthally Polarized vortex beam through a high numerical aperture (NA) lens provides strong longitudinally-polarized magnetic field in a narrow spot on the beam axis where the total electric field is vanishing.

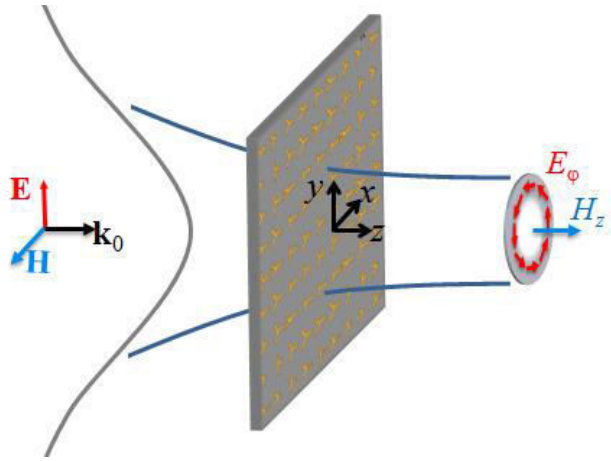

Fig. 5.1 Illustration of a flat azimuthal polarizer made of an array of anisotropic nanoantennas. The metasurface converts a focusing linearly polarized Gaussian beam to an azimuthally polarized beam with a strong longitudinally polarized magnetic field on the beam axis where the total electric field is zero.

Sec. 5.2 Theory of Azimuthally Polarized Beam Generation

In this section, a thin plasmonic metasurface capable of converting a linearly polarized incident beam into an azimuthally polarized vortex beam is conceived. In the previous chapter, we demonstrated that an azimuthally polarized vortex beam can be realized by interference of two circularly polarized LG modes with l numbers of ± 1. In this section, we first introduce the method of phase control by rotating the unit cell. Then, this phase control method is utilized to generate azimuthally polarized beams by tailoring the transverse phase profile of circularly polarized waves of opposite handedness. The transmitted wave through such a polarizing surface is analytically investigated by taking into account non-ideal unit cell characteristics; and provide analytical expressions for the resultant beam.

5.2.1 Phase Control Principle

Let us assume that a linearly polarized incident wave, $\mathbf{E}^i$, propagating in +z direction normally illuminates a metasurface made by an arbitrary shaped nanoantenna. As shown in Fig. 5.2, the reference metasurface unit cell is rotated by angle ψ about the propagation axis (z/z' axis). We define local (primed) coordinate system attached to the unit cell and global (non-primed) coordinate system with the common $z \equiv z'$ axis. It is assumed that the transmission matrix in local (primed) coordinate system related to a unit cell with a specific rotation angle ψ is known. The transmission matrix in the global coordinate system is then derived by applying rotational coordinate transformation as in [23], [24] leading to

$$\begin{pmatrix} E_x^t \\ E_y^t \end{pmatrix} = \underline{\mathbf{M}}(\psi) \begin{pmatrix} T_{x'} & 0 \\ 0 & T_{y'} \end{pmatrix} \underline{\mathbf{M}}^{-1}(\psi) \begin{pmatrix} E_x^i \\ E_y^i \end{pmatrix}$$
$$\underline{\mathbf{M}}(\psi) = \begin{pmatrix} \cos\psi & -\sin\psi \\ \sin\psi & \cos\psi \end{pmatrix}. \tag{5.1}$$

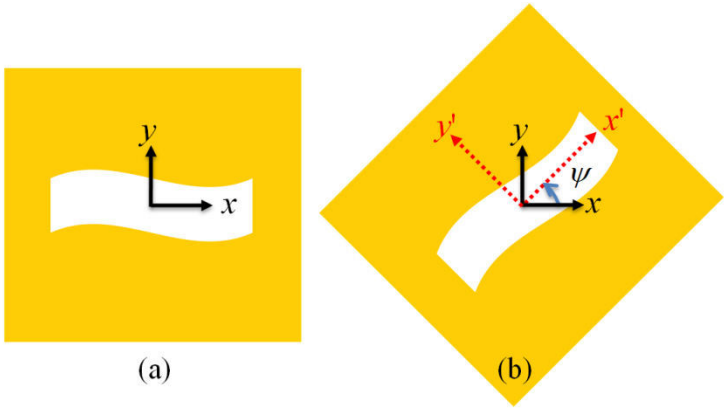

Fig. 5.2 Top view of an arbitrary shaped anisotropic slot nanoantenna unit cell. (a) Reference unit cell with zero rotation angle (local and global coordinate systems coincide with each other). (b) The same unit cell rotated by ψ degrees, indicating both local (primed) and global (non-primed) coordinate systems.

Here the subscript x, and y denote, respectively, the $x-$ and $y-$components of electric field and the superscripts t and i stand for the transmitted and incident fields, respectively. Note here that the transmission matrix of reference unit cell case in primed coordinate system is particularly chosen with null off-diagonal entries. The linearly polarized incident wave is decomposed into right (rh) and left (lh) hand circularly polarized waves as

$$\mathbf{E}^i = E^i_{rh}\hat{\mathbf{e}}_{rh} + E^i_{lh}\hat{\mathbf{e}}_{lh} \tag{5.2}$$

The transmitted wave

$$\mathbf{E}^t = E^t_{rh}\hat{\mathbf{e}}_{rh} + E^t_{lh}\hat{\mathbf{e}}_{lh} \tag{5.3}$$

is therefore composed of

$$\begin{aligned} E^t_{rh} &= E^i_{rh}\frac{A}{2} + E^i_{lh}\frac{B}{2}e^{-2i\psi} \\ E^t_{lh} &= E^i_{rh}\frac{B}{2}e^{2i\psi} + E^i_{lh}\frac{A}{2} \end{aligned} \tag{5.4}$$

in which $A = T_{x'} + T_{y'}$ and $B = T_{x'} - T_{y'}$. Note that for the ideal case with $A = 0$, the transmitted waves are purely circularly polarized waves whose phases, upon transmission through the metasurface, are delayed or progressed by twice the rotation angle of unit cell [23]–[25]. The azimuthal phase profile on the metasurface plane is achieved by spatially tailoring the metasurface with elements having varying transmission coefficients. In doing so, the unit cell is kept stationary and the phases of circularly polarized waves are locally manipulated by rotating the nanoantennas about their own axes. This approach is accurate when the mutual coupling between nanoantennas is negligible [23]–[25]. If the metasurface elements do not change rapidly along the surface, i.e., only a small variation is imposed to adjacent

elements, the local transmission properties of the metasurface can be inferred by resorting to the concept of local periodicity [10], [23], [26]. The transmission matrix of reference unit cell can be characterized in a two-dimensional infinitely periodic setup in full-wave simulations. The phase control method described here has been explored widely in the area of transmitarray and reflectarray antenna design [23]–[26]. These concepts are used in Sec. 5.3 to design a metasurface which converts a linearly polarized beam to an azimuthally polarized beam that possesses a longitudinally polarized magnetic field.

5.2.2 Metasurface Theory

Let us assume that the MS is in the $x-y$ plane and it is illuminated by a normally incident Gaussian beam linearly polarized in $a_x\hat{\mathbf{x}}+a_y\hat{\mathbf{y}}$ direction, where $|a_x|^2+|a_y|^2=1$ and a_x/a_y is a real number. The transverse-to-*z* electric field phasor of incident wave is represented in terms of circular polarizations as

$$\mathbf{E}^i_{\mathrm{FG}}=u_{0,0}(\rho,z)\left(a^i_{rh}\hat{\mathbf{e}}_{rh}+a^i_{lh}\hat{\mathbf{e}}_{lh}\right) \tag{5.5}$$

Where $a^i_{rh}=\left(a_x-ia_y\right)/\sqrt{2}$ and $a^i_{lh}=\left(a_x+ia_y\right)/\sqrt{2}$ are given coefficients and $u_{0,0}(\rho,z)$ is given in Eq. (4.2). Using the phase control method explained in the previous subsection, the phase distribution of the right and left hand circularly polarized waves on the transverse plane can be locally tailored. By rotating a nanoantenna element centered at coordinates (ρ,φ), by an angle $l_0\varphi/2$ about its center, the right- and left-hand circularly polarized incident beams, whose amplitudes are a function of incident beam polarization, are converted into left- and right-hand circularly polarized LG modes with OAM numbers l_0

and $-l_0$, respectively. A vector beam with any desired spatial polarization distribution on the higher-order Poincaré sphere with order l_0 [17], [19] can be then generated by selecting a proper incident beam polarization. Nevertheless the vector vortex beam of interest here is solely the azimuthally polarized beam as formulated in Eq. (4.1). Choosing $l_0 = 1$ leads to spatial phase dependences of OAM states $e^{i\varphi}$ and $e^{-i\varphi}$ for left- and right-hand polarized transmitted waves, respectively.

In the following we construct the transmitted field expressions for a general case with $A \neq 0$. After a certain distance from the metasurface, the resultant modes are established and the total transmitted wave is the sum of four terms with regard to Eqs. (5.3) and (5.4) yielding

$$\mathbf{E}^t = \mathbf{E}^t_{\mathrm{FG}} + \mathbf{E}^t_{\mathrm{LG}} \tag{5.6}$$

where the subscripts "FG" and "LG" stand for fundamental Gaussian and Laguerre-Gaussian, respectively. The sum of fundamental Gaussian beams, whose phases are not controlled by the rotation angle as seen in Eq. (5.4), yields a linearly polarized beam

$$\begin{aligned} \mathbf{E}^t_{\mathrm{FG}} &= u_{0,0}(\rho, z)\frac{A}{2}\left(a^i_{rh}\hat{\mathbf{e}}_{rh} + a^i_{lh}\hat{\mathbf{e}}_{lh}\right) \\ &= u_{0,0}(\rho, z)\frac{A}{2}\left(a_x\hat{\mathbf{x}} + a_y\hat{\mathbf{y}}\right) = \frac{A}{2}\mathbf{E}^i_{\mathrm{FG}} \end{aligned} \tag{5.7}$$

and the sum of LG modes with l numbers +1 and -1 generated by the rotational phase control method, is represented as

$$\mathbf{E}^t_{\mathrm{LG}} = E_1(\rho, z)\frac{B}{2}\left(a^i_{lh}e^{-i\varphi}\hat{\mathbf{e}}_{rh} + a^i_{rh}e^{i\varphi}\hat{\mathbf{e}}_{lh}\right) \tag{5.8}$$

Here $E_1(\rho,z)=E_{-1}(\rho,z)$ represents the radial field profile of $\mathbf{E}^t_{\mathrm{LG}}$ transmitted beam, and it is composed of LG modes with l numbers ±1, and $p=0,1,2,\ldots$,

$$E_{\pm1}(\rho,z)e^{i\pm\varphi}=\sum_{p=0}^{\infty}a_{\pm1,p}u_{\pm1,p} \tag{5.9}$$

as shown in Appendix B. For the case with fundamental Gaussian mode incidence as investigated here, the modes with $p=0$ (with the coefficients $a_{\pm1,0}$) will be the dominant modes in Eq. (5.9). Note that $u_{+1,p}/e^{i\varphi}=u_{-1,p}/e^{-i\varphi}$, hence from Appendix B it can be shown that $u_{+1,p}=u_{-1,p}$.

Equation (5.6) represents the two contributions to the total transmitted wave. The first one is a linearly polarized beam whereas the second one is what we want to generate for obtaining beams with space-variant polarization. It is convenient to represent the radial and azimuthal components of the total transmitted wave $\mathbf{E}^t=E^t_\rho\hat{\boldsymbol{\rho}}+E^t_\varphi\hat{\boldsymbol{\varphi}}$ as

$$\begin{aligned}E^t_\rho&=\frac{1}{2}\left[Au_{0,0}(\rho,z)\left(a^i_{rh}e^{i\varphi}+a^i_{lh}e^{-i\varphi}\right)+BE_1(\rho,z)\left(a^i_{lh}+a^i_{rh}\right)\right]\\ E^t_\varphi&=\frac{i}{2}\left[Au_{0,0}(\rho,z)\left(a^i_{rh}e^{i\varphi}-a^i_{lh}e^{-i\varphi}\right)+BE_1(\rho,z)\left(a^i_{lh}-a^i_{rh}\right)\right]\end{aligned} \tag{5.10}$$

For a purely $y-$polarized incident wave (i.e., with $a^i_{rh}=-a^i_{lh}$), when $T_{y'}=-T_{x'}$ (thus $A=0, B=2T'_x$), it is clear from Eq. (5.10) that $E^t_\rho=0$ and an azimuthally polarized vortex beam is obtained. This is also confirmed from Eq. (5.7) where the fundamental Gaussian beam contribution vanishes, and from Eq. (5.8) where the LG contribution takes the form of

Eq. (4.1) describing an azimuthally polarized beam. On the other hand, for a $x-$polarized incident wave with $a_{rh}^{i}=a_{lh}^{i}$, when $T_{y'}=-T_{x'}$, a pure radially polarized beam is obtained.

Our goal is to show that one can achieve high magnetic-to-electric-field contrast by creating an azimuthally Polarized beam under $y-$polarized incident wave. In practice, guaranteeing $A=0$ is not realistic, whereas one can implement $|A|\ll|B|$ and create a mainly azimuthally polarized beam. For this case, due to the interference of the $y-$polarized $\mathbf{E}_{\mathrm{FG}}^{t}$ and the φ-polarized $\mathbf{E}_{\mathrm{LG}}^{t}$ contribution, the transverse electric field null does not appear at $\rho=0$ and slightly shifts on the x axis (where $\hat{\boldsymbol{\varphi}}=\pm\hat{\mathbf{y}}$ and $E_{\rho}^{t}=0$). By setting $E_{\varphi}^{t}=0$ on the $\pm x$ axis, the null transverse E-field location is found by solving

$$\pm Au_{0,0}(\rho,z)+BE_{1}(\rho,z)=0 \tag{5.11}$$

When $|A|\ll|B|$, one can still realize extremely small E-field close to the beam axis. On the other hand, there is a strong longitudinal magnetic field close to the beam axis due to the generation of azimuthally Polarized beam $\mathbf{E}_{\mathrm{LG}}^{t}$ in Eq. (5.8). Note that all the LG contributions in Eq. (5.9) with *l* numbers ±1, and $p=0,1,2\ldots$, contribute to the strong H_z on the beam axis. Thus, the strength of total H_z on the beam axis is found with a summation as

$$H_{z}=\frac{2B}{w^{2}\omega\mu\sqrt{\pi}}\left(a_{lh}^{i}-a_{rh}^{i}\right)\sum_{p=0}^{\infty}a_{1,p}\sqrt{(p+1)}\;e^{-i2(p+1)\tan^{-1}\left(\frac{z}{z_{R}}\right)}\;. \tag{5.12}$$

Sec. 5.3 Design of a Metasurface Generating an Azimuthally Polarized Beam

The proof of the proposed concept is shown in this section for a flat azimuthal polarizer metasurface of radius 20λ designed to operate at λ =6μm to convert the linearly polarized incident Gaussian beam to an azimuthally Polarized vortex beam. A double layer double split-ring slot element illustrated in Fig. 5.3 is adopted to satisfy $T_{x'} = -T_{y'}$ condition required for generation of an azimuthally polarized beam. Two ring slots, one rotated by 90° relative to the other, are independently excited by orthogonal linear polarizations. Depending on the chosen dimensions, the two polarizations experience distinct resonance frequencies. By tuning the physical parameters, the condition $T_{x'} \approx -T_{y'}$ can be realized at the operating frequency, which lies between the two properly designed resonance frequencies. The double layer cell is chosen due to its higher transmission amplitude than that of the single layer cell [27]. Other geometries can be also devised for analogous transmission property, i.e., the condition $T_{x'} = -T_{y'}$.

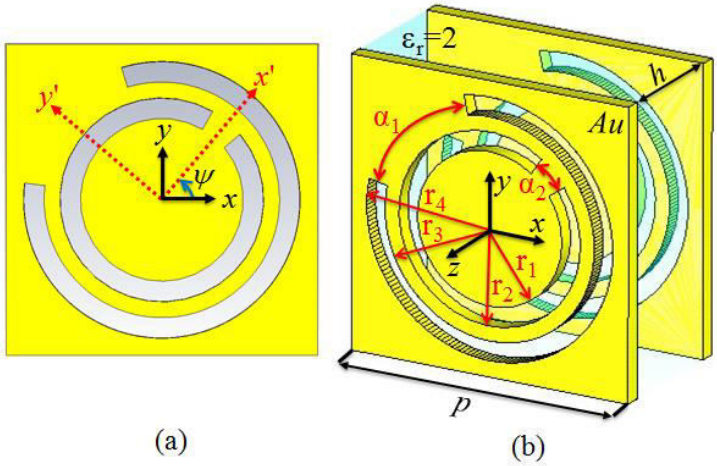

Fig. 5.3 (a) top view, and (b) 3D view of a double-layer double-ring slot resonator: $r_1 = 0.63\mu m$, $r_2 = 0.79\mu m$, $r_3 = 0.9\mu m$, $r_4 = 1.06\mu m$ $\alpha_1 = 66°$, $\alpha_2 = 20°$, $h = 1\mu m$, $p = 2.4\mu m$.

The array element with rotation angle $\psi = 0°$ is characterized in an infinite array setup under normal incidence using the finite element method implemented in CST Microwave Studio frequency domain solver, and its amplitude and phase of transmission coefficients are plotted in Fig. 5.4 versus frequency. It is observed that at the operating frequency (50THz) the transmission coefficients for $x'-$and y'-polarized waves are of equal amplitude (with the insertion loss of 4.6dB) and have a 164° phase difference. This characteristic means that $T_{x'} \approx -T_{y'}$, i.e. $|A| = 0.1697$ and $|B| = 1.2072$ with $|A| \ll |B|$. Hence the resultant transmitted beam will be mainly azimuthally Polarized with weight B, and there will be a remnant of Gaussian beam with linear polarization in the transverse plane, with weight A. In general, other unit cell elements can be used, considering also more metasurface layers, to further decrease the insertion losses at mid-infrared and to further minimize the ratio $|A/B|$.

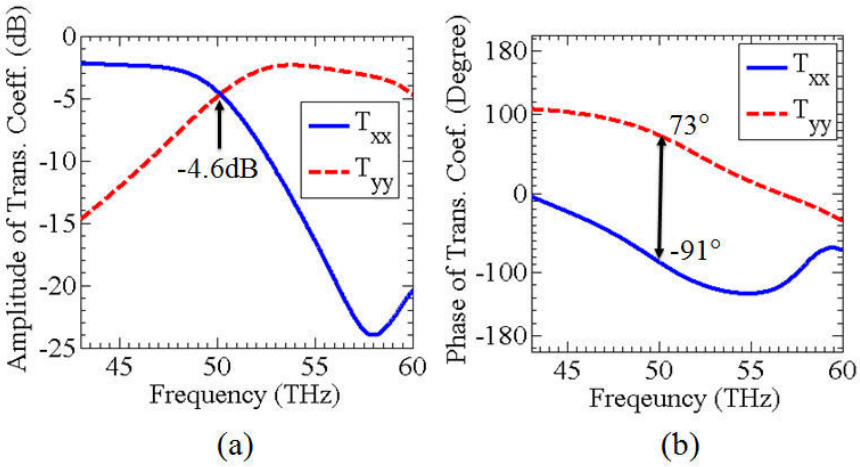

Fig. 5.4 (a) amplitude and (b) phase of the transmission coefficients for the $x-$and $y-$ polarized incident waves. The results obtained for the reference nanoantenna with rotation angle $\psi = 0°$.

Based on the phase control method described in Sec. 5.2, the transmission

characteristics of rotated elements are derived from the characteristics of reference one with $\psi = 0°$. One can estimate the transmitted field at every cell location by resorting to the concept of rotation and local periodicity discussed in Sec. 5.2, without the need of characterizing all possible unit cell configurations and the whole metasurface in full-wave simulation environment. The transmitted field through the metasurface polarizer is approximated as a step function over its surface.

In the following, we utilized 2-D forward and inverse Fourier transform implemented numerically in order to model the propagation of transmitted beam through the metasurface. The transmitted electric field over a unit cell at a very short distance of the metasurface is approximated with uniform distribution over each unit cell and evaluated as $\mathbf{E}_{cell}\left(\rho_{cell},\varphi_{cell}\right) = \underline{\mathbf{T}}\left(\psi = \varphi_{cell}/2\right)\mathbf{E}_g^i\left(\rho_{cell},\varphi_{cell}\right)$ where $\underline{\mathbf{T}}\left(\psi\right)$ is the transmission tensor of the nanoantenna element rotated by the angle ψ, (ρ_{cell}, φ_{cell}) is the position of the center of unit cell. This is the field profile over the metasurface that generates the beam as in Eq. (5.6) further away from the surface. Propagation of the transmitted field through the metasurface is determined by first Fourier transforming the transverse piece-wise approximated electric field just over the transmission side of the polarizing metasurface assumed to be at $z = z_0$. This spectral transverse E-field is evaluated based on the Fourier transform formula

$$\tilde{\mathbf{E}}\left(k_x,k_y,z_0\right) = \int_{-\infty}^{+\infty}\int_{-\infty}^{+\infty}\mathbf{E}\left(x,y,z_0\right)e^{-ik_x x - ik_y y}dxdy\,. \tag{5.13}$$

Then the field is reconstructed by the inverse Fourier transform at any arbitrary transverse plane as

$$\mathbf{E}(x,y,z)=\frac{1}{4\pi^2}\int_{-\infty}^{+\infty}\int_{-\infty}^{+\infty}\left[\tilde{\mathbf{E}}(k_x,k_y,z_0)e^{ik_z(z-z_0)}\right]e^{ik_x x+ik_y y}dk_x dk_y . \tag{5.14}$$

Where

$$k_z=\begin{cases}\sqrt{k_0^2-\left(k_x^2+k_y^2\right)} & k_0^2\geq\left(k_x^2+k_y^2\right)\\ i\sqrt{\left(k_x^2+k_y^2\right)-k_0^2} & k_0^2<\left(k_x^2+k_y^2\right)\end{cases}. \tag{5.15}$$

The double integrals in Eqs. (5.13) and (5.14) are efficiently calculated by using a 2D FFT algorithm, where the size of entire spatial domain is $81.92\lambda\times81.92\lambda$ with spatial resolution of $\lambda/50$. The metasurface located at $z=z_0$ covers a circular area with a diameter of 40λ and the transverse E-field is set to zero outside of the metasurface area. Note that the evanescent near-field components are significant at distances very close to metasurface. The incident wave is a linearly polarized Gaussian beam and its electric field and power density at the beam center are 1V/m and 1.3mW/m^2, respectively. The total incident beam power is $3\times10^{-11}\mathrm{W}$. The beam waist of the incident Gaussian wave is set equal to the radius of azimuthal polarizer metasurface (20λ) so that 86% of the total incident beam power illuminates the metasurface. Via numerical implementations of the plane wave spectrum computations [Eqs. (5.13) and (5.14)], we first show the generated azimuthally Polarized beam's field intensities and its evolution, and then the same beam is focused using a lens, to further boost the magnetic-to-electric-field contrast.

In Fig. 5.5(a)-(b), obtained via numerical calculations, we report the intensities of total electric field and longitudinal magnetic field (polarized along the propagation axis) of the

azimuthally polarized beam generated by the metasurface on three transverse planes $z = 0.5\lambda, 5\lambda, \text{and} 10\lambda$, respectively.

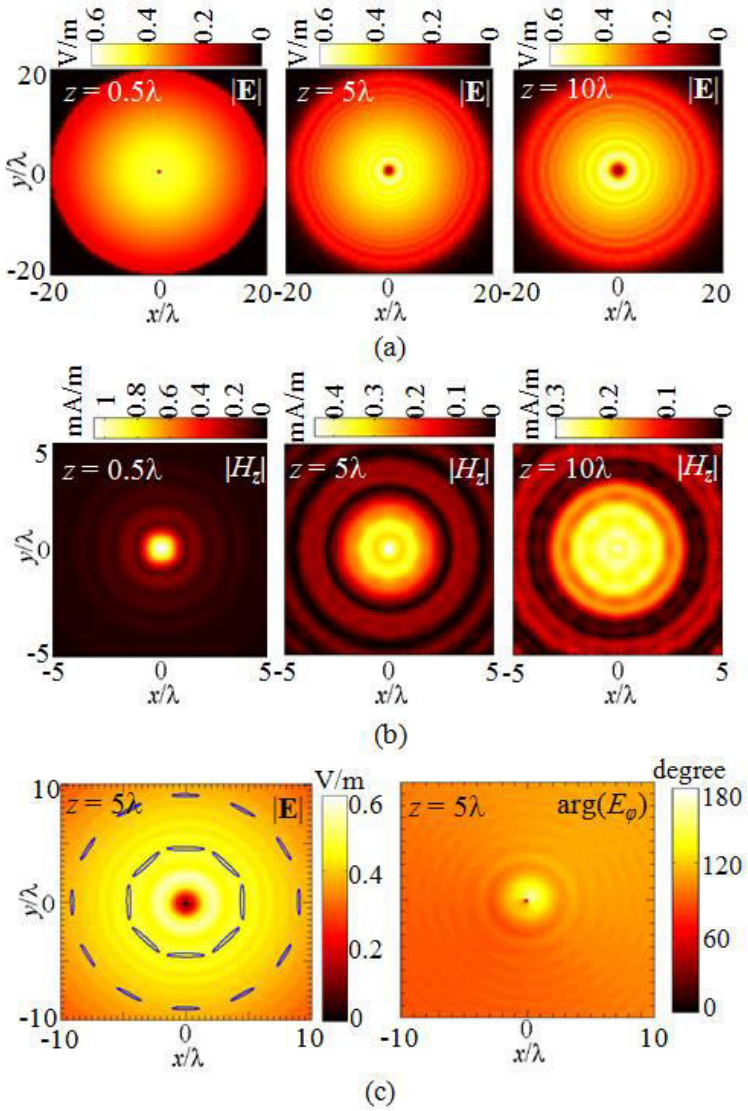

Fig. 5.5 (a) Intensity of the total electric field and (b) the longitudinal magnetic field of the azimuthally Polarized vortex beam generated by the metasurface on different transverse planes: 0.5λ, 5λ, and 10λ, , and away from the polarizer metasurface. (c) Local polarization ellipses, centered at several sample locations, superimposed to the transverse electric field intensity (left) and the phase of the azimuthally polarized electric field component on the transverse plane. All the plots are obtained through numerical calculations of Fourier transform formulas in Eqs. (5.13) and (5.14).

The beam clearly has an electric field null and a hot spot of the longitudinal magnetic field at the center on all transverse planes. These features are broadened in space as the azimuthally polarized beam propagates and diverges. Moreover we report in Fig. 5.5(c) the polarization ellipses (i.e., the trajectories of the time-domain electric field vector tip during a cycle) at several locations (superimposed to the intensity map) on the $z = 5\lambda$ transverse plane. We also plot the phase of E_{φ}^{t} on this plane in Fig. 5.5(c). The electric field has a slight polarization ellipticity (deviation from a purely linear polarization) due to the "leakage" of the incident linearly polarized Gaussian beam through the metasurface as in Eq. (5.7). A detailed discussion on this phenomenon is provided later on in a discussion regarding Fig. 5.8. Nonetheless, the azimuthally polarized electric field component is dominant as indicated by the long axes of the ellipses. As shown on the right panel, the azimuthal E-field component on a constant radius is almost in phase (a mere 20° phase variation is observed); this constitutes a clear prove of the presence of the azimuthally polarized beam. Next, we investigate the features of azimuthally Polarized vortex beam when a focusing lens of radius 20λ is placed 0.5λ away from the polarizer surface. In order to focus the azimuthally Polarized beam, a hyperboloid phase profile is added to the spatial field distribution on the lens plane [28]. The intensity of focused beam is then found in any transverse plane by numerically implementing the plane wave spectrum computations as in Eqs. (5.13) and (5.14). In Fig. 5.6, the magnitude of the total electric field (left), the longitudinal magnetic field (middle), and the normalized ratio of the total magnetic field to total electric field (right), of the focused azimuthally polarized beam at the lens focal plane are reported using lenses with different NAs. The on-axis zero electric field and annular electric field intensity distribution characteristics are clearly observed in Fig. 5.6 in

consistency with the electric field intensity distribution results reported in [29], [30], in which only the electric field intensity distribution of a tightly focused azimuthally polarized beam is examined. In contrast, here we provide a comprehensive investigation and discuss properties of the longitudinal magnetic field component of a tightly focused azimuthally polarized beam. The resultant tightly focused azimuthally Polarized vortex beam creates a strong longitudinally polarized magnetic field in a very narrow spot (vortex region) where the magnitude of total electric field is negligibly small. By duality, this is analogous to the radially polarized beam for which the longitudinal electric field component is strong in a narrow spot [1], [31].

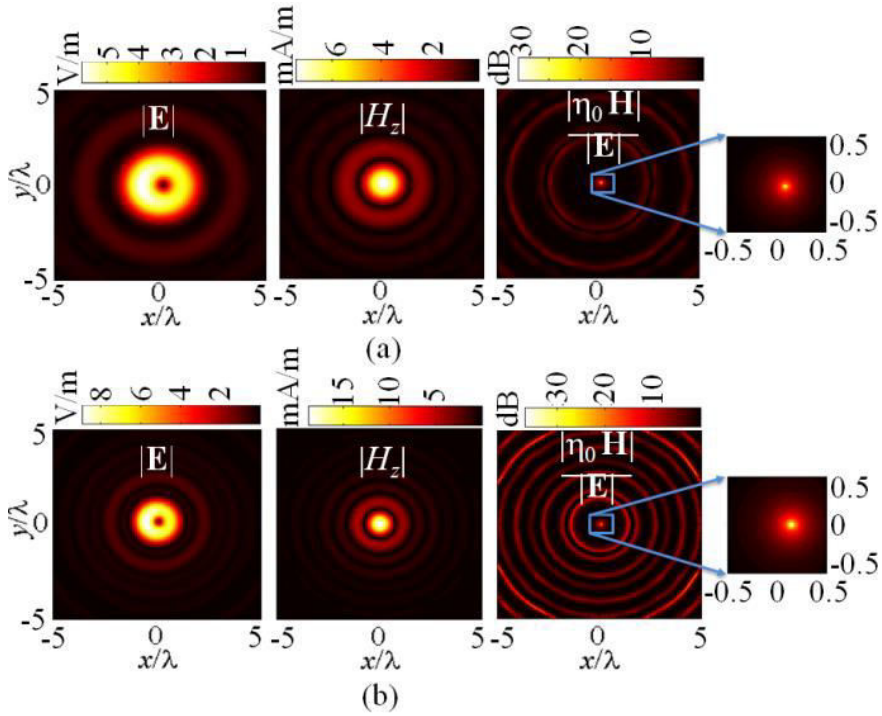

Fig. 5.6 The total electric field $|\mathbf{E}|$ (left), the longitudinal magnetic field $|H_z|$ (middle), and the normalized magnetic-to-electric-field ratio $|\eta_0\mathbf{H}|/|\mathbf{E}|$ (right) of a tightly focused azimuthally polarized beam at the focal plane for lenses of radius 20λ with different NAs: (a) NA=0.45 $(f=40\lambda)$, and (b) NA=0.7 $(f=20\lambda)$. The magnetic-to-electric-field contrast ratio is normalized to its value for plane wave.

Note that the electric field null slightly shifts away from the exact origin, this is due to the "leakage" of the original linearly polarized Gaussian beam in Eq. (5.7) through the metasurface as we will discuss in details regarding Fig. 5.8. Focusing the azimuthally Polarized vortex beam through a lens with either NA of 0.45 or 0.7 enhances the magnetic field levels up to 7.2 to 18 times, respectively. Moreover this results in boosted levels of $|\eta_0\mathbf{H}|/|\mathbf{E}|$. Even though we observe circular regions of $|\eta_0\mathbf{H}|/|\mathbf{E}|$ maxima in Fig. 5.6 the magnetic field is maximum at the central region. In both cases the null of electric field and the maximum of longitudinal magnetic field are close to the center, because of the interference of the fundamental Gaussian beam with the LG modes.

In Fig. 5.7, the total electric field intensity, the longitudinal magnetic field intensity and the magnetic-to-electric-field-contrast ratio on the *x*-*z* plane are reported, clearly showing the large magnetic field and ratio $|\eta_0\mathbf{H}|/|\mathbf{E}|$ values on the beam axis along the depth of focus. The null of electric field along the z axis region is clearly visible, where the magnetic field reaches maximum. In Fig. 5.8, we report the square of the normalized magnetic-to-electric-field-contrast ratio $|\eta_0\mathbf{H}|^2/|\mathbf{E}|^2$ versus the radial position on the *x* axis for the same cases in Fig. 5.6. The square of the normalized contrast ratios exhibit maxima of 1600 and 1684 for lenses with NAs of 0.45 and 0.7, respectively. The location of maxima moves toward to the origin with increasing NA. The slight shift of the maximum of magnetic-to-electric-field-contrast ratio from the origin in the *x*-*y* plane is attributed to the interference with the linearly *y*-polarized Gaussian beam leaking (i.e., transmitted) through the metasurface, because $A \neq 0$ in Eq. (5. 7). The non-zero coefficient A is due to the designed unit cell which locally introduces a 164° phase difference between the transmission

coefficients for the $x'-$ and $y'-$ polarized incident waves rather than the ideal required 180° phase difference. Indeed, the azimuthally Polarized beam is *y*-polarized along the *x* axis, which explains why the *y*-polarized fundamental Gaussian and the LG beams interfere there. Moreover, the leaked linearly polarized Gaussian beam also possesses a very small longitudinally polarized electric field component at $\rho \neq 0$, therefore the normalized magnetic-to-electric-field-contrast ratio assumes finite value, though still very large, at its maximum, and it does not tend to infinity on the axis as it would occur for a symmetric and ideal azimuthally polarized LG beam.

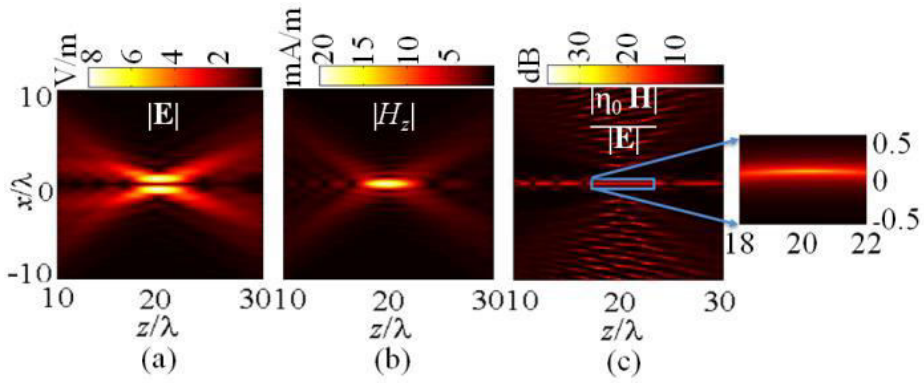

Fig. 5.7 Simulation results for fields in the longitudinal plane generated by a system composed by a polarizer metasurface followed by a lens. The polarizer and lens are placed at $z=0$, and $z=0.5\lambda$, respectively. The focal length of lens with NA =0.7 is $f=20\lambda$. (a) Magnitude of the total electric field and (b) the longitudinally polarized magnetic field, of tightly focused azimuthally Polarized beam in the longitudinal *x*-*z* plane. (c) Normalized magnetic-to-electric-field ratio, showing large values along the *z*-axis region.

Note that both the azimuthal polarizer and lens cannot be simply integrated into a single metasurface by using the double-layer double split-ring element, with the phase control method explained in Sec. 5.2. This method dictates that the phase shift introduced to right- and left-hand circularly polarized waves possess opposite signs [Eq. (5.4)]. Therefore, if lensing was integrated in the metasurface, the phase shift distribution designed for

converging the right-hand circularly polarized wave would lead to a divergent left-hand circularly polarized beam and vice versa due to the opposite sign of phases introduced in Eq. (5.4). Thus the azimuthally Polarized beam could not be synthesized since both right- and left-hand circularly polarized beams should have the same amplitude distribution over any transverse plane.

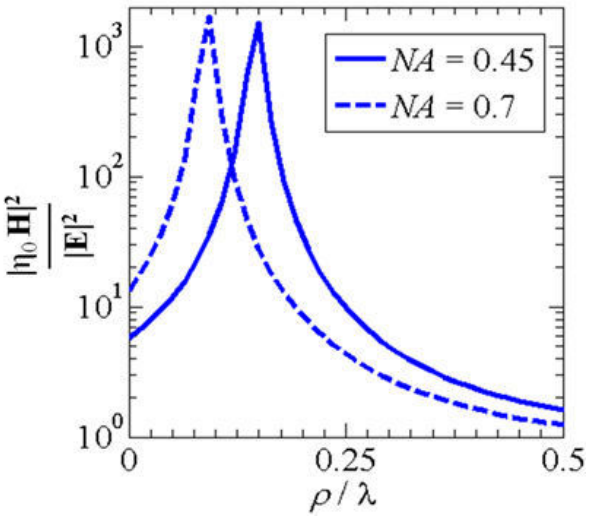

Fig. 5.8 The square of the normalized magnetic-to-electric-field contrast ratio of a tightly focused azimuthally Polarized beam as in Fig. 5.6, for the two lenses considered. The field is evaluated on the focal plane of each case, as a function of radial coordinate, for $\varphi = 0°$.

Sec. 5.4 Conclusion

We have investigated how to form an electromagnetic beam with a very large magnetic-to-electric-field ratio. It is demonstrated, both theoretically and numerically, that azimuthally Polarized vortex beams acquire a strong longitudinal magnetic field on the beam axis where the electric field vanishes. We have shown the properties a metasurface should possess in order to form such a beam and explored a specific metasurface implementation made of an array of double split ring slots. Focusing the resultant

azimuthally Polarized vortex beam significantly boosts the magnetic-to-electric-field-contrast ratio in a narrow spot on the propagation axis. The performance is limited by the fundamental Gaussian beam suppression as the beam traverses through the metasurface. Such beams may find interesting applications in the optical manipulation of particles with optical magnetic polarizability. It may also open the way to future spectroscopy systems based on magnetic dipole transitions.

This chapter is reproduced based on the material in [M. Veysi, C. Guclu, and F. Capolino, "Vortex beams with strong longitudinally polarized magnetic field and their generation by using Metasurfaces," Journ. Opt. Soc. Am. B, Vol. 32, No. 2, pp. 345-354, 2015.], © 2015 OSA.

Appendix A Vanishing Longitudinal Component of Electric Field for an Azimuthally Polarized Vortex Beam

We derive here the longitudinal electric field component of an azimuthally Polarized vortex beam. The transverse electric field of an azimuthally Polarized beam given in Eq. (4.1) is rewritten as

$$\mathbf{E}^t = E_x\hat{\mathbf{x}} + E_y\hat{\mathbf{y}} \tag{5.A1}$$

where $x-$ and $y-$ components of electric field are

$$E_x = \frac{i}{2}\left(u_{1,p} - u_{-1,p}\right), E_y = \frac{1}{2}\left(u_{1,p} + u_{-1,p}\right) \tag{5.A2}$$

By defining $u' = u_{1,p}/e^{i\varphi} = u_{-1,p}/e^{-i\varphi}$, the azimuthally Polarized electric field in Eq. (5.A1) can be rewritten as

$$\mathbf{E} = u'(\rho, z)\left(-\sin\varphi\hat{\mathbf{x}} + \cos\varphi\hat{\mathbf{y}}\right) \tag{5.A3}$$

The longitudinal electric field component can be then found from the transverse electric field components using Maxwell equations under paraxial approximations as [22]

$$E_z = \frac{i}{k}\left(\frac{\partial E_x}{\partial x} + \frac{\partial E_y}{\partial y}\right) = \frac{i}{k}\left(-\frac{\partial\left(u'(\rho, z)\sin\varphi\right)}{\partial x} + \frac{\partial\left(u'(\rho, z)\cos\varphi\right)}{\partial y}\right) \tag{5.A4}$$

After taking the derivatives and using the chain rule $\frac{\partial u'}{\partial x} = \frac{\partial u'}{\partial \rho}\frac{\partial \rho}{\partial x}$, the Eq. (5.A4) is further simplified into

$$E_z = \frac{i}{k}u'(\rho, z)\underbrace{\left(\frac{\partial\cos\varphi}{\partial y} - \frac{\partial\sin\varphi}{\partial x}\right)}_{=0} + \frac{i}{k}\frac{\partial u'(\rho, z)}{\partial \rho}\underbrace{\left(\cos\varphi\frac{\partial \rho}{\partial y} - \sin\varphi\frac{\partial \rho}{\partial x}\right)}_{=0} = 0 \tag{5.A5}$$

which demonstrates that the longitudinal component of electric field is zero everywhere in paraxial regime. Note that this salient feature of azimuthally Polarized beams is valid in the paraxial regime regardless of the radial mode number *p* of constituent LG modes with $l = \pm 1$.

Appendix B Projection of Transmitted Field Onto LG Modes

We show how to calculate the radial field profile of higher order LG modes generated by manipulating the phase distribution of the incident fundamental Gaussian mode $u_{0,0}$ upon transmission through a proper surface. When an azimuthal phase profile $e^{il_1\varphi}$ is added upon phase manipulation through a surface, one has a total field equal to $u_{0,0}e^{il_1\varphi}$ which itself does not constitute an individual LG mode solution of the paraxial wave equation. For

example, LG modes of order l_1 are characterized by a phase distribution of $e^{il_1\varphi}$, however the field radial profile of LG modes of order l_1, $u_{l_1,p}$, differ greatly from that of the incident fundamental Gaussian mode $u_{0,0}$. The field profile $u_{0,0}e^{il_1\varphi}$, on the other hand, generates all the LG modes $u_{l_1,p}$ with $p=0,1,2,\ldots$. Therefore, the total field profile of generated beam is represented as

$$u_{0,0}e^{il_1\varphi}=\sum_{p=0}^{\infty}a_{l_1,p}u_{l_1,p} \tag{5.B1}$$

which is a weighted summation of those LG modes $u_{l_1,p}$, with mode coefficients $a_{l_1,p}$. The mode excitation coefficients $a_{l_1,p}$ are found by taking the projection of transmitted field profile $u_{0,0}e^{il_1\varphi}$ onto the LG modes $u_{l_1,p}$ owing to the orthonormality of LG modes [32]

$$a_{l_1,p}=\int_0^{2\pi}\int_0^{\infty}u_{0,0}e^{il_1\varphi}u_{l_1,p}^{*}\rho d\rho d\varphi \tag{5.B2}$$

Note that due to the orthogonality of LG modes, no LG mode with $l\neq l_1$ can be generated by a phase profile $e^{il_1\varphi}$. As used in Eq. (5.8), the established beam's amplitude distribution $E_{l_1}(\rho,z)$ can be defined using

$$E_{l_1}(\rho,z)e^{il_1\varphi}=\sum_{p=0}^{\infty}a_{l_1,p}u_{l_1,p} \tag{5.B3}$$

In general, the coefficients $a_{l_1,p}$ depend strongly on the initial field profile impinging on the azimuthal polarizer metasurface (here taken as $u_{0,0}$), moreover they can be calculated numerically for any arbitrary incident field profile. Note that reversing the azimuthal phase profile added to the original field profile, which in turn becomes $u_{0,0}\,e^{-il_1\varphi}$, would result in the same radial field profile $E_{-l_1}(\rho,z)=E_{l_1}(\rho,z)$ which can be easily concluded using the identity $u_{l_1,p}/e^{il_1\varphi}=u_{-l_1,p}/e^{-il_1\varphi}$ in Eqs. (5.B2) and (5.B3).

In a more general setting, the azimuthal polarizer metasurface also scales the field strength as it manipulates the phase profile of transmitted beam. These coefficients are provided for the specific case in Eq. (5.8).

References

[1] J. R. Zurita-Sánchez and L. Novotny, "Multipolar interband absorption in a semiconductor quantum dot. II. Magnetic dipole enhancement," *J. Opt. Soc. Am. B*, vol. 19, no. 11, p. 2722, Nov. 2002.

[2] B. Hanewinkel, A. Knorr, P. Thomas, and S. W. Koch, "Optical near-field response of semiconductor quantum dots," *Phys. Rev. B*, vol. 55, no. 20, pp. 13715–13725, May 1997.

[3] E. W. Meijer and E. E. Havinga, "Optical activity in the hyperpolarizability," *Synth. Met.*, vol. 57, no. 1, pp. 4010–4017, Apr. 1993.

[4] R. Oron, S. Blit, N. Davidson, A. A. Friesem, Z. Bomzon, and E. Hasman, "The formation of laser beams with pure azimuthal or radial polarization," *Appl. Phys. Lett.*, vol. 77, no. 21, pp. 3322–3324, Nov. 2000.

[5] S. C. Tidwell, D. H. Ford, and W. D. Kimura, "Generating radially polarized beams interferometrically," *Appl. Opt.*, vol. 29, no. 15, pp. 2234–2239, May 1990.

[6] E. G. Churin, J. Hoβfeld, and T. Tschudi, "Polarization configurations with singular point formed by computer generated holograms," *Opt. Commun.*, vol. 99, no. 1–2, pp. 13–17, May 1993.

[7] M. Stalder and M. Schadt, “Linearly polarized light with axial symmetry generated by liquid-crystal polarization converters,” *Opt. Lett.*, vol. 21, no. 23, pp. 1948–1950, Dec. 1996.

[8] S. Tripathi and K. C. Toussaint, “Versatile generation of optical vector fields and vector beams using a non-interferometric approach,” *Opt. Express*, vol. 20, no. 10, pp. 10788–10795, May 2012.

[9] G. Milione *et al.*, “Cylindrical vector beam generation from a multi elliptical core optical fiber,” in *CLEO:2011 - Laser Applications to Photonic Applications*, 2011, p. CTuB2.

[10] B. Memarzadeh and H. Mosallaei, “Array of planar plasmonic scatterers functioning as light concentrator,” *Opt. Lett.*, vol. 36, no. 13, pp. 2569–2571, Jul. 2011.

[11] N. Yu *et al.*, “Light Propagation with Phase Discontinuities: Generalized Laws of Reflection and Refraction,” *Science*, vol. 334, no. 6054, pp. 333–337, Oct. 2011.

[12] N. Yu, F. Aieta, P. Genevet, M. A. Kats, Z. Gaburro, and F. Capasso, “A Broadband, Background-Free Quarter-Wave Plate Based on Plasmonic Metasurfaces,” *Nano Lett.*, vol. 12, no. 12, pp. 6328–6333, Dec. 2012.

[13] Z. Bomzon, G. Biener, V. Kleiner, and E. Hasman, “Radially and azimuthally polarized beams generated by space-variant dielectric subwavelength gratings,” *Opt. Lett.*, vol. 27, no. 5, pp. 285–287, Mar. 2002.

[14] M. Beresna, M. Gecevičius, P. G. Kazansky, and T. Gertus, “Radially polarized optical vortex converter created by femtosecond laser nanostructuring of glass,” *Appl. Phys. Lett.*, vol. 98, no. 20, p. 201101, May 2011.

[15] J. Lin, P. Genevet, M. A. Kats, N. Antoniou, and F. Capasso, “Nanostructured Holograms for Broadband Manipulation of Vector Beams,” *Nano Lett.*, vol. 13, no. 9, pp. 4269–4274, Sep. 2013.

[16] Z. Zhao, J. Wang, S. Li, and A. E. Willner, “Metamaterials-based broadband generation of orbital angular momentum carrying vector beams,” *Opt. Lett.*, vol. 38, no. 6, pp. 932–934, Mar. 2013.

[17] Y. Liu, X. Ling, X. Yi, X. Zhou, H. Luo, and S. Wen, “Realization of polarization evolution on higher-order Poincaré sphere with metasurface,” *Appl. Phys. Lett.*, vol. 104, no. 19, p. 191110, May 2014.

[18] X. Yi *et al.*, “Generation of cylindrical vector vortex beams by two cascaded metasurfaces,” *Opt. Express*, vol. 22, no. 14, p. 17207, Jul. 2014.

[19] G. Milione, H. I. Sztul, D. A. Nolan, and R. R. Alfano, “Higher-Order Poincaré Sphere, Stokes Parameters, and the Angular Momentum of Light,” *Phys. Rev. Lett.*, vol. 107, no. 5, p. 053601, Jul. 2011.

[20] J. Huang and R. J. Pogorzelski, “A Ka-band microstrip reflectarray with elements having variable rotation angles,” *IEEE Trans. Antennas Propag.*, vol. 46, no. 5, pp. 650–656, May 1998.

[21] C. Guclu, J. Perruisseau-Carrier, and O. Civi, "Proof of Concept of a Dual-Band Circularly-Polarized RF MEMS Beam-Switching Reflectarray," *Antennas Propag. IEEE Trans. On*, vol. 60, no. 11, pp. 5451–5455, Nov. 2012.

[22] E. Erdil *et al.*, "A reconfigurable microfluidic transmitarray unit cell," in *2013 7th European Conference on Antennas and Propagation (EuCAP)*, 2013, pp. 2957–2960.

[23] J. Huang and J. A. Encinar, *Reflectarray antennas*. Piscataway, N.J.; Hoboken, N.J.: IEEE Press ; Wiley-Interscience, 2008.

[24] D. Zelenchuk and V. Fusco, "Split-Ring FSS Spiral Phase Plate," *IEEE Antennas Wirel. Propag. Lett.*, vol. 12, pp. 284–287, 2013.

[25] M. Veysi, O. Boyraz, and F. Capolino, "A thin anisotropic metasurface for simultaneous light focusing and polarization manipulation," *ArXiv14060860 Phys.*, Jun. 2014.

[26] K. Youngworth and T. Brown, "Focusing of high numerical aperture cylindrical-vector beams," *Opt. Express*, vol. 7, no. 2, pp. 77–87, Jul. 2000.

[27] Q. Zhan and J. Leger, "Focus shaping using cylindrical vector beams," *Opt. Express*, vol. 10, no. 7, pp. 324–331, Apr. 2002.

[28] L. Novotny, M. R. Beversluis, K. S. Youngworth, and T. G. Brown, "Longitudinal Field Modes Probed by Single Molecules," *Phys. Rev. Lett.*, vol. 86, no. 23, pp. 5251–5254, Jun. 2001.

[29] W. L. Erikson and S. Singh, "Polarization properties of Maxwell-Gaussian laser beams," *Phys. Rev. E*, vol. 49, no. 6, pp. 5778–5786, Jun. 1994.

[30] P. M. Tannenbaum, "Expansion of a plane wave in terms of Laguerre-gaussian functions and the spectral response of Selfocs®," *J. Opt. Soc. Am.*, vol. 65, no. 1, pp. 56–58, Jan. 1975.

CHAPTER 6

Reflectarrays Carrying Orbital Angular Momentum (OAM) and Their Applications in Satellite Communications

Sec. 6.1 Motivation

The orbital angular momentum (OAM) of light plays an important role in optics and electromagnetics and has been considered in various wireless communication systems [1]–[4]. In this chapter, we revisit the OAM beam concept by focusing on its far-field features. In particular, based on our findings we propose novel cone-shaped pattern and azimuthal multi-beam antennas for wireless and satellite communication systems.

A. Orbital Angular Momentum (OAM) beams: background and applications

It is known in classical electrodynamics that electromagnetic waves carry angular momentum in addition to the linear momentum [5]. The angular momentum of an electromagnetic wave is calculated as the volume integral of the cross product of the wave Poynting vector and the position vector (i.e., $\mathbf{r}$) over a free space volume V as

$\mathbf{J} = \varepsilon_0 \int \mathbf{r} \times \mathrm{Re}\left\{\mathbf{E} \times \mathbf{B}^*\right\} dV$ where ε_0 is the free space permittivity and asterix $(*)$ denotes complex conjugate [5]–[7]. Therefore, in order for a beam traveling along the *z*-axis, to have a non-vanishing angular momentum along the beam axis (i.e., $J_z \neq 0$), the Poynting vector of the beam must have a non-zero component transverse to the beam axis. The angular momentum of an electromagnetic beam has two components: (i) intrinsic, also named spin angular momentum (SAM) with a mode number denoted by *s*, and (ii) extrinsic which is OAM with mode number denoted by *l*. The SAM is associated with the circular polarization of a beam, while the OAM of a beam is associated with its field's azimuthal phase distribution rather than its polarization. The total angular momentum mode number is *j*=*l*+*s*, and is explicitly calculated by $j = J_z / W$, where *W* is the beam energy in the same volume *V* [5]–[7]. Since the detection of OAM in helical beams in 1992 [1], laser beams with twisted wavefronts carrying OAM have attracted increasing attention in the optics community and have given rise to many groundbreaking developments in optical communication systems [2]–[4], [8], [9]. An OAM-carrying beam is characterized by a unique phase distribution linearly changing with the azimuth angle (i.e., as $l\varphi$ where φ denotes the azimuth angle and l is an integer so-called OAM number or azimuthal index number) and therefore featuring a phase vortex on the beam axis (i.e., *z*-axis). The Poynting vector, as well as the dominant local wavevector, of such beams traces a helical path around the beam axis, also so-called phase vortex, and thus they are sometimes referred to as vortex beams. The properties of the well-known families of optical beams with twisted wavefronts, such as helical (Laguerre-Gaussian) beams, fundamental (zero-order) and higher-order Bessel-Gaussian beams, are summarized in Fig. 6.1. Among them the field

distributions of the OAM-carrying vortex beams (i.e., helical beams and higher-order Bessel-Gaussian beams) feature similar linearly varying azimuthal phase distributions [i.e., both contain a complex exponential term $\exp(-jl\varphi)$] but they entail different radial-phase distributions.

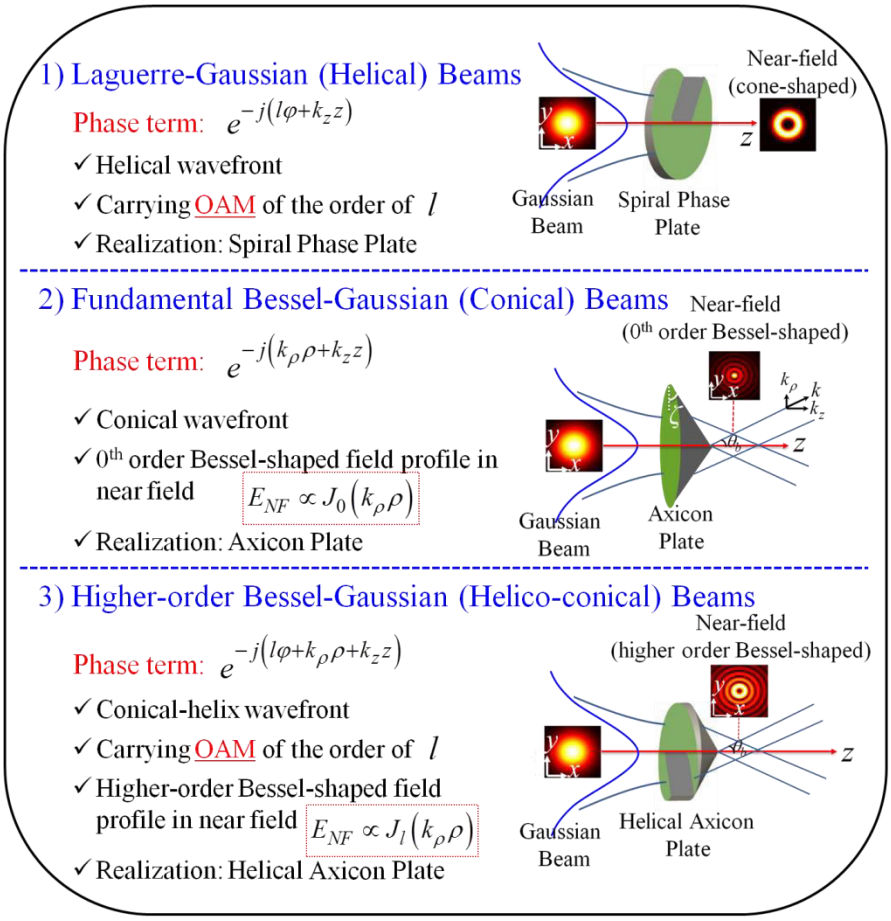

Fig. 6.1 Three known families of optical beams with twisted wavefronts and representative schematics of their generation from a fundamental Gaussian beam at its minimum waist [10], [11] (@ IEEE, 2017).

In particular, OAM-carrying vortex beams provide a complete orthogonal modal basis set [1], [3], and thus give rise to an additional set of data carriers, which does not rely on polarization or frequency. Therefore, they have the potential to increase the capacity and spectral efficiency of wireless communication links at optical range [3] and at radio

frequency (RF) [12], [13]. However, the advantage of OAM-carrying beams to increase the efficiency of RF wireless communication links is yet much of a debate since they inherently diverge with increasing distance from the transmitter [12]–[17], and therefore a very large (compared to wavelength) receiver antenna or a combination of a few antennas is required in far-field to detect the azimuthal phase variation of the field rather than sampling only the local field phase. Several techniques have been developed to generate OAM-carrying vortex beams at optical frequency ranges (such as spiral phase-plates [17], liquid crystal based spatial light modulators (SLMs) [3], plasmonic metasurfaces [4] and holograms [18]) and RF ranges (such as twisted parabolic reflectors [12], circular arrays of antennas [19], spiral phase plates [13], dielectric resonator antennas [20], and using phased array [21] and transmitarray [22] concepts). However, in order to detect the OAM information in far-field of an OAM-carrying beam source, one needs a receiving antenna which covers a sufficiently large solid angle of OAM beam to resolve the OAM phase variation. In other words, the size of the receiving antenna should linearly scale with the distance from the OAM-carrying beam source, as the OAM information is conveyed in the spatial (azimuthal) variation of the beam's phase rather than being a local property. As such, conditions of the OAM-based communication at RF and possible MIMO (multiple-in-multiple-out) applications are mainly limited to the radiating near-field (i.e., the Fresnel region) links rather than the far-field ones. Note that this may be of a less problem in OAM-based free-space optical communications with a link distance of a few meter, where the transmitter and receiver aperture diameters are usually extremely large compared to wavelength (in the order of several hundred wavelengths) [3]. OAM information can be also transferred at RF by using very large antennas (compared to wavelength) where the receiver is in the Fresnel region.

In this study we merely focus on the far-field signature of OAM-carrying beams rather than the detection of OAM information.

B. Far-field signature of OAM-carrying beams and its application

An immediate, yet remarkable, trait of the OAM-carrying vortex beams is that their field vanishes on the phase vortex center featuring an annular-shaped intensity pattern in near-field which is potentially beneficial for optical trapping [10]. Accordingly, the OAM-carrying beams lead to a cone-shaped pattern in far-field. One particular RF application that may take advantage of the vortex beam's unique field distribution is the local satellite-based navigation and guidance system serving moving vehicles. For such application satellite is usually placed in the geostationary orbit (GEO) and employs contoured beam antenna to cover a certain geographical area. In most cases, distinct location of the satellite (at a given east/west orbital position) requires a circularly polarized (CP) conical-scanned beam antenna on the mobile vehicles. In other words, the pencil beam pattern of the mobile vehicle's antenna sweeps out mechanically/electronically a cone in space. Another approach is to use an antenna, on the mobile vehicle, which radiates a fixed CP cone-shaped pattern with high azimuthal symmetry. The peak of the antenna's cone-shaped pattern points towards the satellite at the elevation angle θ_c (so-called radiation cone angle) in order to improve the signal to noise ratio, as shown in Fig. 6.2. Although different kinds of antennas have been developed to generate cone-shaped radiation pattern, such as circular patch antennas operating at higher order modes [23], phased arrays [24], bird-nest antennas [25], crosspatch fed surface wave antennas [26], leaky-wave antennas [27], and

arrays of antennas generating cone-shaped patterns [28], to name a few; they usually suffer from low bandwidth or low gain.

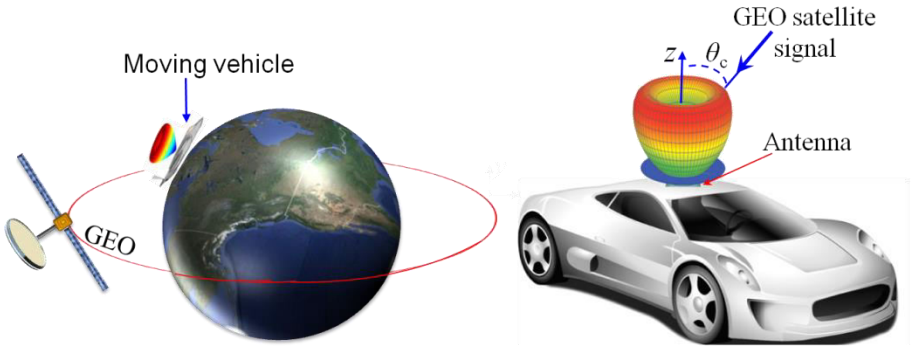

Fig. 6.2 Schematic of a GEO satellite-based navigation and guidance system serving moving vehicles (@ IEEE, 2017).

In this chapter, inspired by the unique cone-shaped far-field pattern of Bessel-Gaussian and helical beams, we investigate the generation of such beams for satellite applications with mobile vehicles at Ka-band (28GHz-32GHz). We demonstrate that reflectarray antenna is a powerful machine to systematically generate a cone-shaped OAM-carrying beam with high azimuthal symmetry. In general, the three categories of the optical beams summarized in Fig. 6.1 (i.e., helical beams, fundamental, and higher-order Bessel-Gaussian beams) feature cone-shaped far-field patterns. Here, we start our investigation by focusing on the higher-order Bessel-Gaussian beams which have both radial and azimuthal phase dependences (it provides two degrees of freedom in the design). We impose a combination of an azimuthal phase gradient and a radial one (the phase terms required for the generation of the higher-order Bessel-Gaussian beam) onto the wave reflecting back from the reflectarray surface to emulate a helical axicon phase plate at Ka-band (refer to Fig. 6.1). The proposed OAM-carrying Bessel-beam reflectarray with conical far-field pattern is a high-gain, wideband, conformal antenna, and it is simple in both design and fabrication as

an alternative to its conventional counterparts mentioned above for satellite-based navigation systems. As a proof of concept we design a reflectarray composed of CP double split-ring elements, operating from 27GHz to 33GHz. The phase profile imposed by the reflectarray surface onto the illuminating beam is then tailored by using the rotational phase control principle [29], [30]. Full-wave simulation and Fourier transform computation results of the reflectarray's far-field pattern are in good agreement exhibiting a highly symmetrical CP cone-shaped pattern. Subsequently, helical-beam reflectarray antennas are then conceived to generate cone-shaped patterns by imposing only an azimuthal phase gradient onto the wave reflecting back from the reflectarray surface, to emulate a spiral phase plate at Ka-band (see Fig. 6.1).

Next, the helical beam concept is further extended to generate multiple simultaneous pencil beams azimuthally distributed in space. To this goal, we divide the reflectarray surface into two concentric annular segments where azimuthal phase gradients (without radial phase gradients) with distinct azimuthal index numbers (OAM numbers) are imposed onto different portions of the wave illuminating the reflectarray. The interference of the overlapping cone-shaped patterns with different azimuthal phase variations radiated from these individual annular segments forms a set of finely azimuthal sectorized pencil beams in the far field with potential applications in single-point to multi-point communications, diversity, and MIMO concepts.

Sec. 6.2 FAR-FIELD FEATURES OF OAM-CARRYING BEAMS

Optical beams with twisted wavefronts as that of Laguerre-Gaussian (helical) beams, or that of fundamental and higher-order Bessel-Gaussian beams, have been thoroughly

studied within their Fresnel region [31], however, to the author's best knowledge, they have not been examined in far-field. In this section, we mainly focus on the Laguerre-Gaussian (helical) beams and the higher-order Bessel-Gaussian beams (see Fig. 6.1) and theoretically examine far-field characteristics of such beams by using the aperture field method (i.e., taking the Fourier transform of the aperture field) [32].

A. Bessel-Gaussian beams

Let us first consider a linearly polarized ideal Bessel beam which is an *exact* solution of the Helmholtz equation in the cylindrical coordinate system with the field distribution as [33]

$$\mathbf{E}^{\mathrm{BB}}\left(\rho',\varphi',z'\right)=E_0^{\mathrm{BB}}J_l\left(k_\rho\rho'\right)e^{-jl\varphi'}e^{-jk_z z'}\left(\hat{\mathbf{x}}'\pm j\hat{\mathbf{y}}'\right)\Big/\sqrt{2} \tag{6.1}$$

where $J_l(\cdot)$ is the order Bessel function of first kind [34], l^{th} - is here an integer number (so-called OAM number), E_0^{BB} is a complex amplitude coefficient, $\left(\rho',\varphi',z'\right)$ are cylindrical coordinates, and k_ρ, k_z, and $k_0=\sqrt{k_\rho^2+k_z^2}$ are radial, longitudinal and free-space wave vectors, respectively. In addition, the plus and minus signs in Eq. (6-1) indicate right-hand circularly polarized (RHCP) and left-hand circularly polarized (LHCP) waves, respectively. Throughout this paper, bold letters denote vectors and carets (^) mark unit vectors. In this chapter, we also assume the time harmonic dependence as $\exp(j\omega t)$ which is suppressed in notation for convenience. Note that equation (6-1) for $l=0$ simplifies to the field distribution of a fundamental (zero-order) Bessel beam which does not carry OAM (See Fig. 6.1). However, the ideal Bessel beams as in Eq. (6-1) are nonphysical because they carry infinite power, similar to the uniform plane waves. In this regards, Bessel-Gaussian beams

have been introduced and experimentally realized by illuminating an axicon phase plate with a Gaussian beam (see Fig. 6.1). In the following, we consider a general CP paraxial Bessel-Gaussian beam (which satisfies wave equation under *paraxial* approximation) in the transverse plane $z'=0$ with field distribution as [33]

$$\mathbf{E}^{\mathrm{BG}}\left(\rho',\varphi',z'=0\right)=E_0^{\mathrm{BG}}J_l\left(k_\rho\rho'\right)e^{-\rho'^2/w_g^2}e^{-jl\varphi'}\frac{\left(\hat{\mathbf{x}}'\pm j\hat{\mathbf{y}}'\right)}{\sqrt{2}} \tag{6.2}$$

where w_g is the beam waist of the Gaussian term controlling the transverse extent of the beam and E_0^{BG} is a complex amplitude coefficient. The far-field of the Bessel-Gaussian beam with the transverse field distribution (at $z'=0$ plane) given in Eq. (6.2) is calculated using the aperture field method which in cylindrical coordinate system is written as (see [32], chapter 12, page 711)

$$\begin{aligned}\mathbf{E}_{ff}^{\mathrm{BG}}\left(r,\theta,\varphi\right)\approx\mathbf{Q}^{\mathrm{BG}}&\int_0^{\infty}J_l\left(k_\rho\rho'\right)\exp\left(-\rho'^2/w_g^2\right)\rho'\,d\rho'\times\\&\times\int_0^{2\pi}e^{-jl\varphi'}\exp\left(jk_0\rho'\sin\theta\left[\cos\left(\varphi-\varphi'\right)\right]\right)d\varphi'\end{aligned} \tag{6.3}$$

Where

$$\mathbf{Q}^{\mathrm{BG}}=E_0^{\mathrm{BG}}\,jk_0\,e^{-jk_0r}\Big/\left(2\pi r\right)e^{\pm j\varphi}\left(\hat{\boldsymbol{\theta}}\pm j\cos\theta\,\hat{\boldsymbol{\varphi}}\right)\Big/\sqrt{2} \tag{6.4}$$

Note that equation (6.3) represents the Fourier transform of the transverse aperture field (with Bessel-Gaussian distribution) given in Eq. (6.2). Using the following integral identities [33], [34]

$$\int_0^{2\pi} e^{-jl\phi'} e^{\left[jk_\rho \rho' \cos(\phi-\phi')\right]} d\phi' = 2\pi (-j)^l J_l\left(k_\rho \rho'\right) e^{-jl\phi}$$
$$\int_0^{\infty} e^{-(p\rho')^2} J_v\left(a\rho'\right) J_v\left(b\rho'\right) \rho' d\rho' = \frac{1}{2p^2} \exp\left(-\frac{a^2+b^2}{4p^2}\right) I_v\left(\frac{ab}{2p^2}\right) \tag{6.5}$$

the far-field expression for the Bessel-Gaussian beam is then found as

$$\mathbf{E}_{ff}^{\mathrm{BG}}(r,\theta,\varphi) \approx \mathbf{Q}^{\mathrm{BG}} \pi w_g^2 (-j)^l e^{-jl\varphi} I_l\left(w_g^2 k_\rho k_0 \sin\theta/2\right) \times \exp\left(-w_g^2\left[k_\rho^2 + (k_0 \sin\theta)^2\right]/4\right) \tag{6.6}$$

Here $I_l(\cdot)$ is the $l^{\text{th}}-$order modified Bessel function of first kind [34]. For elevation angles θ away from the beam axis (i.e., the $\theta = 0$ axis), and for beams with large beam waist w_g (i.e., large apertures) the argument of the function $I_l(\cdot)$ (i.e., $\frac{1}{2} w_g^2 k_\rho k_0 \sin\theta$) is very large. Using the asymptotic expansion of the modified Bessel function for a large argument [33], [34]

$$I_l\left(w_g^2 k_\rho k_0 \sin\theta/2\right) \sim \exp\left(w_g^2 k_\rho k_0 \sin\theta/2\right) \Big/ \sqrt{\pi w_g^2 k_\rho k_0 \sin\theta} \tag{6.7}$$

the far-field expression for the Bessel-Gaussian beam given in Eq. (6.6) is then simplified as

$$\mathbf{E}_{ff}^{\mathrm{BG}}(r,\theta,\varphi) \sim \mathbf{Q}^{\mathrm{BG}} (-j)^l \sqrt{\pi/\left(k_\rho k_0\right)}\, w_g e^{-jl\varphi} \exp\left[-w_g^2\left(k_\rho - k_0 \sin\theta\right)^2/4\right] \Big/ \sqrt{\sin\theta} \tag{6.8}$$

The above far-field equation is analogous to the equation describing field distribution in the focal plane of a lens illuminated by a Bessel-Gaussian beam (calculated using Fresnel integral) as in [33]. The far-field expression in Eq. (6.8) represents a CP cone-shaped

pattern with perfect azimuthal symmetry (i.e., amplitude of the far-field expression in (6.8) is independent of φ) which peaks at the elevation angle of

$$\theta_{\mathrm{r}}^{\mathrm{BG}} = \sin^{-1}\left(k_{\rho}/k_{0}\right) \tag{6.9}$$

It is observed from Eq. (6.9) that the peak elevation angle for the Bessel-Gaussian beam in the far-field (i.e., $\theta_{\mathrm{r}}^{\mathrm{BG}}$) only depends on the radial wavenumber k_{ρ} and is independent of the beam waist w_g. The axial ratio (ratio of the magnitudes of E_{θ} and E_{φ} components) of the ideal theoretical far-field expression given in Eq. (6.8) at the elevation angle $\theta_{\mathrm{r}}^{\mathrm{BG}}$ is then obtained as

$$AR = 1/\cos\theta_{\mathrm{r}}^{\mathrm{BG}} \tag{6.10}$$

Equation (6.10) shows that as the peak elevation angle $\theta_{\mathrm{r}}^{\mathrm{BG}}$ increases, the minimum theoretically achievable axial ratio increases. The Bessel-Gaussian field distribution as in Eq. (6.2) can be generated by imposing a combination of the phase function of an axicon phase plate [which implies a radial-phase term, see Fig. 6.1] and that of a spiral phase plate [which implies an azimuthal-phase term, see Fig. 6.1] upon reflection or transmission of an incident Gaussian beam [35]. The equivalent beam waist of the Bessel-Gaussian distribution (i.e., w_g) is the half width of the normalized aperture field amplitude at $1/e$. The generated Bessel-Gaussian field distribution radiates a cone-shaped far-field pattern [as given in Eq. (6.8)] which peaks toward elevation angle $\theta_{\mathrm{r}}^{\mathrm{BG}}$ imposed only by the aperture field's radial phase gradient (i.e., k_{ρ} parameter). On the other hand, the aperture field's azimuthal phase gradient (i.e., *l* parameter) gives rise to a phase vortex on the beam axis

(i.e., the boresight direction) in far-field [due to the phase term $\exp(-jl\varphi)$ in Eq. (6.8)], which in turn results in a null in the boresight (field vanishes on the phase vortex).

B. Laguerre-Gaussian (helical) beams

Laguerre-Gaussian (helical) beams are cylindrically symmetric solutions to the paraxial wave equation in the cylindrical coordinate system and their electric field distributions in the transverse plane $z'=0$ are given as [4]

$$\begin{aligned}\mathbf{E}^{\mathrm{LG}}\left(\rho',\phi',z'=0\right)=\frac{E_0^{\mathrm{LG}}}{w_g}\sqrt{\frac{2p!}{\pi\left(p+|l|\right)!}}\left(\frac{\rho'\sqrt{2}}{w_g}\right)^{|l|}e^{-\rho'^2/w_g^2}\\ \times L_p^{|l|}\left(2\rho'^2/w_g^2\right)e^{-jl\varphi'}\left(\hat{\mathbf{x}}'\pm j\hat{\mathbf{y}}'\right)/\sqrt{2}\end{aligned} \tag{6.11}$$

where E_0^{LG} is a complex amplitude coefficient, *l* and *p* are integer numbers (so-called azimuthal and radial mode numbers, respectively), and $L_p^{|l|}(\cdot)$ is the associated Laguerre polynomial [34]. Here we consider a Laguerre-Gaussian beam with circular polarization in Eq. (6.11). The far-field of the Laguerre-Gaussian beam with the transverse field distribution given in Eq. (6.11) is then calculated using the aperture field method as

$$\begin{aligned}\mathbf{E}_{ff}^{\mathrm{LG}}\left(r,\theta,\varphi\right)\approx\mathbf{Q}^{\mathrm{LG}}\sqrt{\frac{p!}{\pi\left(p+|l|\right)!}}\int_0^\infty e^{-\rho'^2/w_g^2}L_p^{|l|}\left(2\rho'^2/w_g^2\right)\rho'^{|l|+1}d\rho'\\ \times\left(\sqrt{2}/w_g\right)^{|l|+1}\int_0^{2\pi}e^{-jl\varphi'}e^{jk_0\rho'\sin\theta\left[\cos(\varphi-\varphi')\right]}d\varphi'\end{aligned} \tag{6.12}$$

where $\mathbf{Q}^{\mathrm{LG}}$ is given in Eq. (6.4) with E_0^{BG} replaced by E_0^{LG}. Using the integral identities given in [36] (see (A4) in [36]), the far-field expression for the Laguerre-Gaussian beam with the field distribution given in Eq. (6.11) is then calculated as

$$\mathbf{E}_{ff}^{\mathrm{LG}}\left(r,\theta,\varphi\right)\approx\mathbf{Q}^{\mathrm{LG}}w_g\left(-1\right)^p\left(-j\right)^l\sqrt{2\pi\,p!/\left(p+|l|\right)!}\times \\ \times\left(\mathrm{sgn}(l)\Psi/\sqrt{2}\right)^{|l|}e^{\left(-\Psi^2/4\right)}L_p^{|l|}\left[\Psi^2/2\right]e^{-jl\phi} \tag{6.13}$$

where $\Psi=w_g k_0\sin\theta$. In the case of generation of such beams by imposing the azimuthal phase gradient onto the incident Gaussian beam (as investigated in this chapter), the Laguerre-Gaussian mode with p=0 is the dominant mode and therefore the far-field expression in Eq. (6.13) is simplified as

$$\mathbf{E}_{ff}^{\mathrm{LG}}\left(r,\theta,\varphi\right)\approx\mathbf{Q}^{\mathrm{LG}}w_g\left(-j\right)^l\sqrt{\frac{2\pi}{|l|!}}\left(\frac{\mathrm{sgn}(l)\Psi}{\sqrt{2}}\right)^{|l|}e^{\left(\frac{-\Psi^2}{4}\right)}e^{-jl\phi} \tag{6.14}$$

The above far-field expression represents a CP cone-shaped pattern with perfect azimuthal symmetry. The radiation cone angle of the cone-shaped pattern in Eq. (6.14) is then calculated as

$$\theta_{\mathrm{r}}^{\mathrm{LG}}=\sin^{-1}\left[\sqrt{2|l|}/\left(k_0 w_g\right)\right] \tag{6.15}$$

Equation (6.15) shows that for a constant l parameter the cone radiation angle decreases with increasing the beam waist of the Laguerre-Gaussian beam (i.e., the aperture diameter as we numerically show in the following sections). To make use of the far-field signatures of the Bessel-Gaussian and Laguerre-Gaussian beams, we here use reflectarray antennas to emulate the radial and azimuthal phases required for the generation of such beams with cone-shaped far-field patterns. In the following section we introduce a proper element best suited for CP reflectarray antennas operating at Ka-band (28-32GHz).

Sec. 6.3 CP Reflectarray Element

The proposed cone-shaped pattern reflectarray comprises a PEC backed flat surface decorated with CP antenna elements and is illuminated by a CP feed horn antenna. The CP reflectarray elements must highly suppress cross-polarized reflection with respect to the incident CP sense. Based on the rotational phase control principle to be used [30], we can then control the phase of the CP reflected wave (from reflectarray surface) maintaining the same CP sense as the incident wave by locally rotating the CP reflectarray elements around their centers. In order to obtain a wideband response, we here consider a double split-ring element, whose unit cell geometry is shown in Fig. 6.3. The element is characterized in a 2-D periodic-array environment under normally incident plane waves using the frequency domain solver based on the finite elements method implemented in CST microwave studio. This is a common approach that takes into account the mutual coupling between the reflectarray elements by a local periodicity assumption. The geometrical parameters of the double split-ring element (see Fig. 6.3) are optimized such that the difference between the phases of the reflection coefficients pertaining to *x*- and *y*-polarized waves [see Fig. 6.4(a)] is about 180° within the desired bandwidth (28GHz-32GHz). Therefore when a RHCP wave impinges onto the reflectarray surface, the reflected wave remains mainly RHCP.

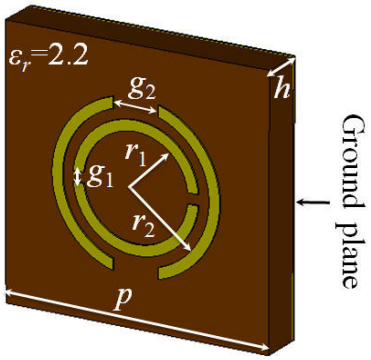

Fig. 6.3 Unit cell geometry of a double split-ring reflectarray element. The optimized parameters of the element at Ka-band are: $h = 0.81\text{mm},\ p = 5\text{mm},\ g_1 = 0.85\text{mm},\ g_2 = 0.2\text{mm},\ r_1 = 1\text{mm},$ $r_2 = 1.4\,\text{mm}$. The ring width is also set at 0.2mm(@ IEEE, 2017).

The amplitudes of the CP reflection coefficients for the co- and cross- (X-) polarized components are plotted in Fig. 6.4(b), where we observe a wide X-polarized suppression bandwidth ($\left|\Gamma_{\text{X-pol}}\right| \le -10\text{dB}$) from 27.2GHz to 32.8GHz. Note that the sense of the incident circular polarization and the element angular orientation ψ have no effect on the amplitudes of the CP reflection coefficients. The full-wave simulated reflection phase of the co-polarized component as a function of the element's angular orientation ψ is plotted at *f*=30GHz in Fig. 6.4(c) when the element is illuminated by a normally incident RHCP wave. It is observed that the reflection phase of the co-polarized component is linearly increasing by twice the angular orientation of the element as expected from the rotational phase control principle. In contrast, for an incident LHCP wave the reflection phase of the co-polarized component linearly decreases by twice the angular orientation, which is not shown here for brevity. We also observe from Fig. 6.4(c) that the reflection phase of the co-polarized component covers the full 360° phase span required to fully control the wavefront of the reflected wave. In the following section, we populate the reflectarray surface with the proposed CP elements with the fixed geometrical parameters (provided in the caption of Fig. 6.3) but an individual orientation angle ψ [as in Fig. 6.4(a)] to emulate helical axicon and spiral phase plates (See Fig. 6.1).

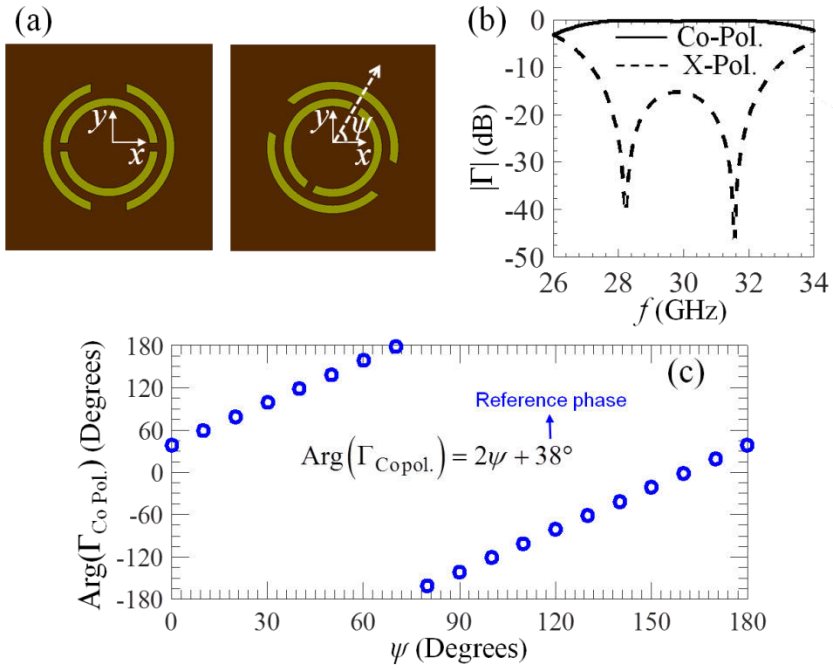

Fig. 6.4 (a) Schematic of proposed CP element unit cell and its rotation around z-axis. (b) Amplitude of the co- and cross- (X-) polarized reflection coefficients when the unit cell is illuminated by a normally incident CP wave. (c) Reflection phase of the co-polarized component versus the angular orientation of CP element for RHCP incident wave at 30GHz (@ IEEE, 2017).

Sec. 6.4 Cone-shaped Pattern Reflectarrays

By use of the CP reflectarray element designed in the previous section and the rotational phase control technique, in this section we develop Ka-band CP Bessel-beam and helical-beam reflectarrays radiating cone-shaped patterns.

A. Bessel-beam reflectarrays

In order for a reflectarray to radiate a CP Bessel beam, the required phase shift $\chi_{r,i}$ imposed by the i^{th} element on the reflectarray surface must vary depending on the element position as

$$\chi_{r,i} = k_0 d_i - \rho_i k_0 \sin\theta_r - l\varphi_i \tag{6.16}$$

where k_0 is the free-space wavenumber, d_i is the distance between the reflectarray focal point (the phase center of the feed horn as in Fig. 6.5) and the center of the i^{th} cell on the reflectarray surface, θ_r is the peak elevation angle [see Eq. (6.16)], and (ρ_i, φ_i) is the cylindrical coordinate of the i^{th} cell's center (see Fig. 6.5). The so-called OAM number *l* here is considered to be an integer; however, it can take generally any real number. The first term on the right-hand side of Eq. (6.16) cancels the propagation phase of the wave traversing from the phase center of the feed horn to the i^{th} cell's center while the second and third terms are, respectively, the required radial and azimuthal phases for generation of the Bessel-Gaussian beam. Note that in Eq. (6.16) a non-zero azimuthal index number (i.e., $l \neq 0$) is required to form a phase vortex around the *z*-axis [see Eq. (6.8)].

We first assume an ideal cos-*q* shaped RHCP incident beam illuminating the reflectarray surface. The *q*-parameter is chosen such that the incident field amplitude drops by 12dB at the reflectarray edge with respect to that at the reflectarray center [30]. Let us first consider a center-fed reflectarray with the diameter of D=7.5λ and the focal length to diameter ratio of F/D=0.7, where λ=10mm. The *q*-parameter is set to 5.7 to achieve a -12dB reflectarray edge taper for the given F/D ratio. The aim is to generate a RHCP cone-shaped pattern with cone angle of $\theta_c = 15^\circ$ (see Fig. 6.2) and a phase vortex in boresight direction (e.g., with *l*=1). The Bessel-beam reflectarray ideally imposes a local phase obtained from Eq. (6.16) (with $\theta_c = 15^\circ$) onto the incident beam. For far-field evaluations, the reflected field on the reflectarray surface is step-wise approximated and the reflected electric field at

each reflectarray cell is assumed to be uniform and equal to the incident field at the center of the cell multiplied by the required exponential phase term, $\exp\left(j\chi_{r,i}\right)$, with $\chi_{r,i}$ calculated via Eq. (6.16).

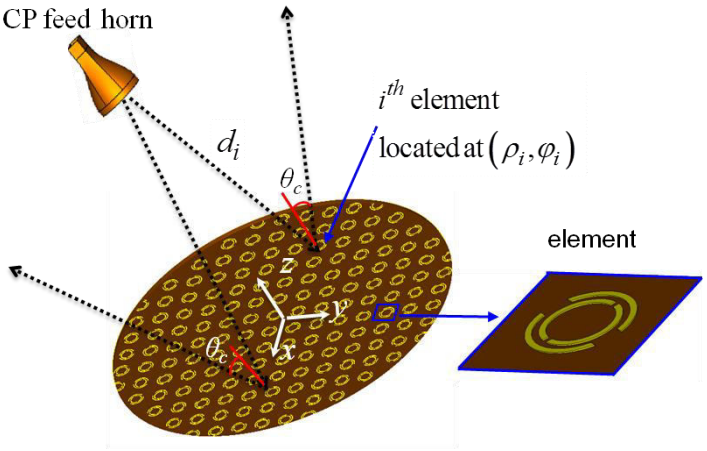

Fig. 6.5 Schematic of a reflectarray generating an OAM-carrying cone-shaped pattern (@ IEEE, 2017).

The ideal phase and amplitude of the step-sized approximated reflected field on the reflectarray surface are plotted in Fig. 6.6. Note that reflected field has a spiral-shaped phase profile on the reflectarray surface, similar to that imposed by a helical axicon phase plate onto an incident beam (See Fig. 6.1). The RHCP far-field radiation pattern is then numerically calculated via the Fourier transform of the reflected field on the reflectarray surface and plotted in Fig. 6.7. Furthermore, we also perform a full-wave simulation of the combined feed horn-reflectarray system using the CST microwave studio. The split-rings on the reflectarray surface are systematically oriented based on Fig. 6.4(c) such that the reflected wave has the spiral-shaped phase profile [as shown in Fig. 6.6(a)] over the reflectarray surface. The RHCP feed horn is oriented normal to the reflectarray surface and has a boresight gain of 13.6dB required to achieve a -12dB reflectarray edge taper.

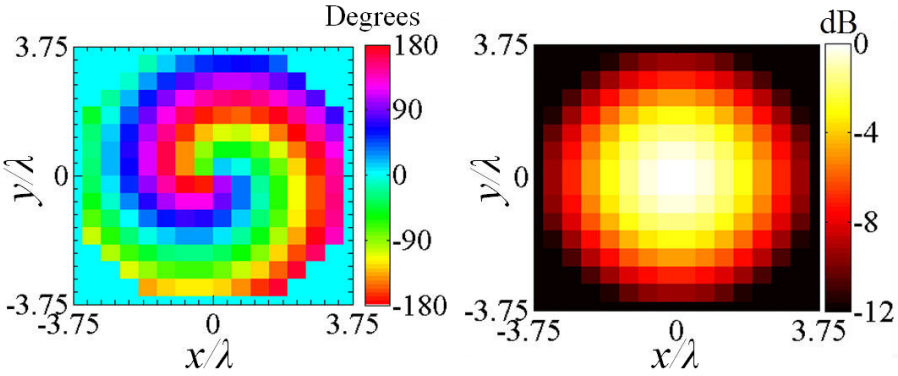

Fig. 6.6 Ideal (a) phase and (b) amplitude of the field on the Bessel-beam reflectarray's cells upon reflection from reflectarray surface. The reflectarray diameter is D=7.5λ (@ IEEE, 2017).

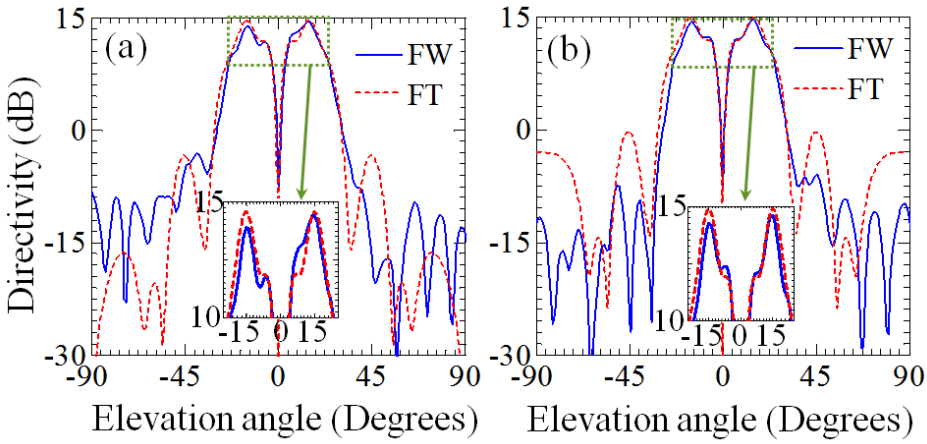

Fig. 6.7 Comparison between full-wave (FW) and Fourier-transform (FT) results for the RHCP radiation patterns of the Bessel-beam reflectarray (with D=7.5λ) at 31GHz on two different elevation planes: (a) φ = 0°, and (b) φ = 90° (@ IEEE, 2017).

The full-wave simulation also takes into account the undesirable scattering due to the illumination horn and the reflectarray's edge diffraction. The Fourier transform and the full-wave simulation results for the reflectarray's RHCP radiation patterns at two orthogonal elevation planes are compared at 31GHz in Fig. 6.7. It is observed that the Fourier transform and the full-wave simulation results are in good agreement especially around the radiation cone angle. Furthermore, the peaks of both the Fourier transform and

the full-wave radiation patterns point toward $\theta_c = 15^\circ$ which matches well with the theoretical prediction [i.e., setting $\theta_r = 15^\circ$ in Eq. (6.16)]. Note that the presence of the feed horn (i.e., blockage of the reflected fields), that is only accounted for in the full-wave simulation, does not significantly degrade the radiation of the reflectarray antenna even for a cone-shaped pattern with a radiation cone angle as small as 15° owing to its placement at the cone's vortex.

The full-wave co-polarized (RHCP) and cross-polarized (LHCP) radiation patterns of the Bessel-beam reflectarray are plotted at various frequencies in Fig. 6.8. The maximum antenna directivity in the elevation angle (radiation cone angle) of $\theta_c = 15^\circ$ is ~14.6dB and occurs at 31GHz. It is also observed from Fig. 6.8 that the cone-shaped radiation pattern of the reflectarray is mostly preserved over the frequency range of interest from 28GHz to 33GHz. However the cross-polarized radiation (whose phase is not tailored by the rotational phase control method utilized here) becomes significant at 33GHz. This is mainly attributed to the high cross-polarized reflection coefficient amplitude of the element at 33GHz [see Fig. 6.4(b)]. The RHCP radiation pattern of the Bessel-beam reflectarray is also plotted on the $\theta = \theta_c = 15^\circ$ azimuth cone for various frequencies in Fig. 6.9 which demonstrates a good azimuthal symmetry for the cone-shaped radiation pattern within the frequency band of interest. The maximum directivity variation in the azimuth cone within the frequency range of interest is about 2dB and occurs at 32GHz. Since the Fourier transform results agree well with the full-wave results (see Fig. 6.7), in the following we conduct the parametric analyses based on just the Fourier transform calculations.

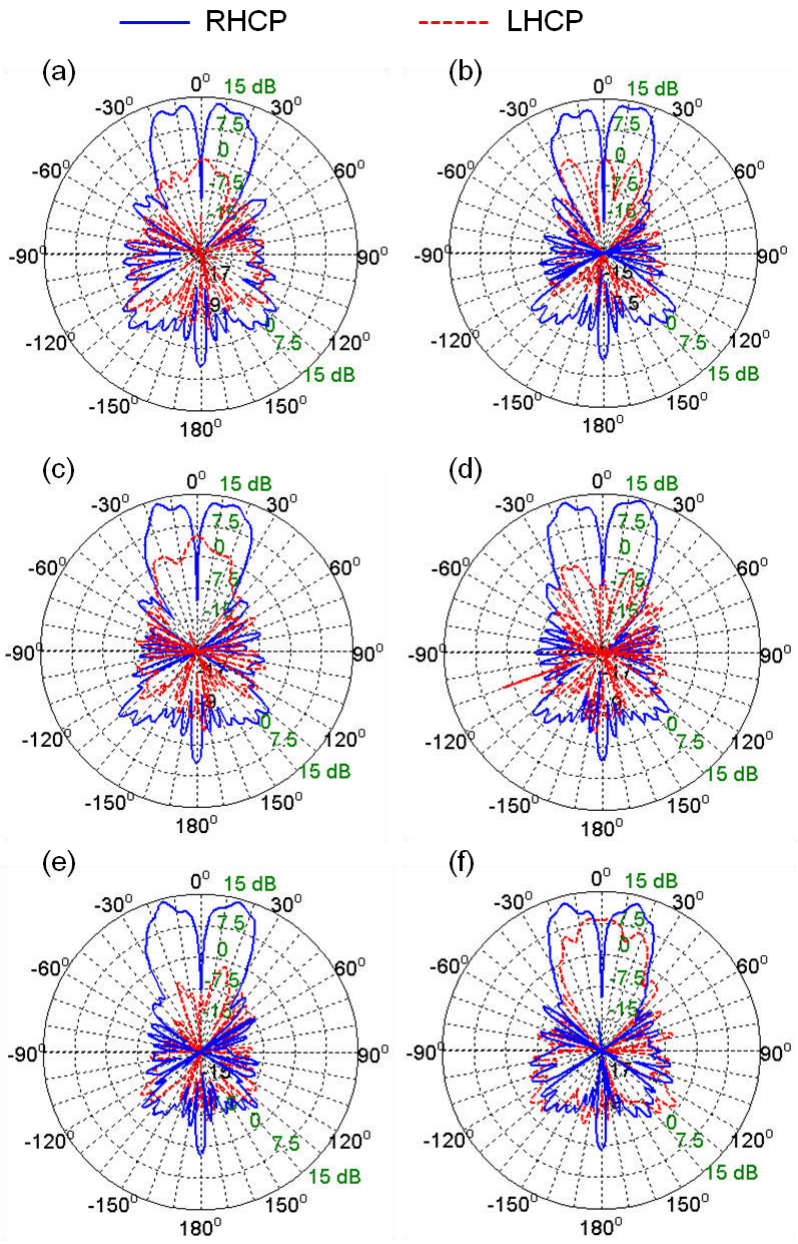

Fig. 6.8 Full-wave radiation patterns (in dB) of the Bessel-beam reflectarray (with D=7.5λ) in φ = 0° elevation plane at (a) 28GHz, (b) 29GHz, (c) 30GHz, (d) 31GHz, (e) 32GHz, (f) 33GHz (@ IEEE, 2017).

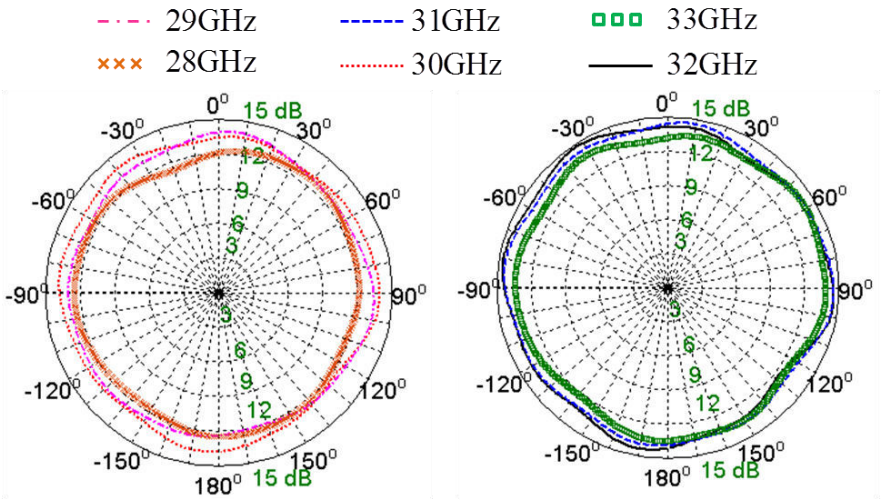

Fig. 6.9 Full-wave RHCP radiation pattern (in dB) of Bessel-beam reflectarray (with D = 7.5λ) in θ=15° azimuth cone at various frequencies (@ IEEE, 2017).

Let us first examine the effect of the azimuthal phase gradient [third term on the right hand side of Eq. (6.16)] on the Bessel-beam reflectarray's radiation pattern. Here, we increase the reflectarray diameter from 7.5λ to 30λ (with λ=10mm) while keeping the edge taper, the F/D ratio, and θ_r parameter constant as the previous design. Fig. 6.10 shows the RHCP radiation patterns for the Bessel-beam reflectarrays with [l=1 in Eq. (6.16)] and without [l=0 in Eq.(6.16)] azimuthalz phase gradient.

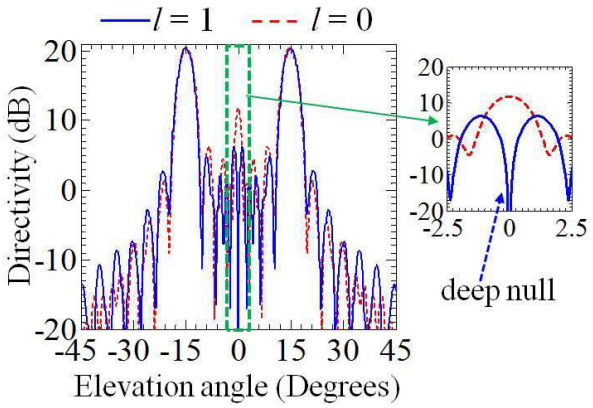

Fig. 6.10 Fourier-transform radiation pattern (in dB) of the Bessel-beam reflectarray (with D = 30λ) in φ = 0° elevation plane with (l=1) and without (l=0) azimuthal phase gradient at 31GHz (@ IEEE, 2017).

The first and foremost observation is that both cases have equal radiation cone angles that correspond to the design one (i.e., $\theta_c = \theta_r = 15°$) and their radiation patterns are almost identical around the cone angle. Furthermore, we observe that the presence of the azimuthal phase gradient (in addition to the radial phase gradient) features a deep null in the boresight direction as compared to the Bessel-beam reflectarray without the azimuthal phase gradient (i.e., case with *l*=0). This is expected due to the presence of the phase term in the far-field expression of a higher-order Bessel-Gaussian beam given in Eq. (6.7). Note that a Bessel-beam reflectarray with a larger azimuthal phase gradient (i.e., $l = 2,3,\ldots$) does not have any superiority to the one with *l*=1 in terms of the boresight null, and therefore is not shown here for the sake of brevity. Next we examine the effects of the reflectarray diameter and the θ_r parameter on the reflectarray's cone-shaped pattern. In each case, we only change the corresponding parameter and keep *F/D*=0.7, *l*=1, and edge taper (-12dB) constant as the previous design.

We observe from Fig. 6.11(a) that increasing the reflectarray's diameter by a factor of two increases the antenna directivity in the cone angle direction ($\theta_c = 15°$) by about 2.9dB. Therefore, by increasing the reflectarray diameter, one can increase the antenna directivity for a certain cone angle. Furthermore, Fig. 6.11(b) shows the effect of the radial phase gradient [i.e., θ_r in Eq.(6.16)] on the cone angle of the reflectarray's cone-shaped pattern. It is observed that the proposed Bessel-beam reflectarray features a wide-angle cone-shaped pattern scanning capability. One way to achieve a Bessel-beam reflectarray with radiation cone angle scanning capability is to properly integrate RF MEMS switches or varactors into

each of its elements to dynamically adjust the local elements' angular orientations and thus the radial phase gradient on the reflectarray surface.

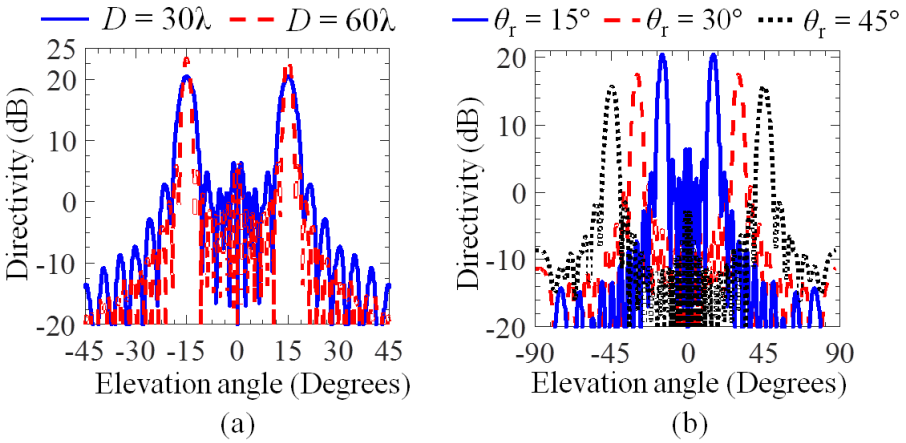

Fig. 6.11 The effect of (a) the diameter of the cone-shaped Bessel-beam reflectarray (with l=1 and $\theta_r = 15°$), and (b) the radial phase gradient amount (i.e., θ_r) in Eq. (6.9), on the cone angle (@ IEEE, 2017).

B. Helical-beam reflectarrays

In this subsection, we examine reflectarrays that generate OAM-carrying helical-beams (i.e., Laguerre-Gaussian beams theoretically investigated in Sec. 2-*B*) by imposing only azimuthal phase gradient [i.e., excluding the radial phase gradient in Eq. (6.16) by setting $\theta_r = 0$] on the illuminating beam to emulate a spiral phase plate (see Fig. 6.1). Despite the design parameter $\theta_r = 0$, such beams do generate a cone-shaped radiation pattern (see Sec. II-*B*). Indeed, Fig. 6.12(a) shows the RHCP radiation pattern of such a reflectarray (with diameter D=7.5λ where λ=10mm) for various azimuthal index numbers l in $\varphi = 0^\circ$ elevation plane. As the l number increases from 1 to 2 to 3, the radiation cone angle (i.e., θ_c) of the reflectarray's cone-shaped pattern increases from 7.5° to 11° to 14°, respectively.

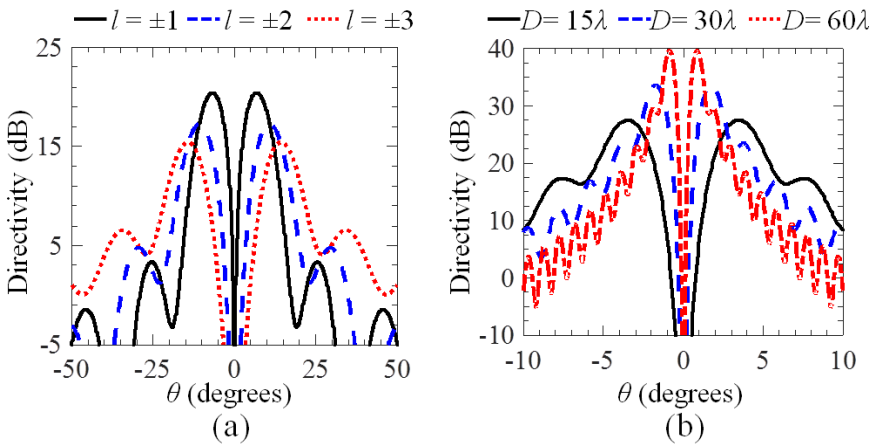

Fig. 6.12 RHCP radiation pattern (in dB) of an OAM-carrying cone-shaped helical-beam reflectarray designed based on only azimuthal phase gradient versus (a) azimuthal index number l (D=7.5λ), and (b) reflectarray diameter (l=±3), in φ = 0° elevation plane. Patterns evaluated by using Fourier-transform of the aperture field (@ IEEE, 2017).

However, such radiation cone angles are different from the theoretical cone angles calculated from Eq. (6.15) (i.e., 4.14°, 5.86°, and 7.17°, respectively). In equation (6.15), the equivalent beam waist of the generated Laguerre-Gaussian beam by the reflectarray (i.e., w_g) is calculated as the half width of the normalized aperture field magnitude on the reflectarray surface at $1/e$ and is equal to $w_g = 0.415D$ for the reflectarray with F/D=0.7. Note that the theoretical cone angle in Eq. (6.15) is calculated based on the *paraxial* approximation and is only valid for large beam waists (i.e., large reflectarray diameters and thus small cone angles). As we show in the following, when the reflectarray diameter increases the theoretical radiation cone angle, calculated by Eq. (6.15), approaches to the simulated one. We also observe from Fig. 6.12(a) that the HPBW solid angle of the cone-shaped pattern increases with the azimuthal index number l, which in turn decreases the maximum directivity of the reflectarray. Note that increasing the azimuthal index number to the values larger than 3 features a large azimuthal phase gradient that may not be

effectively resolved for a reflectarray with D=7.5λ and by reflectarray elements with cell size as large as $\lambda/2$. This would in turn perturb the azimuthal symmetry of the reflectarray's desired cone-shaped pattern and therefore has not been examined here. Note that the radiation pattern for a helical-beam reflectarray with azimuthal index number $-l$ is identical to that for a helical-beam reflectarray with azimuthal index number $+l$ (see Fig. 6.12), and they only differ by variation of their phase with the azimuthal position in far-field.

Although a helical-beam reflectarray with radiation cone angle as large as $\theta_c = 14°$ is designed here by only imposing the azimuthal phase gradient (with l=±3), the radiation cone angle shifts toward smaller angles as the reflectarray diameter ($w_g = 0.415D$) increases for high-gain applications. Fig. 6.12(b) shows the effect of the reflectarray diameter on the radiation cone angle for a helical-beam reflectarray with the azimuthal index number l=±3. We observe that the radiation cone angle shifts from about 3.5° to 1.72° to 0.9° as the reflectarray diameter increases from 15λ to 30λ to 60λ which are in good agreement with the theoretical cone angles calculated from Eq. (6.15), i.e., 3.58°, 1.79°, and 0.9°, respectively. Therefore, range of the radiation cone angle achieved by the helical-beam reflectarray (which is merely based on azimuthal phase gradient) is much narrower than that achieved by the Bessel-beam reflectarray (which is designed based on both azimuthal and radial phase gradients), especially for high-gain applications (i.e., large reflectarray diameters). Note that Eq. (6.15) also shows that the radiation cone angle decrease with increasing the reflectarray diameter (here $w_g = 0.415D$). Although reflectarrays with larger diameters can generally resolve larger azimuthal index numbers,

given that the element period is constant there is always a limit on the maximum azimuthal index number that can be resolved with a reflectarray with a certain diameter. In the next section, we exploit helical beams featuring only azimuthal phase gradients to achieve multiple azimuthally-distributed pencil beams.

Sec. 6.5 Azimuthal Multi-Beam Reflectarray

Let us assume two OAM-carrying helical beams featuring azimuthal phases with azimuthal index numbers l_1 and l_2 are superimposed. The electric field of the interference beam is calculated by the vector sum of the two superimposed beams' electric fields (i.e., $\mathbf{E}=\mathbf{E}_1+\mathbf{E}_2$). The local electric field intensity of the interference beam in far-field (i.e., $I(\theta,\varphi)=\left|\mathbf{E}(\theta,\varphi)\right|^2$) is then calculated as

$$I(\theta,\varphi)=I_1(\theta)+I_2(\theta)+2\sqrt{I_1(\theta)I_2(\theta)}\cos\beta(\theta,\varphi) \tag{6.17}$$

where I_1 and I_2 are the electric field intensities of the helical beams with azimuthal index numbers of l_1 and l_2, respectively, and they are only a function of the elevation angle θ. Note that the phase of each superimposed beam generally contains two terms: (*i*) the azimuthal phase term, and (*ii*) the elevation phase term. In Eq. (6.17), the parameter $\beta(\theta,\varphi)=(l_1-l_2)\varphi+\psi(\theta)$ is the phase difference between the two beams' fields, where $\varphi\in[0,2\pi]$ and ψ is the difference between the elevation phase terms of the two beams and is only a function of the elevation angle θ. Individually, each helical beam with an azimuthal index number l features a cone-shaped radiation pattern in far-field as demonstrated in the previous sections (see Eq. (6.14) and also Fig. 6.12). Let us assume

that the two interfering helical beams (with different azimuthal index numbers) peak at the same elevation angle with comparable field intensities around the peak (cone) angle i.e., $I_1\left(\theta=\theta_c\right)\approx I_2\left(\theta=\theta_c\right)$. The far-field intensity of the interference beam given by Eq. (6.17) is then simplified around the radiation cone angle as

$$I \propto 1+\cos[\left(l_1-l_2\right)\varphi+\psi]=2\cos^2\left(\left[\left(l_1-l_2\right)\varphi+\psi\right]/2\right) \tag{6.18}$$

We observe from Eq. (6.18) that the interference beam has a cosine-shaped standing wave pattern versus φ with total number of $\left|l_1-l_2\right|$ maxima equally spaced on a ring whose central axis is aligned with the beam axis.

In the following, we demonstrate that the interference of two OAM-carrying helical radio beams with different azimuthal index numbers (and zero radial phase gradients) is an efficient apparatus to generate multiple azimuthally-distributed pencil-beams in far-field. Such a radiation pattern exhibits a great potential for sectorization of the 360° azimuthal coverage of the space, single point to multi-point communication, diversity, and MIMO concepts. As an illustrative example, we design an azimuthal multi-beam reflectarray radiating multiple pencil beams pointing toward the elevation angle of 15°. To this aim, we divide the reflectarray surface into two concentric segments, as shown in Fig. 6.13 (a), each radiating a distinct helical beam with a certain azimuthal index number. Here, the azimuthal index number of the inner segment (i.e., l_1) is fixed at +1 while the corresponding parameter of the outer segment is changing accordingly such that we have different numbers of pencil beams as set by the design.

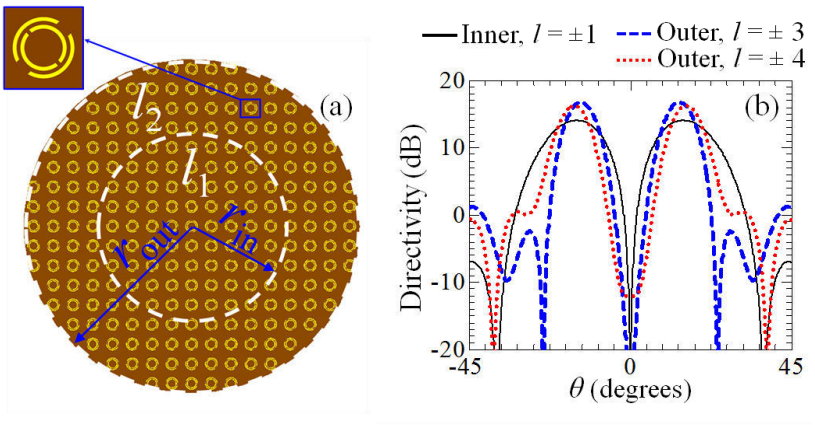

Fig. 6.13 (a) Schematic of a reflectarray antenna with two concentric annular segments featuring different azimuthal index numbers. (b) Fourier-transform RHCP radiation pattern radiated only from the inner segment of the reflectarray in (a) with l_1=±1 in φ=0 elevation plane. Also the directivity patterns radiated only from the outer segments with l_2=±3 and l_2=±4 are plotted. The radius of the inner segment is fixed at r_{in} = 1.5λ and the outer segment radius for l_2=±3 and l_2=±4 are set as r_{out} = 3.75λ and r_{out} = 4λ, respectively, where λ =10mm (@ IEEE, 2017).

The radius of the inner segment (r_{in}) is also chosen as 1.5λ in order to have a cone-shaped pattern with $l_1 = 1$ and radiation cone angle of 15°. The required reflection phase from each cell on each segment with a specific azimuthal index number is obtained from Eq. (6.16) (by setting $\theta_r = 0$, i.e., excluding the radial phase gradient). The directivity pattern radiated only from the inner segment (by setting the field amplitude on the outer segment to zero) is shown in Fig. 6.13(b). Accordingly, the radius of the outer segment (r_{out}) for the azimuthal index number $l_2 = \pm 3$ ($l_2 = \pm 4$) is found to be 3.75λ (4λ), in order to radiate a cone-shaped pattern with cone angle of 15°. The directivity patterns radiated only from the outer segment (i.e., setting the field amplitude on the inner segment to zero) with two different azimuthal index numbers (and two different aforementioned radii) are plotted in Fig. 6.13(b). We observe from Fig. 6.13 that the directivity patterns for all three

cases peak at around 15° elevation angle with comparable values.

Next we plot in Fig. 6.14 the RHCP radiation pattern of the azimuthal multi-beam reflectarray, shown in Fig. 6.13(a), in the $u-v$ plane for different sets of the inner and outer segments' azimuthal index numbers (l_1, l_2). Note that the outer segment radius is r_{out} = 3.75λ for the case with l_2 = ±3 and is r_{out} = 4λ for the case with l_2 = ±4. We observe from Fig. 6.14 that the total number of the pencil beams for each case is $|l_1 - l_2|$ and that they are uniformly distributed around the center (i.e., antenna's boresight direction) and well separated by azimuth angle $360^\circ / |l_2 - l_1|$.

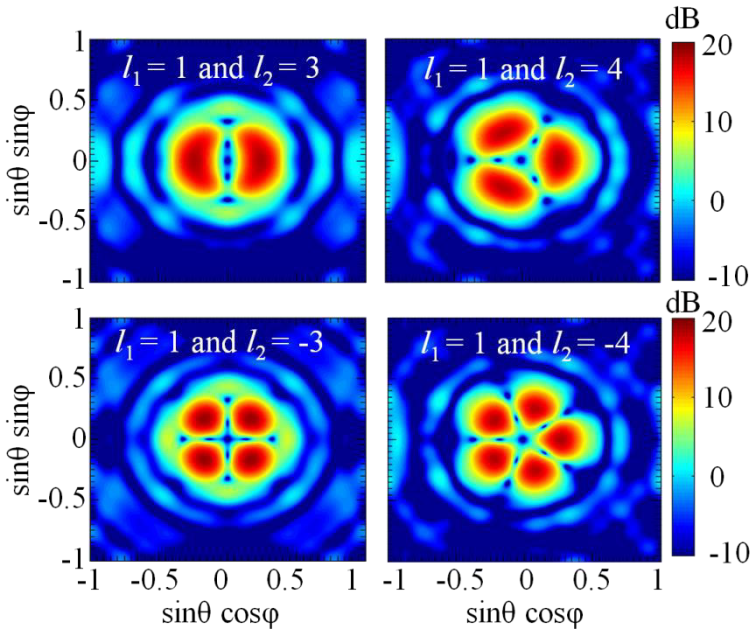

Fig. 6.14 (a) Fourier-transform RHCP radiation pattern (in dB) of an azimuthal multi-beam reflectarray composed of two concentric annular segments [as shown in Fig. 6.13(a)] for different (l_1, l_2) combinations at 30GHz. The inner segment radius and azimuthal index number are set at r_{in} = 1.5λ and l_1 = +1, respectively, while the outer segment radius and azimuthal index number are r_{out} = 3.75λ (4λ) and l_2 = ±3 (±4), respectively, where λ =10mm (@ IEEE, 2017).

As an illustrative example, the full-wave 3-D radiation pattern for a CP quad-beam reflectarray (with $l_1 = 1$, $l_2 = -3$, $r_{\text{in}} = 1.5\lambda$ and $r_{\text{out}} = 3.75\lambda$) is reported in Fig. 6.15. Note that the full-wave radiation pattern here takes into account the aperture blockage due to the illuminating horn and the undesirable diffraction from reflectarray edges. The full-wave RHCP radiation pattern and the axial ratio of the quad-beam reflectarray at $\theta = 15°$ azimuth cone are also reported at various frequencies in Fig. 6.16. We observe that the maximum directivity of the quad-beam reflectarray changes by about 1.5dB within the operating bandwidth (where the maximum directivity is 16.4, 16.9, 17.6, 17.9, 18, and 18dB, at 28, 29, 30, 31, 32, and 33GHz, respectively). Furthermore, the maximum variation between the maximum directivities of the four pencil-beams is about 0.9, 0.4, 0.6, 0.3, 0.6, and 0.4dB at 28, 29, 30, 31, 32, and 33GHz, respectively.

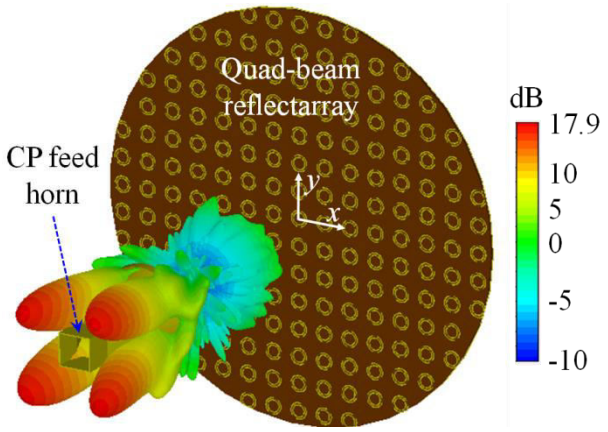

Fig. 6.15 Full-wave RHCP radiation pattern of a quad-beam reflectarray with r_{in} = 1.5λ, r_{out} = 3.75λ (λ =10mm), l_1=1, and l_2=-3 at 31GHz (@ IEEE, 2017).

This shows that the maximum directivity doesn't change significantly from one pencil-beam to the other at each frequency. We also observe from Fig. 6.16 that the reflectarray radiates four well-separated RHCP pencil-beams whose axial ratios are less than 3dB around the main beams' directions from 28GHz to 32GHz. However, the axial ratio slightly

shifts above 3dB at 33GHz as expected from the element's high cross-polarized reflection coefficient magnitude in Fig. 6.4(b). Note that, based on Eq. (6.10), the minimum theoretically achievable axial ratio in the elevation angle of 15° is ~0.3dB.

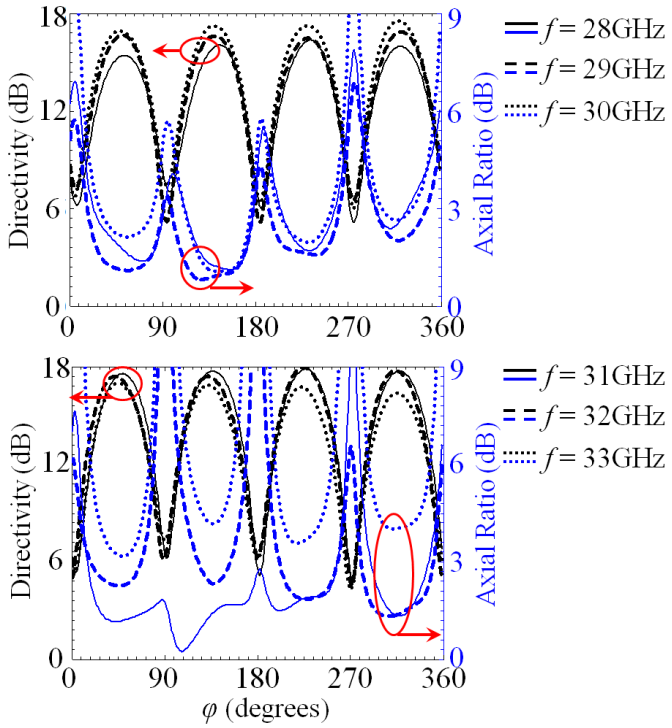

Fig. 6.16 Full-wave RHCP radiation pattern and axial ratio for the quad-beam reflectarray with diameter of 7.5λ in θ=15° azimuth cone at various frequencies (@ IEEE, 2017).

Sec. 6.6 Conclusion

We revisit the concept of the orbital angular momentum (OAM) beams with special attention to their far-field features. In particular, we harness the intrinsic feature of the OAM beams that possess annular-shaped field intensity distribution, to generate cone-shaped radiation patterns. In this regard, novel *circularly-polarized* reflectarray antennas radiating cone-shaped patterns with high azimuthal symmetry and a deep null in boresight direction are conceived at Ka-band. Such reflectarrays are efficiently realized by taking

advantage of the cone-shaped far-field pattern of the OAM-carrying Bessel-Gaussian and helical beams. In particular, we show that Bessel-beam reflectarrays are capable of radiating cone-shaped patterns with high gain and a wide range of cone angles up to ~45°. In contrast, the helical-beam reflectarray generates a cone-shaped pattern with a much smaller radiation cone angle. Moreover, the OAM-concept is further developed here to design multi-beam reflectarrays with multiple pencil-beams azimuthally distributed in space. To this goal, we divide the reflectarray surface into two concentric annular segments that radiate two overlapping cone-shaped helical (Laguerre-Gaussian) radio beams with different azimuthal index numbers (OAM numbers). The proposed Bessel-beam and helical-beam reflectarrays may find interesting applications in satellite communications with mobile vehicles, beam shaping, as well as short-range wireless communication links.

This chapter is reproduced based on the material in [M. Veysi, C. Guclu, F. Capolino, Y. Rahmat-samii, "Revisiting the Orbital Angular Momentum Beams: Fundamentals, Reflectarray Generation, and Novel Antenna Applications," in review with *IEEE Antenna and Propagation Magazine*].

References

[1] L. Allen, M. W. Beijersbergen, R. J. C. Spreeuw, and J. P. Woerdman, “Orbital angular momentum of light and the transformation of Laguerre-Gaussian laser modes,” Phys. Rev. A, vol. 45, no. 11, pp. 8185–8189, Jun. 1992.

[2] I. B. Djordjevic, “Deep-space and near-Earth optical communications by coded orbital angular momentum (OAM) modulation,” Opt. Express, vol. 19, no. 15, pp. 14277–14289, Jul. 2011.

[3] J. Wang et al., “Terabit free-space data transmission employing orbital angular momentum multiplexing,” Nat. Photonics, vol. 6, no. 7, pp. 488–496, Jul. 2012.

[4] M. Veysi, C. Guclu, and F. Capolino, “Vortex beams with strong longitudinally polarized magnetic field and their generation by using metasurfaces,” J. Opt. Soc. Am. B, vol. 32, no. 2, p. 345, Feb. 2015.

[5] J. D. Jackson, Classical Electrodynamics, 3rd Edition. Wiley.
[6] O. Edfors and A. J. Johansson, “Is Orbital Angular Momentum (OAM) Based Radio Communication an Unexploited Area?,” IEEE Trans. Antennas Propag., vol. 60, no. 2, pp. 1126–1131, Feb. 2012.
[7] S. M. Mohammadi et al., “Orbital Angular Momentum in Radio; A System Study,” IEEE Trans. Antennas Propag., vol. 58, no. 2, pp. 565–572, Feb. 2010.
[8] M. Padgett, J. Courtial, and L. Allen, “Light’s orbital angular momentum,” Phys. Today, vol. 57, no. 5, pp. 35–40, May 2004.
[9] L. Allen, S. M. Barnett, and M. J. Padgett, Optical Angular Momentum. CRC Press, 2016.
[10] Q. Zhan, Vectorial Optical Fields: Fundamentals and Applications. World scientific, 2014.
[11] X. Wei et al., “Generation of arbitrary order Bessel beams via 3D printed axicons at the terahertz frequency range,” Appl. Opt., vol. 54, no. 36, p. 10641, Dec. 2015.
[12] F. Tamburini, E. Mari, A. Sponselli, B. Thidé, A. Bianchini, and F. Romanato, “Encoding many channels on the same frequency through radio vorticity: first experimental test,” New J. Phys., vol. 14, no. 3, p. 033001, Mar. 2012.
[13] Y. Yan et al., “High-capacity millimetre-wave communications with orbital angular momentum multiplexing,” Nat. Commun., vol. 5, p. 4876, Sep. 2014.
[14] M. Tamagnone, C. Craeye, and J. Perruisseau-Carrier, “Further Comment on ’Encoding many channels on the same frequency through radio vorticity: first experimental test,” New J. Phys., vol. 15, no. 7, p. 078001, Jul. 2013.
[15] M. Tamagnone, C. Craeye, and J. Perruisseau-Carrier, “Comment on ‘Encoding many channels on the same frequency through radio vorticity: first experimental test,’” New J. Phys., vol. 14, no. 11, p. 118001, 2012.
[16] C. Craeye, “On the Transmittance Between OAM Antennas,” IEEE Trans. Antennas Propag., vol. 64, no. 1, pp. 336–339, Jan. 2016.
[17] M. W. Beijersbergen, R. P. C. Coerwinkel, M. Kristensen, and J. P. Woerdman, “Helical-wavefront laser beams produced with a spiral phaseplate,” Opt. Commun., vol. 112, no. 5–6, pp. 321–327, Dec. 1994.
[18] M. S. Soskin, V. N. Gorshkov, M. V. Vasnetsov, J. T. Malos, and N. R. Heckenberg, “Topological charge and angular momentum of light beams carrying optical vortices,” Phys. Rev. A, vol. 56, no. 5, pp. 4064–4075, Nov. 1997.
[19] B. Thidé et al., “Utilization of Photon Orbital Angular Momentum in the Low-Frequency Radio Domain,” Phys. Rev. Lett., vol. 99, no. 8, p. 087701, Aug. 2007.
[20] Y. Pan, S. Zheng, J. Zheng, X. Jin, H. Chi, and X. Zhang, “Orbital angular momentum antenna using dielectric resonator,” in 2015 Asia-Pacific Microwave Conference (APMC), 2015, vol. 3, pp. 1–3.
[21] K. Liu et al., “Generation of OAM Beams Using Phased Array in the Microwave Band,” IEEE Trans. Antennas Propag., vol. 64, no. 9, pp. 3850–3857, Sep. 2016.
[22] D. Zelenchuk and V. Fusco, “Split-Ring FSS Spiral Phase Plate,” IEEE Antennas Wirel. Propag. Lett., vol. 12, pp. 284–287, 2013.
[23] J. C. Batchelor and R. J. Langley, “Microstrip ring antennas operating at higher order modes for mobile communications,” Antennas Propag. IEE Proc. - Microw., vol. 142, no. 2, pp. 151–155, Apr. 1995.
[24] U. H. Park, H. S. Noh, S. H. Son, K. H. Lee, and S. I. Jeon, “A Novel Mobile Antenna for Ku-Band Satellite Communications,” ETRI J., vol. 27, no. 3, pp. 243–249, Jun. 2005.

[25] Y. M. Pan and K. W. Leung, “Wideband Circularly Polarized Dielectric Bird-Nest Antenna With Conical Radiation Pattern,” IEEE Trans. Antennas Propag., vol. 61, no. 2, pp. 563–570, Feb. 2013.
[26] F. Yang, Y. Rahmat-Sami, and A. Kishk, “Low-profile patch-fed surface wave antenna with a monopole-like radiation pattern,” Antennas Propag. IET Microw., vol. 1, no. 1, pp. 261–266, Feb. 2007.
[27] M. Ettorre and A. Grbic, “Generation of Propagating Bessel Beams Using Leaky-Wave Modes,” IEEE Trans. Antennas Propag., vol. 60, no. 8, pp. 3605–3613, Aug. 2012.
[28] M. Vicente-Lozano, G. Franceschetti, F. J. Ares-Pena, and E. Moreno-Piquero, “Analysis and synthesis of a printed array for satellite communication with moving vehicles,” IEEE Trans. Antennas Propag., vol. 50, no. 11, pp. 1555–1559, Nov. 2002.
[29] J. Huang, “Circularly polarized conical patterns from circular microstrip antennas,” IEEE Trans. Antennas Propag., vol. 32, no. 9, pp. 991–994, Sep. 1984.
[30] J. Huang and J. A. Encinar, Reflectarray antennas. Piscataway, N.J.; Hoboken, N.J.: IEEE Press ; Wiley-Interscience, 2008.
[31] A. M. Yao and M. J. Padgett, “Orbital angular momentum: origins, behavior and applications,” Adv. Opt. Photonics, vol. 3, no. 2, pp. 161–204, Jun. 2011.
[32] Constantine A. Balanis, “Wiley: Antenna Theory: Analysis and Design, 4th Edition -.” [Online]. Available: http://www.wiley.com/WileyCDA/WileyTitle/productCd-1118642066.html. [Accessed: 24-Jul-2016].
[33] P. Vaity and L. Rusch, “Perfect vortex beam: Fourier transformation of a Bessel beam,” Opt. Lett., vol. 40, no. 4, p. 597, Feb. 2015.
[34] M. Abramowitz and I. A. Stegun, Eds., Handbook of Mathematical Functions: with Formulas, Graphs, and Mathematical Tables, 0009–Revised edition ed. New York: Dover Publications, 1965.
[35] B. G. Cai, Y. B. Li, W. X. Jiang, Q. Cheng, and T. J. Cui, “Generation of spatial Bessel beams using holographic metasurface,” Opt. Express, vol. 23, no. 6, p. 7593, Mar. 2015.
[36] M. Veysi, C. Guclu, and F. Capolino, “Focused azimuthally polarized vector beam and spatial magnetic resolution below the diffraction limit,” J. Opt. Soc. Am. B, vol. 33, no. 11, p. 2265, Nov. 2016.